ANISOTROPIC SURFACE FEATURES OF SELECTED PHYLLOSILICATES

by

Xihui Yin

A dissertation submitted to the faculty of
The University of Utah
in partial fulfillment of the requirements for the degree of

Doctor of Philosophy

Department of Metallurgical Engineering

The University of Utah

August 2012

The University of Utah Graduate School

STATEMENT OF DISSERTATION APPROVAL

The dissertation of **Xihui Yin**

has been approved by the following supervisory committee members:

Jan D. Miller	, Chair	**May 9, 2012** Date Approved
Xuming Wang	, Member	**May 9, 2012** Date Approved
Michael S. Moats	, Member	**May 9, 2012** Date Approved
Michael L. Free	, Member	**May 9, 2012** Date Approved
Vladimir Hlady	, Member	**May 9, 2012** Date Approved

and by **Jan D. Miller**, Chair of the Department of **Metallurgical Engineering**

and by Charles A. Wight, Dean of The Graduate School.

ABSTRACT

The phyllosilicate minerals are very important in geology, agriculture, and a wide range of industries. It has been known that almost all the processes in mineral processing are significantly influenced by the surface properties of the phyllosilicates. Therefore, the objective of this research is to investigate the anisotropic surface properties of selected phyllosilicates using both experimental and theoretical methods.

A new technique based on atomic force microscopy (AFM) was developed to determine the anisotropic wetting characteristics of kaolinite basal surfaces. The hydrophobicity was determined by the magnitude of the hydrophobic attraction force between a hydrophobic diamond-like-carbon (DLC) AFM tip and the kaolinite basal surfaces. The results demonstrate that the kaolinite silica face has a moderate degree of hydrophobicity, whereas the kaolinite alumina face is hydrophilic. The hydrophobicity of the kaolinite silica face is found to be weaker than the talc basal surface, which may be due to the presence of isomorphous substitutions. Using molecular dynamics simulation (MDS), it is noted that the wetting characteristics and the interfacial water structure of the silica tetrahedral surface of phyllosilicates are greatly affected by the isomorphous lattice substitution. In addition, the surface charging behaviors of chlorite basal plane surfaces and the edge surface were established as a function of pH.

It is expected that the findings from this dissertation research will provide a basis for understanding the behavior of layered silicate particles in flotation systems, leaching systems, and tailing disposal systems.

TABLE OF CONTENTS

LIST OF TABLES

LIST OF FIGURES

ACKNOWLEDGEMENTS

I would like to thank my advisor, Professor Jan D. Miller, for all his guidance, encouragement, and patience during the past four years. His work ethic and enthusiasm toward science motivated me to accomplish this project. The time I discussed with him will be one of my precious memories.

I would like to extend gratitude to my committee members: Dr. Vladimir Hlady, Dr. Michael Free, Dr. Michael Moats, and Dr. Xuming Wang, for their precious time reviewing my dissertation.

Thanks are extended to Dr. Liem Dang, Dr. Xiuquan Sun, and Dr. Tsun-Mei Chang at Pacific Northwest National Lab and Dr. Hao Du from the Chinese Academy of Sciences for opening the door of molecular dynamics simulation for me. Thanks are also extended to Dr. Zhenghe Xu at the University of Alberta. A part of the work in this dissertation was completed under his guidance and support from his research group.

Thanks are also extended to the U.S. Department of Energy and Newmont Mining Corporation for their financial support on this research project.

I would like to thank all the faculty and staff in the Department of Metallurgical Engineering at the University of Utah for giving me this great opportunity to work with researchers all around the world. Also, thanks to all my colleagues and friends for their valuable discussions and suggestions during the completion of this dissertation.

Finally, I would like to express my love and appreciation to my parents and my husband for their support all these years.

CHAPTER 1

INTRODUCTION

The group of phyllosilicates, or sheet silicates, including serpentine, micas, chlorite, and the clay minerals, is very important in geology, agriculture, and mineral processing (H. Murray and Kogel 2005; Harvey and Murray 1997; Haydn 1991). Some of the phyllosilicates in a pure state can be valuable materials in widespread applications, including, for example, in ceramics, in the manufacture of paper (as a coating, pigment, and filler), in inks and paints (as an extender), in medicine, and as an additive in the production of rubber and polymers (Harvey and Murray 1997; Haydn 2000). According to different surface properties, different phyllosilicates may have different applications. For instance, muscovite can be used in fireproofing and insulating materials. Due to its ultraflatness, muscovite is also a good substrate for many kinds of scientific studies. Montmorillonite, a type of swelling clay, can be used to remove moisture from air and it is also proven to be an important component in oil drilling mud. Moreover, it is also widely applied in medicine and pharmacology, for stabilization of suspensions and emulsions as well as being used as a drug carrier (Lin, Jian, and Lee 2000; Wai and Banker 1966).

However, in other circumstances, the phyllosilicates, such as kaolinite, illite, and talc, may create problems in making efficient particle separations (concentration) and in achieving satisfactory sedimentation/consolidation for waste disposal (tailings). For

example, during bauxite flotation, kaolinite and illite often bring difficulties for the recovery of the gibbsite, diaspore, and boehmite (Hu and Liu 2003; Hu, Liu, and Xu 2003; Hu et al. 2003). In another case, the oil sands industry, the efficient separation of bitumen from phyllosilicates, including kaolinite, illite, and montmorillonite, is always a challenge (Liu, Xu, and Masliyah 2004). Also, these phyllosilicates may significantly influence the sedimentation rate of the oil sands tailings (Chalaturnyk, Scott, and Ozum 2002, Fine Tailings Fundamentals 1995). All of these processes, including wettability, aggregation, dispersion, flotation, and thickening, are affected by the crystal structure and surface properties of phyllosilicates (Hu et al. 2005; Ma and Pierre 1999). In this regard, the study of phyllosilicate surface chemistry is very critical to the understanding of particulate separation processes and to the development of effective ways for the improvement of separation efficiency.

1.1 Clay Mineralogy

Two basic structural units in the phyllosilicate minerals are the silica tetrahedron and alumina/magnesia octahedron. In each silica tetrahedron, the silicon atom occupies the center position and tetrahedrally coordinates with the nearest four oxygen atoms. The tetrahedrons are joined together to form a hexagonal tetrahedral sheet by sharing three oxygen atoms with other tetrahedrons. The structures of the silica tetrahedron and the silica tetrahedral sheet are shown in Figure 1.1. This silica tetrahedral sheet is bonded with the octahedral sheet by sharing the apical oxygen atoms. The octahedral sheet is composed of octahedrons in which the cation is surrounded by six oxygen atoms or hydroxyls (see Figure 1.2). Both divalent cations (like Mg^{2+} and Fe^{2+}) and trivalent cations (like Al^{3+}) can be the cations in the octahedral sheet. Also, other elements such as

Cu, Ni, Mn, Cr, Zn, Ti, etc. can also be present in the octahedral sheets. If the divalent cations occur in the octahedral sheet, all three octahedrons are occupied and this structure is classified as a trioctahedral sheet silicate or a "brucite type." In another case, if trivalent cations occur in the octahedral sheet, only two octahedrons are occupied and this structure is classified as a dioctahedral sheet silicate or a "gibbsite type." Due to the different stacking structure of a silica tetrahedral sheet and alumina/magnesia octahedral sheets, the phyllosilicates can be classified into two groups, bilayer phyllosilicates and trilayer phyllosilicates. The details of these two groups of phyllosilicates will be described in the following sections.

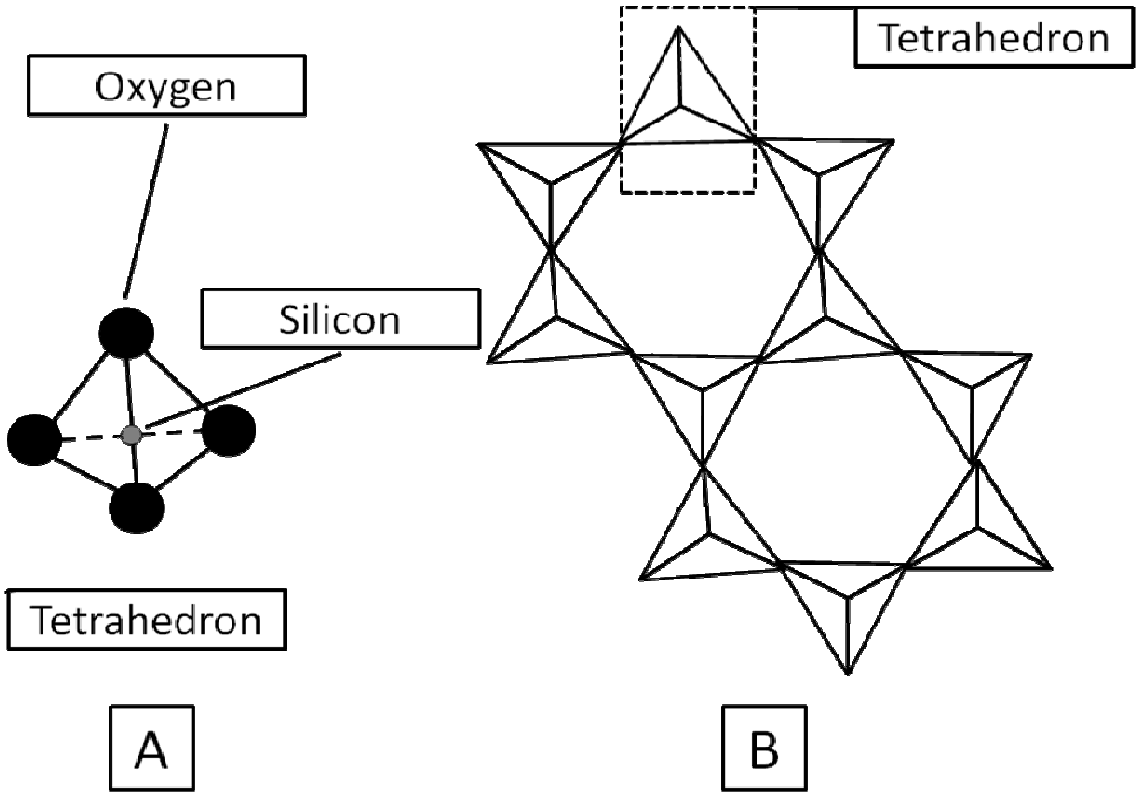

Figure 1.1 – Structure of the silica tetrahedron (A) and the top view of a tetrahedral sheet (B). Large black circles represent oxygen atoms and small grey circle represents a silicon atom.

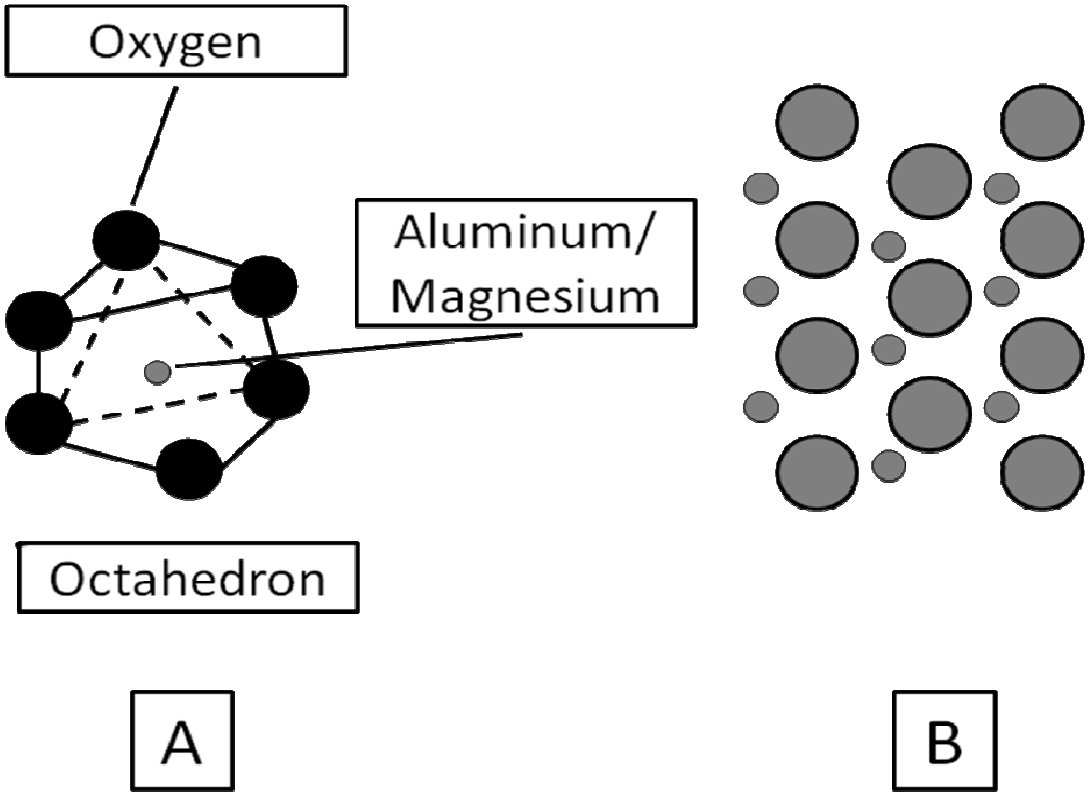

Figure 1.2 – Structure of the alumina/magnesia octahedron (A) and the top view of an octahedral sheet (B). Large black circles represent oxygen atoms, small grey circles represent aluminum or magnesium atoms, and large grey circles represent oxygen atoms or hydroxyl groups in the octahedral sheet.

1.1.1 Bilayer Phyllosilicates

The phyllosilicate minerals which have the repeating unit of one silica tetrahedral sheet bonded to one octahedral sheet are classified as bilayer phyllosilicates or 1:1 type phyllosilicates. The bilayer phyllosilicates can be divided into two subgroups, kaolinite group and serpentine group. Kaolinite group includes kaolinite, halloysite, dickite, and nacrite, whereas chrysotile, antigorite, and lizardite belong to the serpentine group. The composition and structural features of some selected bilayer silicates are shown in Table 1.1. Based on the different particle shapes, bilayer phyllosilicates can also be classified into planar structure and tubular structure. For example, kaolinite and lizardite are two types of bilayer phyllosilicates with planar structure. Kaolinite has Al^{3+} in the octahedral sheet, whereas lizardite has Mg^{2+} in the octahedral sheet. The bilayer sheets are joined by strong hydrogen bonds. The distance between the repeating units in kaolinite is about 0.72 nm. The crystalline structure of kaolinite is shown in Figure 1.3.

Sometimes, due to the imperfect fit of the octahedral sheet and the tetrahedral sheet, the planar crystal structure may bend. Antigorite is one of the phyllosilicates that exhibits a bending structure. The bending in the antigorite is not continuous, but presents as alternating inverted domains. When structural bending is more continuous, the planar sheet may become rolled and exhibit a tubular structure. The typical minerals with tubular structure are halloysite (dioctahedral) and chrysotile (trioctahedral). In most cases, the phyllosilicates with tubular structure are present as fibrous crystals. The schematics of the bilayer phyllosilicates with planar structure and tubular structure are shown in Figure 1.4.

Table 1.1 – Composition and structural features of selected bilayer phyllosilicates.

Chemical composition	Planar structure	Tubular structure
$Al_2Si_2O_5(OH)_4$	Kaolinite	Halloysite
$Mg_3Si_2O_5(OH)_4$	Lizardite/Antigorite	Chrysotile

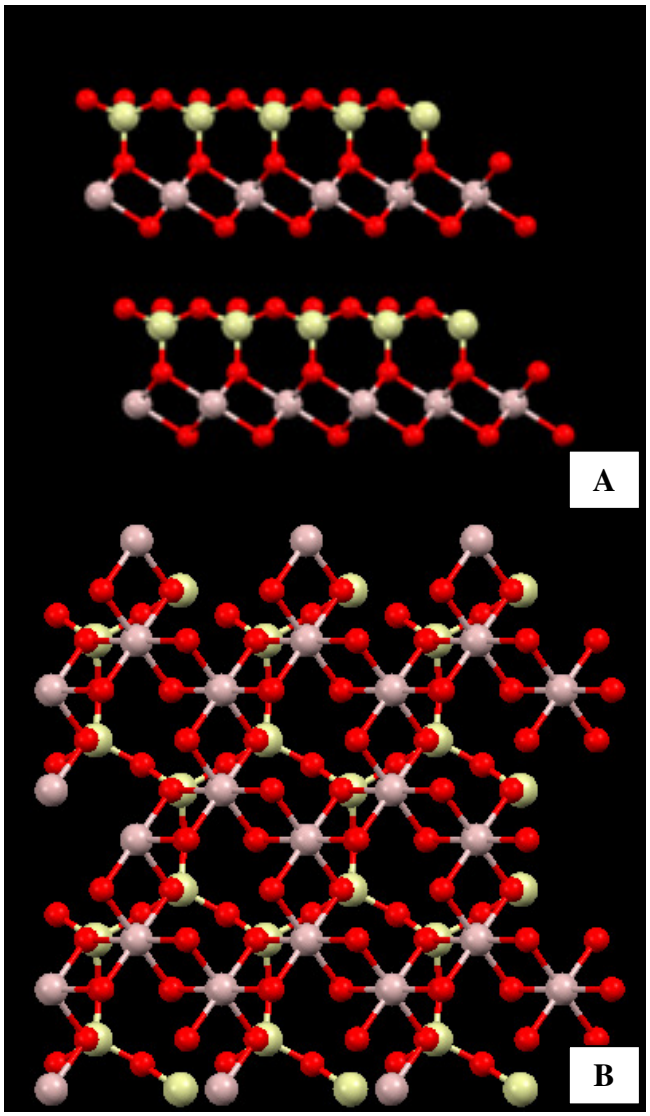

Figure 1.3 – Crystalline structure of kaolinite, side view (A) and top view of alumina face (B). Pink: aluminum; Yellow: silicon; Red: oxygen.

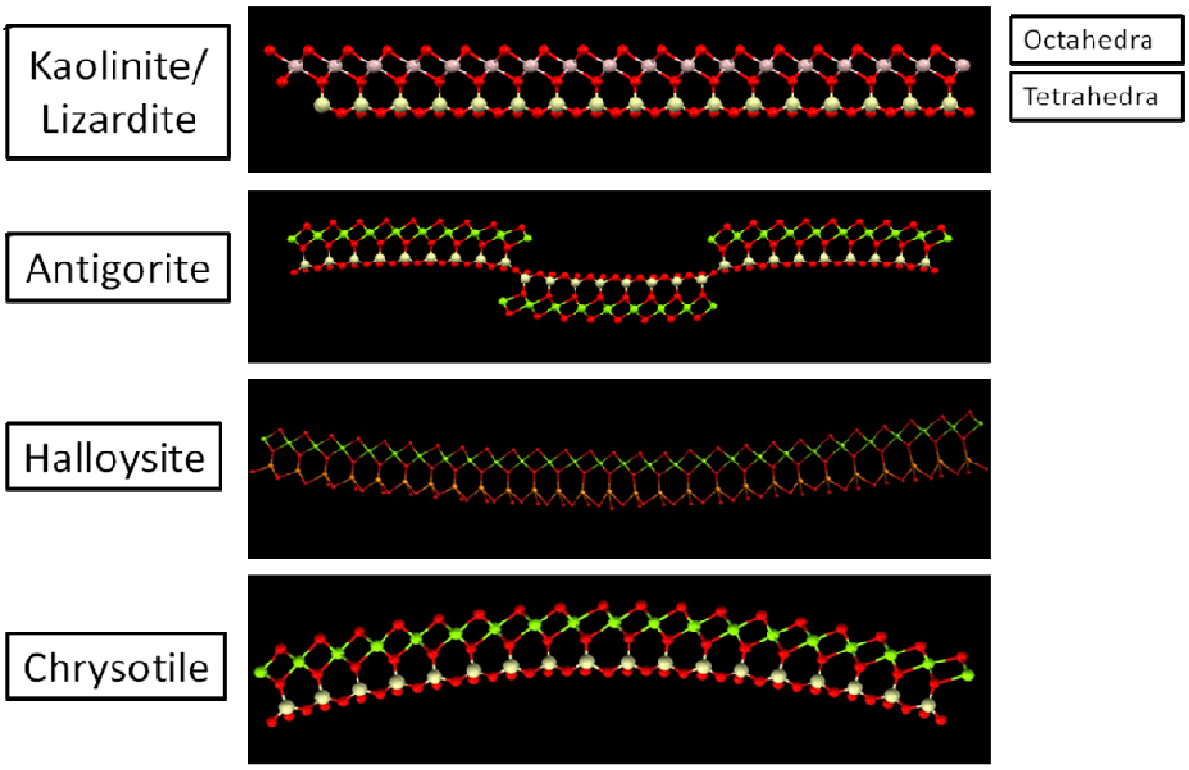

Figure 1.4 – Schematic of the crystalline structure for selected bilayer phyllosilicates.

1.1.2 Trilayer Phyllosilicates

Trilayer phyllosilicates are another important group. The trilayer phyllosilicates have a structure of one octahedral sheet sandwiched by two tetrahedral sheets, which are also known as 2:1 type phyllosilicates. There are five major subgroups in the trilayer phyllosilicates, including talc-pyrophyllite, mica, chlorite, smectite, and vermiculite.

Talc has the chemical formula of $Mg_3Si_4O_{10}(OH)_2$. The positive charge in the octahedral layer is compensated by two silica tetrahedral layers, resulting in a neutral charge on each trilayer sheet. The trilayers are bonded together through van der Waals forces so that the layers are easy to cleave along the (001) plane. The distance between two trilayer sheets is about 0.94 nm (Rayner and Brown 1973). The lattice structure of

talc is shown in Figure 1.5. Pyrophyllite ($Al_2Si_4O_{10}(OH)_2$) has the similar structure to talc. The difference is that pyrophyllite has aluminum as the cation in the octahedral layer, whereas talc has magnesium in its octahedral layer. Similar to talc, pyrophyllite is also electrically neutral for each trilayer sheet and it has no interlayer cations.

Mica is another type from the trilayer phyllosilicates group (2:1 structure). The common mica minerals include muscovite ($KAl_2(AlSi_3O_{10})(OH,F)_2$), phlogopite ($KMg_3(AlSi_3O_{10})(OH,F)_2$), biotite ($K(Mg,Fe,Mn)_3(AlSi_3O_{10})(OH, F)_2$), margarite ($CaAl_2(Al_2Si_2O_{10})(OH)_2$), and lepidolite ($K_2LiAl_6(Al_6Si_6O_{20})(OH, F)_4$). The micas have similar structure and properties. As an example, muscovite has one-fourth of the silicon atoms in the tetrahedral layer substituted by aluminum atoms, causing a negatively charged trilayer sheet. This negative charge is neutralized by interlayer cations (K^+) which fit into the hexagonal holes in the silica tetrahedral sheet. The layer thickness of muscovite is about 1 nm. The lattice structure of muscovite is shown in Figure 1.6.

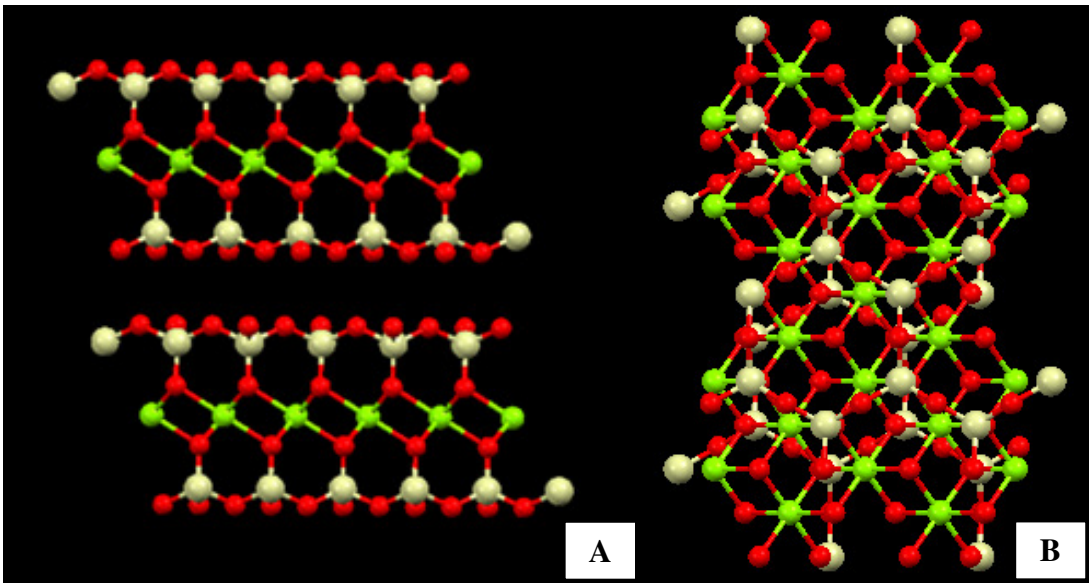

Figure 1.5 – Crystalline structure of talc, side view (A) and top view (B). Green: magnesium; Yellow: silicon; Red: oxygen.

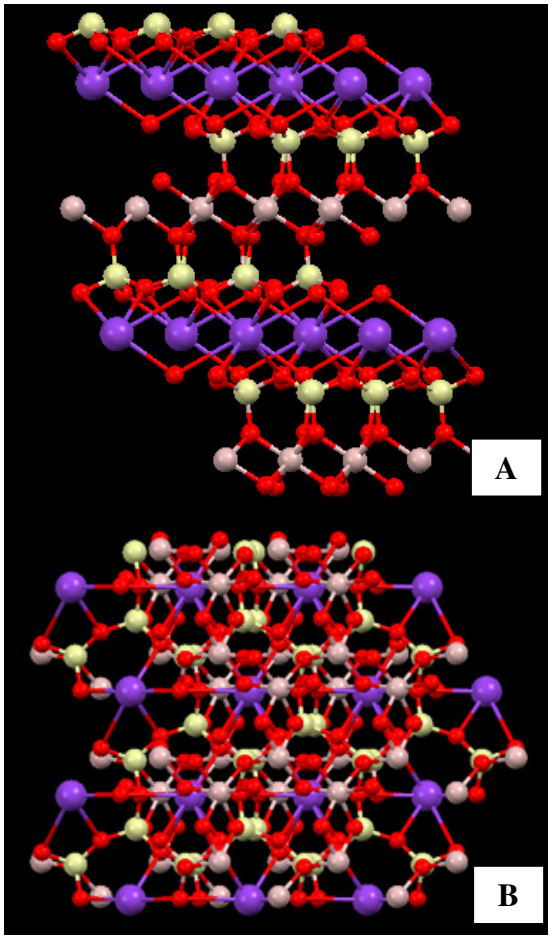

Figure 1.6 – Crystalline structure of muscovite, side view (A) and top view (B). Purple: potassium; Yellow: silicon; Red: oxygen; Pink: aluminum. (The aluminum substitutions in the silica tetrahedral layer are not shown in this figure.)

Smectite is another class of trilayer phyllosilicate having the group of 2:1 structure with a dioctahedral sheet or trioctahedral sheet sandwiched between two silica tetrahedral sheets. One of the most common smectites is montmorillonite with a general chemical formula of $(1/2Ca,Na)(Al,Mg,Fe)_4(Si,Al)_8O_{20}(OH)_4 . nH_2O$ (van Olphen 1963). The montmorillonite contains a large amount of isomorphous substitution in both silica sheets and alumina sheets, the excess of negative lattice charge exists and is compensated by the interlayer cations. The lattice structure of montmorillonite is shown in Figure 1.7.

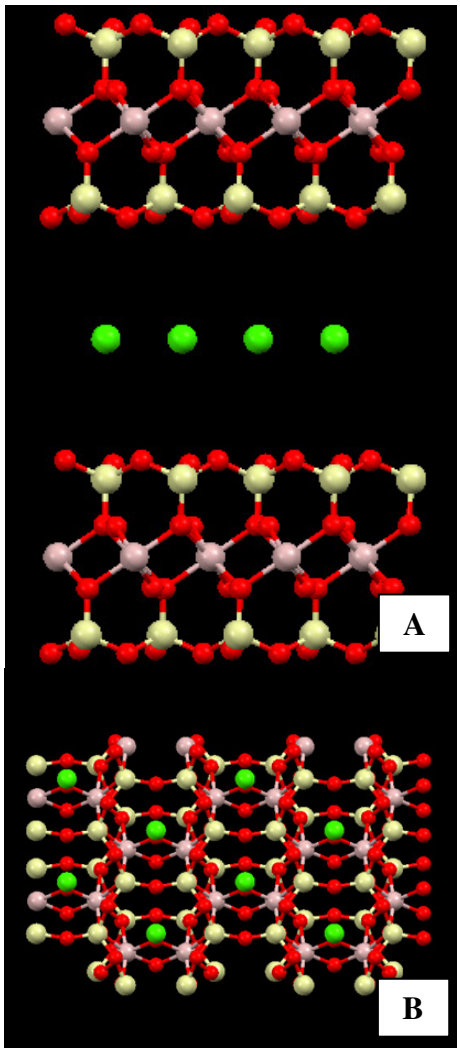

Figure 1.7 – Crystalline structure of montmorillonite, side view (A) and top view (B). Green: Interlayer exchangeable cations; Pink: aluminum; Yellow: silicon; Red: Oxygen. (The aluminum substitutions in the silica tetrahedral layer are not shown in this figure.)

It can also have significant amounts of Mg and Fe substituting into the octahedral sheets. The distance between montmorillonite layers is in a range of 0.98 nm to 1.8 nm. When the montmorillonite is in contact with water or water vapor, the compensating cations on the layer surfaces can be easily exchanged by other cations in solution. Meanwhile, the water molecules can penetrate between the layers which results in so-called “interlayer swelling” or “crystalline swelling,” resulting in expansion of the

particle. The phyllosilicate minerals which have this unique behavior are also known as expandable silicates.

Chlorite ($(Mg_5Al)(Si_3Al)O_{10}(OH)_8$) is a class of phyllosilicates with a mixed structure. The common minerals in the chlorite class include clinochlore ($(Mg_5Al)(AlSi_3)O_{10}(OH)_8$), chamosite ($(Fe_5Al)(AlSi_3)O_{10}(OH)_8$), nimite ($(Ni_5Al)(AlSi_3)O_{10}(OH)_8$), and pennantite ($(Mn, Al)_6(Al,Si)_4O_{10}(OH)_8$). The chlorite structure is depicted as consisting of a brucite-like layer (with some aluminum) sandwiched between mica-like trilayers that are similar to phlogopite. Since chlorite has two octahedral sheets, it is also called 2:1:1 phyllosilicate. The lattice structure of clinochlore is shown in Figure 1.8. Chlorite is a nonexpandable phyllosilicates. The thickness between chlorite layers is about 1.4 nm.

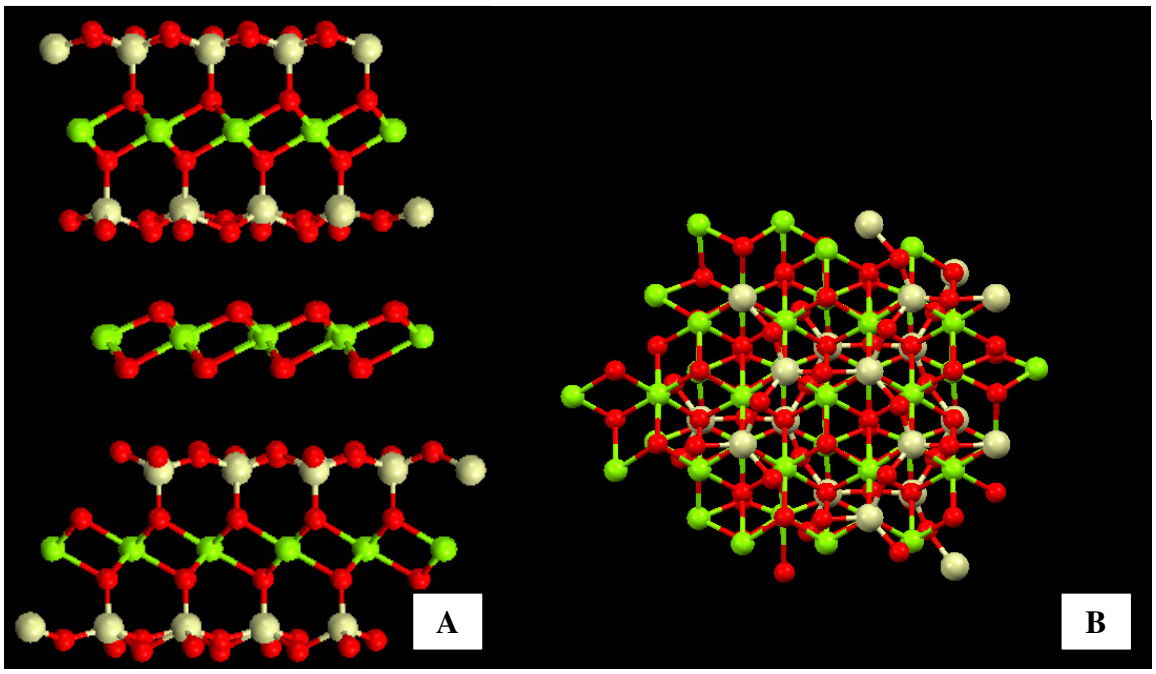

Figure 1.8 – Crystalline structure of clinochlore, side view (A) and top view (B). Green: magnesium; Yellow: silicon; Red: oxygen. (The aluminum substitutions in the silica tetrahedral layer are not shown in this figure.)

1.2 Physical Properties

The physical properties for selected phyllosilicates are discussed in this section. Kaolinite is usually transformed from the chemical weathering of aluminium silicate, for example, feldspar. It is commonly present as pseudohexagonal platy particles with the natural cleavage plane of (001). The particles are soft and white in color, but sometimes show as blue or brown due to the impurities. It has a low swelling capacity and low cation exchange capacity (1-15 meq/100g). The specific gravity is between 2.16 g/cm^3 to 2.68 g/cm^3. The refractive index for kaolinite is: n_α=1.552-1.576, n_β=1.582-1.615, and n_γ=1.587-1.618.

Muscovite is formed from the alteration of topaz, feldspar, and kyanite. It is famous for its near perfect basal cleavage (001) plane. The muscovite is usually present as white, grey, silverery, or transparent. The specific gravity is around 2.76 g/cm^3 to 3 g/cm^3. It is an anisotropic material with high birefringence. The refractive index for muscovite is: n_α=1.553-1.563, n_β=1.559-1.569, and n_γ=1.56-1.57.

Talc is a mineral formed from the metamorphism of serpentine, pyroxene, amphibole, olivine, etc. It is the softest mineral and has a greasy feel. Talc has a color of white, grey, or green. The specific gravity is 2.5 g/cm^3 to 2.8 g/cm^3. The refractive index for talc is: n_α=1.538-1.550, n_β=1.589-1.594, and n_γ=1.589-1.6.

Montmorillonite is one of the typical minerals in the smectite family. The distinguishing feature of montmorillonite is the high cation exchange capacity (70-100 meq/100g) and swelling capacity. It usually occurs as fine platy particles. The color of montmorillonite can be white, blue, yellow, green, etc. The specific gravity is 1.7 g/cm^3

to 2 g/cm^3. The refractive index for montmorillonite is: n_α=1.485-1.535, n_β=1.504-1.550, and n_γ=1.505-1.550.

The chlorite minerals are commonly derived from the alteration of mafic minerals, including pyroxene, amphibole, and biotite. It is a soft mineral with a color of light or dark green. Due to the complexity in chemical composition, the physical and optical properties of chlorite have a broad range. The specific gravity is 2.6 g/cm^3 to 3.3 g/cm^3. The refractive index for chlorite is: n=1.57-1.67.

1.3 Anisotropic Surface Characteristics

Almost all the phyllosilicate minerals show significant anisotropic surface characteristics due to their anisotropic crystalline structure. It is known that the surface properties at phyllosilicate basal planes and edge plane differ greatly. The silica tetrahedral basal surface with a siloxane structure has an extremely low affinity for protons (Bleam, Welhouse, and Janowiak 1993; White and Zelazny 1988). It is believed that the surface charge at the silica tetrahedral face is mainly from the isomorphous lattice substitutions and the surface charge is fixed and pH-independent. Previous research has revealed that the isomorphous lattice substitution plays an important role on the surface properties (Bleam 1990; Sposito et al. 1999). If there is no, or little, isomorphous substitution in the lattice, the nonpolar nature of this siloxane-terminated basal plane would be nonpolar and have a hydrophobic character with a small surface charge. When the isomorphous substitutions are present in the silica tetrahedral basal planes, the surface becomes negatively charged and the affinity for cation adsorption and wetting by water molecules is greatly enhanced. This could be attributed to the distortions in the local electrical field caused by the isomorphous substitution at the silica tetrahedral basal

planes (Bleam 1990). Unlike the valence-saturated silica tetrahedral basal surface, the edge surfaces are terminated with broken bonds with valence unsaturated atoms. These unbounded oxygen atoms promote the protonation/deprotonation reactions at the edge surface (Avena and De Pauli 1998; Bickmore et al. 2001; Tanaka et al. 1994). In this regard, the edge surface of phyllosilictes is pH-dependent. The charging behavior of the edge surfaces for talc and muscovite have been characterized by Zhao et al. and Yan et al. in recent studies (Yan et al. 2011; Zhao et al. 2008).

For some phyllosilicates, such as kaolinite, a significant difference in the surface charging behavior has been observed for the 001 and the 00$\underline{1}$ basal plane surfaces (Gupta and Miller 2010). When a phyllosilicate mineral is cleaved, sometimes the newly created two basal planes are not identical. For example, kaolinite has one silica tetrahedral sheet bonded with one alumina octahedral sheet as the repeating unit. Ideally, when kaolinite is cleaved, both the silica tetrahedral face and the alumina octahedral face will be exposed. Unlike the siloxane structure in the silica tetrahedral face, the alumina octahedral face is terminated with a layer of hydroxyl groups which can hydrogen bond with water molecules and also can easily undergo the protonation/deprotonation reactions. Thus, the different crystalline structures lead to significantly different surface properties at the two basal planes of kaolinite. Recently, the different charging behavior at the two kaolinite faces has been observed by Gupta et al. (Gupta and Miller 2010) using AFM surface force measurements. However, wetting characteristics, or the surface hydrophobicity, of the kaolinite silica face and alumina face have not been reported in the literature.

The analysis of the surface properties for some of the phyllosilicates is challenging due to their submicron size, various shapes, and especially their anisotropic

character. In this regard, a systematic study of the anisotropic surface charging characteristics and hydrophobicity of phyllosilicate surfaces is desirable. This research mainly focuses on two typical phyllosilicates showing significant anisotropic characteristics, kaolinite and chlorite. It is expected that the results of this research will contribute to the further explanation of surface charging and wetting characteristics for phyllosilicates and their effect on flotation separations.

1.4 Research Objectives

The overall objective of this dissertation is to investigate the anisotropic surface properties of selected phyllosilicates, basically focusing on kaolinite and chlorite, using experimental and theoretical techniques. It is expected that the surface charge of face and edge surfaces will be established. In addition, an experimental technique which can estimate the hydrophobicity of the phyllosilicate surfaces will be developed. In this way, the wetting characteristics of selected surfaces will be established. Specifically, the hydrophobicity of the silica tetrahedral layer will be considered with respect to structural features. It is expected that this fundamental information will provide a basis for understanding the behavior of layered silicate particles in flotation systems, leaching systems, and tailing disposal systems.

1.5 Research Organization

Chapter 2 reviews the surface properties of different types of phyllosilicates with regard to the recent research results reported in the literature. The surface charging behavior of phyllosilicates is reviewed based on various analytical techniques, including electrophoresis, titration, and atomic force microscopy (AFM). The principles of these

techniques are introduced and the results generated using these experimental techniques were compared. The wetting characteristics of phyllosilicates from contact angle measurements and molecular dynamics simulation (MDS) are also reviewed. The effect of phyllosilicate crystalline structure on the surface polarity is discussed.

Chapter 3 discusses a newly developed AFM-based technique for the characterization of surface wettability. Contact mode AFM cantilevers and tips coated with a thin layer of hydrophobic diamond-like-carbon (DLC) are used. The interaction force between this hydrophobic diamond-like-carbon tip and the surfaces of interest determines the hydrophobicity of specific surfaces by measuring the direction and magnitude of the detected hydrophobic force. The collected surface forces are then fitted with a mathematical model to have a quantitative understanding of the hydrophobicity. This technique is validated by detecting the interaction force between the DLC tips and hydrophobized silica substrates with different extents of hydrophobicity. The surface force curves are discussed with respect to corresponding contact angles of the substrates.

Chapter 4 presents the results for the surface hydrophobicity of kaolinite surfaces as determined from AFM surface force measurements. The surface force curves for the kaolinite silica face and alumina face were collected and compared with force curves at muscovite and talc surfaces. The origin of the detected short-range hydrophobic force is discussed with the theoretical van der Waals interaction when considering the presence of the water exclusion zone at the hydrophobic surfaces. Moreover, the interfacial water structures at the two basal planes of kaolinite were studied using MDS. The interfacial water structure at the kaolinite silica face and alumina face were examined using water density analysis, water dipole orientation analysis, and water residence time analysis.

Chapter 5 discusses the effect of isomorphous substitution in the silica tetrahedral layer on the surface hydrophobicity using molecular dynamics simulation. The contact angles at the silica tetrahedral surfaces with different degrees of isomorphous substitution were calculated based on the two-dimensional water density analysis. Moreover, the effect of isomorphous substitution on the interfacial water structure was also investigated. It is expected that these results will provide further understanding of the hydrophobicity of phyllosilicates from a theoretical point of view.

Chapter 6 discusses the anisotropic surface properties of chlorite. The charging characteristics of chlorite are first investigated by the electrophoresis method. Then the surface charging at chlorite mica-like and brucite-like basal planes is characterized using AFM by measuring the surface forces between a silicon nitride tip and the chlorite surface. The edge plane of chlorite has been prepared by ultramicrotome cutting technique and the surface charge of chlorite edge was determined by AFM surface force measurements.

Chapter 7 summarizes the findings of this dissertation research.

CHAPTER 2

BACKGROUND

The surface properties of phyllosilicate minerals are very important in mineral processing. For example, the surface charge and wetting characteristics of phyllosilicates significantly influence the separation efficiency in the flotation. In past decades, many efforts have been made to understand the surface chemistry of phyllosilicates. However, some of the surface properties of phyllosilicates still remain mysterious, since the investigation is quite challenging due to the submicron particle size and heterogeneous surface characteristics.

The objective of this chapter is to review the surface chemistry characteristics of the phyllosilicate minerals with regard to the recent surface charge results based on electrophoresis, titration, and atomic force microscopy (AFM) surface force measurements, and the wetting characteristics of phyllosilicate minerals using contact angle measurements and molecular dynamics simulation (MDS).

2.1 Review of the Surface Charging Characteristics of Phyllosilicates

The phyllosilicate minerals are expected to have a heterogeneous surface charge. The surface charge properties at the basal surfaces and edge surfaces of phyllosilicates were thought to be different (Schofield 1938; Schofield 1939; Swartzen-Allen and Matijevic 1974; Williams and Williams 1978). Traditionally, the basal surface of phyllosilicates were believed to carry a constant structural charge due to the isomorphous

substitution of Si^{4+} by Al^{3+} in the tetrahedral sheet or Mg^{2+}/Al^{3+} by Fe^{2+} in the octahedral sheet. The surface charge on the edges was considered to be pH-dependent, since the exposed broken bonds easily undergo the protonation/deprotonation reactions. Thus, the edge surface is expected to carry a positive charge in acidic solution, while in alkaline solution, the edge surface is negatively charged. The common techniques for determining the surface charging of phyllosilicates include electrophoresis, titration, and AFM surface force measurements. The results from literature will be reviewed in the following sections.

2.1.1 Electrophoresis

Electrophoresis is a common technique to determine the surface charge. According to the Stern's model, there are two layers surround the sample's surface. One is the Stern or Helmholtz layer where the ions are fixed to the surface and the other is the diffuse layer, also called the diffuse Gouy-Chapman layer. The schematic of Stern's model is shown in Figure 2.1. When a voltage is applied to the suspension, the potential at the slipping plane where the Stern layer ends and the diffuse layer begins is called the zeta potential (ζ-potential). The slipping plane is also known as the shear plane or outer Helmholtz plane. The pH where the zeta potential is zero refers to the iso-electric point (IEP), whereas the pH value where the surface potential is zero represents the point of zero charge (PZC). In the electrophoresis measurements, the mobility of the particles is measured under an applied electric field. Then the zeta-potential of the particles is calculated from the electrophoretic mobility using a mathematical model. The zeta-potential is largely affected by the pH value, ionic strength, and the type of ions in the electrolyte.

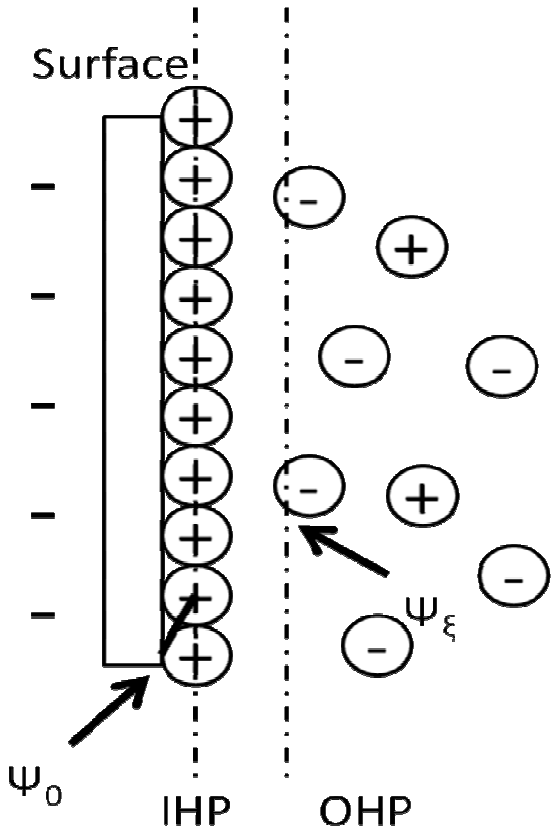

Figure 2.1 – Model of electrical double layer proposed by Stern. IHP refers to the inner Helmholtz plane and OHP refers to the outer Helmholtz plane. Ψ_0 is the surface potential and Ψ_ξ is zeta-potential at the OHP.

The surface charge of various types of phyllosilicates from electrophoresis measurements have been made and reported in the literature. For example, the isoelectric point (IEP) of kaolinite has been found to be lower than pH 3 using the electrophoresis technique (Hunter and James 1992; Johnson et al. 2000; Nicol and Hunter 1970; Williams and Williams 1978). Hu et al. claimed that the IEP of kaolinite is influenced by the ratio of silica content to alumina content in the sample. The alumina tends to increase the IEP to a higher level (Hu and Liu 2003). However, even in kaolinite with a higher alumina content, the determined IEP is still low, suggesting that the effect of alumina is not very significant.

Other bilayer phyllosilicates, including the halloysite, chrysotile (tubular structures), and antigorite (planar structure) have also been studied and discussed in the literature (Miller et al. 2007). The IEP of halloysite is lower than pH 3, which is similar to silica, due to the exposure of the silica tetrahedral sheet at the surface of the halloysite tube. On the other hand, since the tubular chrysotile has the magnesia octahedral sheet exposed, a higher IEP which is similar to the IEP of brucite (pH 11) is found. The planar antigorite has an intermediate IEP value between brucite and silica. These results suggest that the exposure of magnesia octahedral sheets and silica tetrahedral sheets are relatively equal in the antigorite lattice. The zeta-potentials of selected phyllosilicate minerals are listed in Table 2.1. The zeta-potentials of trilayer phyllosilicates have also been studied. Mica has a higher surface charge than talc, illite, and montmorillonite due to the greater extent of isomorphous substitution. Moreover, the contribution of isomorphous lattice substitutions to the zeta-potential has not been well understood.

It should be noted that the electrophoretic measurements do not consider the shape and anisotropic character of phyllosilicate particles. For example, when determining the zeta-potential using Smoluchowski's model, it is assumed that the particles have spherical shape and uniform surface charge. However, the phyllosilicate particles usually have platy shape and heterogeneous surface charge. So far, there is no satifactory model to describe the electrophoretic mobility of a platy phyllosilicate particle with anisotropic surface charging characteristics. Thus, it is not clear what the measured electrophoretic mobilities of phyllosilicate particles represent and such measurements do not provide sufficient detail to describe the anisotropic surface charging characteristics.

Table 2.1 – Electrophoretic zeta-potentials of selected clay minerals at neutral pH.

Clay Minerals	**Zeta-Potential, mV (neutral pH)**
Trilayer Clay Minerals	
Talc	-22 (Nalaskowski et al. 2006)
Illite	-35 (Hu, Liu, and Xu 2003)
Montmorillonite	-25 (Liu, Xu, and Masliyah 2004)
Mica	-71 (Hartley, Larson, and Scales 1997)
Bilayer Clay Minerals	
Kaolinite	-30 (Miller et al. 2007)
Halloysite	-41 (Miller et al. 2007)
Antigorite	-5 (Miller et al. 2007)
Chrysotile	+20 (Miller et al. 2007)
Other Clay Minerals	
Chlorite	-15 (Fornasiero and Ralston 2005)

2.1.2 Titration

Potentiometric titration is another technique which can be used to determine the point of zero charge (PZC) of a mineral suspension. The surface charge density is determined by monitoring the changes of pH when adding a certain amount of acid or base titrant (Ardizzone, Spinolo, and Trasatti 1995; Pokrovsky, Schott, and Thomas 1999). Then the surface charge density of the particles is calculated as:

$$\sigma = \left(\frac{F}{S}\right)\left(\left[C_a - C_b\right] - \left[H^+\right] + \left[OH^-\right]\right) \tag{2-1}$$

where σ is the surface charge density (C/m^2), S is the surface area (m^2/liter), F is Faraday's constant, and C_a and C_b are the amounts of acid and base titrant added (mol/liter).

It is noted that the potentiometric titration technique requires the surface area of the sample which is sometimes difficult to obtain. In this regard, Mular and Roberts

proposed a simplified titration method to determine the PZC. In this procedure, the change in pH (ΔpH) is measured when increasing the concentration of background electrolyte (Mular and Roberts 1966). When there is no effect of electrolyte on pH (ΔpH=0), the pH value refers to the PZC.

Using the titration method, the surface charge densities of some phyllosilicate minerals have been studied and the results have been reported in the literature. For example, Burdukow et al. reported that the PZC of talc is around pH 7.7 which is much higher than the PZC measured by electrophoresis (Burdukova et al. 2008). Alvarez-Silva et al. studied the surface charging of serpentine and chlorite using the Mular-Robers titration technique and their results show that the PZC values for serpentine and chlorite are found at pH 4.3 and 4.7, respectively, compared to the IEP of pH 4 and < 3 determined from electrophoresis. The PZC of kaolinite has been determined by potentiometric titrations by many researchers. The results are in the range of pH 4.3 to pH 4.6 (Brady, Cygan, and Nagy 1996; Motta and Miranda 1989). Some researchers considered the titration method to be a better technique as it is not affected by the particle shape. However, similar to the electrophoresis technique, the titration still can only give an overall surface charge density and the anisotropic surface charging characteristics of phyllosilicates are not defined.

2.1.2 Atomic Force Microscopy

As a powerful analytical tool, atomic force microscopy (AFM) has been applied to characterize the surface properties in a wide range of disciplines because of its nano scale resolution, simple sample preparation, and flexible working environment. The AFM has a laser beam reflected from the back side at the very end of a cantilever which usually

has a sharp tip or probe particle on the front side. The reflected laser which is detected by a photodetector acts as an optical lever allowing for nanometer measurements. The difference in voltage after the cantilever's deflection can be converted to the three-dimensional surface height image. Besides the high resolution imaging, AFM can also measure the forces between the cantilever's tip and the substrate. Both long-range and short-range colloidal forces as well as adhesion forces can be measured. The results are recorded as a cantilever deflection versus distance curve, which is then converted to a force versus distance curve. Further AFM description is given in Chapter 3.

Previous studies have reported that the surface charge density and surface potential can be calculated by fitting the AFM surface force curve with the theoretical DLVO model (Drelich, Long, and Yeung 2007; Yin and Drelich 2008). Using the AFM surface force measurement and the theoretical model fitting, the surface charging behaviors of some phyllosilicates have been determined and the results reported (Zhao et al. 2008). For instance, using the AFM direct colloid probe force measurement, Zhao et al. characterized the surface charging of mica basal planes. They observed monotonically repulsive forces at pH 6-10, indicating that the basal plane of mica is pH-independent. In addition, they prepared a molecularly smooth mica edge surface using the ultra microtome cutting technique and interrogated the mica edge surface using AFM. The results show that the mica edge surface is pH-dependent and the IEP is between pH 7 to pH 8. Yan et al. extended this research to the investigation of the surface charging of the talc basal surface and edge surface (Yan et al. 2011). Similar to mica, the basal surface of talc is negatively charged at pH 6- 10. The isoelectric point of the edge surface for the talc edge surface (~pH 8.1) is slightly higher than that for muscovite (~pH 7.5),

apparently due to the difference in the strength of the Al-OH and Mg-OH surface acid groups. Recently, Gupta and Miller successfully developed a method to deposit kaolinite particles at the surface of glass and fused alumina substrates with exposure of the silica face and alumina face, respectively (Gupta and Miller 2010). Then the well-ordered kaolinite particles were interrogated by AFM surface force measurements. Their results suggest that the surface charging of the kaolinite silica face and alumina face is different. The kaolinite silica face has an IEP lower than pH 4, whereas the IEP of the kaolinite alumina face is between pH 6 to pH 8. These results are very helpful in explaining the mechanism of the kaolinite aggregation phenomena.

2.2. Review of Surface Wetting Characteristics of Phyllosilicates

Recently, more and more efforts have been devoted to the study of phyllosilicates' wettability using a variety of techniques. Of these techniques, contact angle measurement is one of the most prevailing methods to determine the hydrophobicity of phyllosilicates. It measures the angle between the tangent line of the liquid/vapor interface and liquid/solid interface. The thermodynamic balance of the interfacial energy and contact angle is expressed by Young's equation:

$$\gamma_{sv} = \gamma_{sl} + \gamma_{lv} \times \cos\theta \tag{2-2}$$

where γ_{sv}, γ_{sl}, γ_{lv} are the surface tension of the solid/vapor, solid/liquid, and liquid/vapor interfaces, respectively, and θ is the contact angle. The schematic of a liquid droplet on a solid surface forming contacts lines between the three phases (solid, liquid, and vapor) is shown in Figure 2.2.

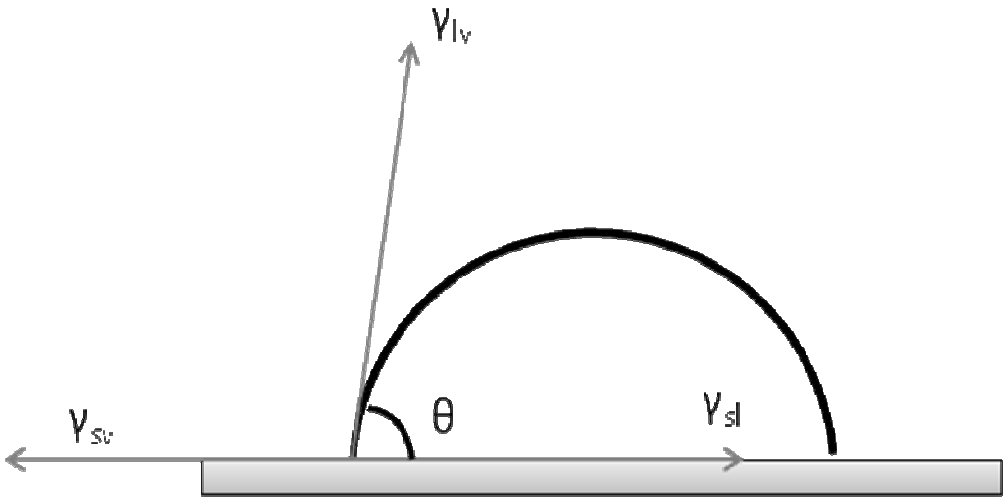

Figure 2.2 – Wetting and thermodynamic equilibrium for a liquid droplet on a rigid solid surface. γ_{sv}, γ_{sl}, γ_{lv} are the surface tension of the solid/vapor, solid/liquid, and liquid/vapor interfaces and θ is the contact angle.

The surface wetting characteristics are usually described by the magnitude of contact angle. When a water droplet easily spreads over the surface with a contact angle close to zero, the surface is considered to be hydrophilic. According to different surface characteristics, the contact angle may range from 0˚ to 180˚. The surface with larger contact angle corresponds to stronger surface hydrophobicity. When the contact angle is above 150˚, the surface is known as a super-hydrophobic surface.

In the real situation, the surface is not ideal and it may demonstrate more than one contact angle. Thus, the concept of advancing contact angle (largest contact angle when liquid tends to advance) and receding contact angle (smallest contact angle when liquid tends to recede) help to describe the surface wetting characteristics. The difference between the advancing and receding contact angle is known as the contact angle hysteresis which indicates the deviation of the surface from ideality. For an ideal surface, the advancing contact angle is equivalent to the receding contact angle.

Experimentally, the contact angle can be determined by using various techniques, including sessile drop, captive bubble, capillary rise, Wihelmy method, etc. However, contact angle measurements are influenced by many factors, including surface roughness, surface preparation, temperature, humidity, sample pretreatment, and experimental procedures. It is known that almost all the surfaces in nature are rough (to a certain extent) and it has been noticed that the contact angle is significantly affected by the surface roughness. In this regard, Wenzel took the surface roughness into consideration and modified the equation as:

$$\cos\theta' = r\cos\theta \tag{2-3}$$

where θ' is the apparent contact angle which is observed by optical microscope and r is the roughness factor which is defined as the ratio between the actual and projected surface area. As the roughness factor r is always greater or equal to 1, the apparent contact angle decreases with surface roughness when contact angle is less than 90˚, while the surface roughness increases the apparent contact angle of the hydrophobic surface with contact angle is greater than 90˚.

Besides surface roughness, the surface heterogeneity has also been investigated in previous research. Cassie derived an equation to determine the contact angle for a smooth but chemically heterogeneous surface as:

$$\cos\theta' = f_1\cos\theta_1 + f_2\cos\theta_1 \tag{2-4}$$

where θ' is the apparent contact angle, θ_1 and θ_2 are the contact angle for two regions with different surface properties, and f_1 and f_2 are the fractions of the two regions.

Using contact angle measurements to determine the wetting characteristics of phyllosilicate minerals is quite challenging, since the results may be affected by the particle size, surface heterogeneity, sample preparation, organic matter, and adsorption phenomena. The water contact angles for selected clay minerals, including talc, pyrophyllite, illite, muscovite, and kaolinite using different techniques are summarized in Table 2.2.

Table 2.2 – Water contact angles for pyrophyllite, illite, and muscovite.

Clays	**Preparation**	**Technique**	**Contact Angle (Degrees)**	**Reference**
Talc(basal)	Cleaved	Sessile drop (adv)	64.0	(Nalaskowski et al. 2007)
Talc (edge)	Cut	Sessile drop (adv)	31.0	(Nalaskowski et al. 2007)
Talc (basal)	-	-	62.0	(Fuerstenau and Huang 2003)
Talc (edge)	-	-	13.0	(Fuerstenau and Huang 2003)
Talc (basal)	Cleaved	Sessile drop	90.0	(Kaggwa et al. 2006)
Pyrophyllite	Polished	Sessile drop	47.0	(Hu, Liu, and Xu 2003)
Illite	Clay film	Sessile drop	34.2	(Shang et al. 2010)
Illite	Polished	Sessile drop	12.0	(Hu, Liu, and Xu 2003)
Muscovite	Cleaved	Captive drop	10.0	(Bryant, Bowman, and Buckley 2006)
Kaolinite	Polished	Sessile drop	15.0	(Hu, Liu, and Xu 2003)
Kaolinite	Clay film	Sessile drop	16.9	(Shang et al. 2010)
Kaolinite	Clay film	Sessile drop	46.1	(Wu 2001)

Shang et al. compared sessile drop, Wihelmy plate, thin layer wicking, and column wicking methods to determine contact angles of different clay minerals including kaolinite, illite, and smectite. They found considerable differences in the results from the different experimental techniques for the same sample (Shang et al. 2008). For example, variations in contact angle for illite ranged from 24.0˚ to 56.8˚. The water contact angles were little affected by humidity between 19% and 75%. However, a decreased contact angle was observed at 100% relative humidity which may be due to expansion of the adsorbed water film. In addition, they claimed that the effect of cations on contact angles for kaolinite, illite, and smectite was very small.

Generally, the wettability of phyllosilicate minerals is believed to be determined by their crystalline structure. For example, the silica tetrahedral basal plane of phyllosilicates with perfect lattice arrangement (no isomorphous substitution) is electrically neutral. The surface with this saturated valence siloxane structure has a very low polarity and low affinity to water molecules which results in strong hydrophobicity. An example is the talc/pyrophyllite surface. Both of these minerals have a trilayer structure with an octahedral sheet sandwiched between two silica tetrahedral sheets. There is almost no lattice substitution and the contact angle for the basal planes of talc and pyrophyllite is in the range of 50˚ to 70˚. On the other hand, when isomorphous substitutions are present in the phyllosilicate lattice, the surface wetting characteristics change significantly. For example, muscovite which is also a trilayer phyllosilicate has 25% percent of the silicon atoms in the silica tetrahedral sheet substituted by aluminum atoms. These isomorphous substitutions lead to a net surface charge deficiency which is compensated by the interlayer cations. As a result, due to the charge imbalance and the

nature of ionic interlayer forces, muscovite is a naturally hydrophilic mineral with a contact angle of 10˚ or less. Thus, the isomorphous substitution plays a very important role on the surface wettability of phyllosilicates' basal planes.

The edge surface of phyllosilicates is expected to have different wetting characteristics from basal plane surfaces. Nalaskowski et al. compared the surface properties of the talc basal plane surface and edge surface from contact angle measurements, atomic force microscopy, and streaming potential measurements (Miller et al. 2007). The results show that the edge of talc is hydrophilic due to the exposure of broken Si-O and Al-O bonds. This finding is also confirmed by the molecular dynamics simulations (Du and Miller 2007a).

Kaolinite is a type of bilayer phyllosilicate. The bulk kaolinite is usually considered as a hydrophilic material. The structure of kaolinite can be described as alternating sheets of silica tetrahedra and aluminum octahedra. The bilayers are bonded together by hydrogen bonds between the hydroxyl ions of the octahedral sheet and the oxygen atoms of the silica tetrahedral sheet. Ideally, when kaolinite is cleaved, both a silica tetrahedral face and an alumina octahedral face will be exposed. Kaolinite has an extremely small degree of isomorphous substitution relative to a perfect lattice. Therefore, in this regard, some extent of hydrophobicity for the kaolinite silica face can be expected. In fact, some research has already shown evidence of kaolinite's hydrophobicity (Durand and Rosenberg 1998; Kaminsky et al. 2009; Saada, Siffert, and Papirer 1995). Saada et al. compared the hydrophobicity of kaolinite and illite from asphaltene and water adsorption isotherms. They found that kaolinite displays a higher affinity for asphaltenes and a lower affinity for water than does illite (Saada, Siffert, and

Papirer 1995). Kaminsky et al. carried out a detailed clay mineralogical analysis for froth streams and tailings streams during the extraction of bitumen from oil sand (Kaminsky et al. 2009). The results from their analysis showed that kaolinite and chlorite tend to be enriched in the froth solids, suggesting a significant interaction of bitumen with kaolinite and chlorite surfaces. Durand et al. used cryo-SEM to investigate the distribution of oil in the kaolinite- and illite-bearing cores (Durand and Rosenberg 1998). They found that after aging, fibrous illite had no affinity for oil and that kaolinite has an affinity for oil, as do platy illite particles which behave as kaolinite. Therefore, they claimed that the bulk wettability of clays depends not only on the nature of clays, but also on the morphology, amount, and distribution. All these findings provide indirect evidence about the hydrophobic character of kaolinite. Direct evidence regarding the wettability of the kaolinte silica face and alumina face has not been reported.

Using the method of molecular dynamics simulation, Miller et al. also found a difference in the wetting behavior for the two faces of kaolinite (Miller et al. 2007). Their results suggest that the silica tetrahedral face of kaolinite should be hydrophobic, similar to pyrophyllite and talc (Du and Miller 2007a), due to the observation of an exclusion zone between interfacial water and the silica tetrahedral face. In contrast to the silica tetrahedral sruface, water molecules are tightly bonded with the alumina octahedral surface, indicating the hydrophilic character of alumina octahedra. This hydrophilic characteristic was explained by the presence of surface hydroxyl groups which can provide plenty of hydrogen bonding sites and facilitate the formation of strong hydrogen bonds (Du and Miller 2007a; Wang et al. 2005). Recently, the MDS results from Solc's group confirmed this finding and they calculated a contact angle for the kaolinite silica

face of about 105˚, whereas the alumina face is hydrophilic (Šolc et al. 2011). However, the detailed analysis on the interfacial water structure of the two kaolinite faces has not been reported.

CHAPTER 3

ATOMIC FORCE MICROSCOPY FOR PROBING WETTABILITY

3.1 Introduction

The surface wettability of minerals plays a very important role in mineral flotation, not only in bubble attachment but also in froth stability, and in tailings sedimentation (Dang-Vu et al. 2009; Hu, Liu, and Xu 2003; Hu et al. 2005; Liu, Xu, and Masliyah 2004). In previous studies, many techniques have been applied to investigate the wettability of clay minerals, for example, contact angle measurements on packed particle beds or thin particle films (Hu, Liu, and Xu 2003; Nalaskowski et al. 2007; Shang et al. 2008; Shang et al. 2010). However, such measurements are quite challenging for phyllosilicate minerals due to their anisotropic characteristics and nano scale particle size. Moreover, the surface roughness, sample preparation, temperature, humidity, sample pretreatment, and experimental procedures may also influence the results. Therefore, in order to avoid these effects, we employed surface force measurements using atomic force microscopy (AFM) to characterize the wettability based on the presence and magnitude of the surface force between a hydrophobic diamond-like-carbon AFM tip and the surfaces of interest.

In the absence of electrostatic and steric repulsive forces, the hydrophobic force is often observed as an attractive force between two hydrophobic surfaces. It is of importance in many interfacial processes, including the protein conformation, micellar

formation, surfactant adsorption/desorption, and stability of colloidal suspensions (Bremmell, Jameson, and Biggs 1999; Isrealachvili 1985; Wolgemuth, Workman, and Manne 2000). The hydrophobic force has been found to be both short-range and long-range (Eriksson, Ljunggren, and Claesson 1989; Israelachvili and Pashley 1984; Nalaskowski, Drelich, and Miller 2008; Yoon and Ravishankar 1996). Israelachvili and Pashley first measured the hydrophobic force with a distance about 10 nm between two hydrophobized mica surfaces using the surface force apparatus (SFA). In later studies, the hydrophobic force is reported for a very wide range of distances from 10 nm to over 100 nm (Wood and Sharma 1995). Although the hydrophobic force has been observed in many systems using different techniques, the origin of the hydrophobic force is still under debate. The current main theories to explain the hydrophobic force include:

(1) Nano Bubble Bridging. Due to the nonpolar nature of hydrophobic surfaces, they are likely to accommodate the small air bubbles from the aqueous solution. When two solid surfaces carrying such nano bubbles approach each other, a strong attractive capillary force may be present. The presence of nano bubbles at the hydrophobic surface has been confirmed by AFM imaging (Tyrrell and Attard 2001). According to this theory, the distance of the hydrophobic force is expected to be related to the size of nano bubbles.

(2) Water Structure. From molecular dynamics simulation results, it has been reported that the interfacial water structure at a hydrophobic surface is quite different from that at a hydrophilic surface. A gap between the water phase and the hydrophobic surface with thickness of 1 Å to 3 Å is found, also called the exclusion zone (Du and Miller 2007a; Du and Miller 2007b; Sendner et al. 2009). Moreover, the spectrum

collected by sum frequency vibrational spectroscopy (SFVS) suggests that the water structure at the hydrophobic surface is more like the water structure at the vapor/liquid interface. A large number of water molecules without hydrogen bonding are present at the interface (Miranda and Shen 1999; Du, Freysz, and Shen 1994; Shen, Nihonyanagi, and Uosaki 2001). This unique interfacial water structure at the hydrophobic surface may result in an attractive solvation force when two hydrophobic surfaces approach. Recently, the exclusion zone between water and a hydrophobized silicon surface was confirmed by Reichert et al. performing x-ray reflectivity measurements at the high-energy beamline ID15A, European Synchron Radiation Facility, using the surface and interface scattering instrument HEMD for high-energy microdiffraction (Mezger et al. 2006). In their approach, the reflected intensity was recorded by an x-ray detector and then the density profile across the interface was calculated based on a theoretical model. The measured thickness of the gap is approximately between 0.1 and 0.5 nm. Moreover, they found the dissolved gas (Ar, Xe, Kr, N_2, O_2, CO and CO_2) and HCl have no effect on the water depletion zone.

(3) Electrostatic Origin. In this theory, the hydrophobic force is explained by the mobile charges or dipoles adsorbed at the surface which result in a high local polarization (Tsao, Evans, and Wennerstrom 1993). Then the rearrangement of water molecules at the interface would lead to an attractive electrostatic van der Waals-like force. Recently, Hanly et al. studied the effect of electrostatic interaction on the surface wettability and they reported that the wettability of a titania surface reaches the maximum at its isoelectric point. Moreover, the wettability decreases with increasing electrolyte concentration (Hanly et al. 2011).

In the past decade, many researchers have investigated the hydrophobic force in different systems using AFM (Hampton and Nguyen 2009; Isrealachvili 1985; Nalaskowski, Drelich, and Miller 2008; Wallqvist et al. 2006; Zhang, Yoon, and Eriksson 2007; Zhang et al. 2005). It has been reported that the hydrophobic force increases with an increase in water contact angle (Yoon and Ravishankar 1996). A common AFM-based technique for measuring the hydrophobic force is known as the colloidal probe technique in which a chemical hydrophobized spherical particle with a particle size of 5 to 50 μm is used as the AFM tip. The measured hydrophobic force can be long-range and have a large magnitude. However, this type of colloidal AFM tip cannot provide the high resolution image and the size of these colloidal tips is too large to measure the surface forces for nano-size clay particles. Hence, a technique which is able to measure the surface force, specifically the hydrophobic force for such nano-size particles, is desirable. Moreover, the chemical reagents used to hydrophobize the colloidal AFM tips may also influence the results of surface force measurements. In this regard, a naturally hydrophobic material which is known as diamond-like-carbon was selected as the AFM tip, in order to avoid chemical effects.

The objective of this chapter is to describe the development of a new AFM-based technique to characterize the surface wettability and demonstrate its validity. The charging behavior of the diamond-like-carbon (DLC) tip was first characterized by measuring the surface forces at a well-cleaned glass substrate. Then surface force measurements were performed between the DLC tip and two hydrophobized silica surfaces with different degrees of hydrophobcity to demonstrate the validity of this technique.

3.2 Materials and Methods

3.2.1 Sample Preparation

Two fused silica samples were used as the substrates. First, the fused silica samples were thoroughly cleaned using the SC1 procedure in which the samples were boiled in a solution containing water, H_2O_2, and NH_4OH with a ratio of 5:1:1 for 20 min (Nalaskowski et al. 2003). Using this method, the organic and inorganic contaminants can be removed from the sample surfaces. In order to prepare silica surfaces of different hydrophobicity, two octadecyltrichlorosilane (OTS) solutions with different concentrations were prepared using 50 ml benzene mixed with 0.25g and 0.025g OTS. The concentrations for the OTS solutions were calculated as 1.29×10^{-2} mol/L and 1.29×10^{-3} mol/L. To obtain a complete dispersion, the solutions were stirred for 30 min using a magnetic stirrer. One of the silica samples was placed into the high-concentration OTS solution and another sample was placed in the low-concentration OTS solution. Reaction with silica surface was for about 1 min. After removal from the solution, the samples were rinsed with chloroform to clean the excess OTS solution. Finally, the hydrophobized silica samples were placed in an oven at 100˚ C for 4 hrs. Then the silica samples were ready to be used as the hydrophobized reference substrates.

3.2.2 Surface Force Measurements Using AFM

A picoforce AFM with Nanoscope V controller and PF scanner (Bruker Corporation, Santa Barbara, CA) was used for the surface force measurements. An AFM fluid cell was used to contain and control the aqueous environment. A contact mode AFM cantilever (Budget Sensors, Sofia, Bulgaria) and a tip coated with a thin layer of hydrophobic diamond-like-carbon (DLC) was used. The thickness for this diamond-like-

carbon coating is about 15 nm. The micrographs of the DLC tip were taken by field emission scanning electron microscopy (FE-SEM) with 20000× and 150000× magnification, as shown in Figure 3.1.

The accelerating voltage was set to 3kV and 5kV, respectively. The tip curvature radius was measured by fitting a circle to the tip apex and calculated by comparing with the scale bar shown on the graph. The tip radius thus determined is around 15 nm to 20 nm. This value is in good agreement with the value determined by the manufacturer. The spring constant provided by the manufacturer is about 0.2 N/m. The exact spring constant was determined by the thermal tuning function provided with the Nanoscope v 7.20 software and this value is used later in data analysis. The technical information regarding the DLC tip is summarized in Table 3.1.

In order to characterize the surface charging of the DLC tip as a function of pH, surface force measurements between the DLC tip and a thoroughly cleaned glass substrate were carried out in 1 mM KCl with varying pH values. The cleaning procedure has been described in the ref. (Nalaskowski et al. 2003). Five random locations at the surface were selected, and at each location, five force curves were recorded. The collected approaching force curves were fitted with the theoretical DLVO model to calculate the surface charge density and surface potential at each pH value.

The surface force measurements were also performed in 1mM KCl at pH 4 between the DLC tip and two hydrophobized silica surfaces. For each sample, five different locations were selected and five force measurements were made at each location.

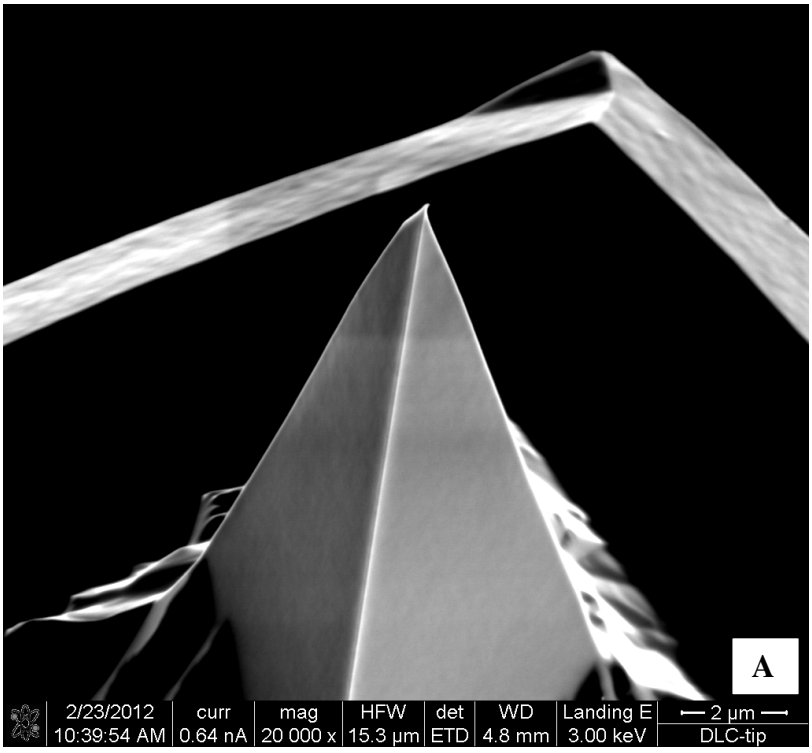

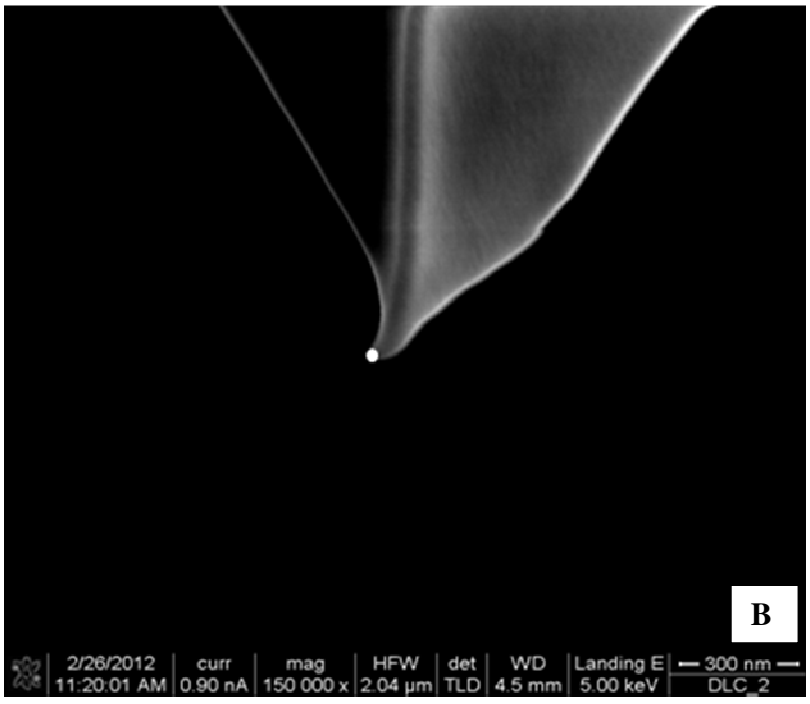

Figure 3.1 – Micrographs of diamond-like-carbon AFM tip taken by field emission scanning electron microscope under 20000× magnification (A) and 150000× magnification (B).

Table 3.1 – Specification information for DLC tip.

	Value	Range
Resonant Frequency	13 kHz	± 4 kHz
Spring Constant	0.2 N/m	0.07 N/m to 0.4 N/m
Length	450 μm	± 10 μm
Mean Width	50 μm	± 5 μm
Thickness	2 μm	± 1 μm
Tip Height	17 μm	± 2 μm
Tip Set Back	15 μm	± 5 μm

All surface force measurements were performed at a scan rate of 1 Hz and captured at a resolution of 512 points. Approach force curves were then analyzed with SPIP software (Image Metrology, Lyngby, Denmark).

3.2.3 Theoretical Model

The force curves collected from AFM surface force measurements for determination of the surface charge density for the DLC tip were fitted with the DLVO (Derjaguin-Landau-Verwey-Overbeek) theoretical model in which only the van der Waals force and electrical double layer force are considered. A constant surface charge density and surface element integration for spherical-flat plate geometry were used in the calculation (Assemi, Nguyen, and Miller 2008; Bhattacharjee and Elimelech 1997). The equations are expressed as:

$$F_{(SEI)} = \frac{4\pi\sigma_1\sigma_2 e^{-\kappa h}}{\varepsilon\varepsilon_0\kappa^2}\left\{e^{-2\kappa R} + \kappa\mathrm{Re}^{-2\kappa R} + \kappa R - 1\right\} + \frac{2A(h,\kappa)R^3}{3h^2(h+2R)^2} \tag{3-1}$$

The first term in eq. (3-1) refers to the electrical double layer force, whereas the second term refers to the van der Waals force. σ_1 is the surface charge density of the substrate and σ_2 is the surface charge density of the tip, κ^{-1} is the Debye length, h is the separation distance, R is the tip radius, and ε and ε_0 are the permittivity of water and vacuum. A is the Hamaker-Lifshitz function which is defined by (Fa, Nguyen, and Miller 2006; Nguyen and Schulze 2004):

$$A(h,\kappa) = (1+2\kappa h)e^{-2\kappa h}A_0 + A_1(h) \tag{3-2}$$

The first term in eq. (3-2) represents the Keesom and Debye dipolar (zero-frequency) contributions to the Hamaker constant. It is calculated from the static dielectric constant of water and surfaces, given by:

$$A_0 = \frac{3kT}{4}\sum_{m=1}^{\infty} m^{-3}\left(\frac{80-\varepsilon_1}{80+\varepsilon_1}\times\frac{80-\varepsilon_2}{80+\varepsilon_2}\right) \tag{3-3}$$

where ε_1 and ε_2 are the static dielectric constants of the substrates and AFM tip, k is the Boltzmann constant and T is the absolute temperature.

The second term is the non-zero frequency contribution of the dispersion interaction, which is expressed as:

$$A_1(h) = \frac{3\hbar\omega}{8\sqrt{2}}\frac{(B_1-B_3)(B_2-B_3)}{(B_1-B_2)}\left(\frac{I_2(h)}{\sqrt{B_2+B_3}} - \frac{I_1(h)}{\sqrt{B_1+B_3}}\right) \tag{3-4}$$

where ħ is the Planck constant divided by 2π and ω is the absorption frequency in UV (about 2×10^{16} rad/s for water). B_1, B_2 and B_3 are the square of the refractive index for the substrate, the AFM tip and water. $I_1(h)$ and $I_2(h)$ are the electromagnetic retardation terms given by:

$$I_i(h) = \left\{1 + (h/\lambda_i)^q\right\}^{-1/q} \tag{3-5}$$

where q=1.185. The characteristic wavelengths, λ_j, are given by:

$$\lambda_j = \frac{v}{\pi^2\omega}\sqrt{\frac{2}{B_3(B_j + B_3)}} \tag{3-6}$$

where v is the speed of light in the vacuum. The refractive index and dielectric constant for diamond-like-carbon, glass, and water are listed in Table 3.2 (Isrealachvili 1985; Nguyen and Schulze 2004; Rosenholtz and Dudley 1936; Smietana et al. 2007).

The surface potential of the DLC tip was calculated from the surface charge density using the following equations (Yin and Drelich 2008):

$$c_0 = c_\infty \exp(-\frac{z_i e\Psi}{kT}) \tag{3-7}$$

Table 3.2 – Parameters for the calculation of van der Waals force.

	Refractive index	Dielectric constant
Diamond-like-carbon	1.8	4.20
Glass	2.10	3.81
Water	1.33	80

$$c_0 - c_\infty = \frac{\sigma^2}{2\varepsilon\varepsilon_0 kT} \tag{3-8}$$

$$c_\infty = \frac{\kappa\varepsilon\varepsilon_0 kT}{e^2 z^2} \tag{3-9}$$

where Ψ is the surface potential, k is the Boltzmann constant, T is the absolute temperature, e is the electronic charge, z is the valency of the ions, c_0 is the ionic concentration at the surface, and c_∞ is the ionic concentration in the bulk at x=∞ where $\Psi(\infty) = 0$.

The hydrophobic force may be involved in the surface forces collected between the DLC tip and clay mineral surfaces. This hydrophobic attraction force was fitted with an empirical single exponential equation:

$$\frac{F_{hydrophobic}}{R} = -C\exp(-\frac{h}{D}) \tag{3-10}$$

where C and D are fitting parameters. The total surface force is obtained by the summation of DLVO force and hydrophobic force:

$$F = F_{(SEI)} + F_{hydrophobic} \tag{3-11}$$

3.2.4 Contact Angle Measurements

The advancing and receding water contact angles for each silica sample were determined by a contact angle goniometer using the sessile drop technique. For each

sample, at least five drops were measured. The average values from the five measurements were calculated.

3.3 Results and Discussions

3.3.1 Determination of Charge Regulation for the DLC Tip

The charging behavior of the DLC tip is essential in this research, since the electrostatic interaction needs to be avoided when measuring the hydrophobic force from which the wettability is characterized. Therefore, it is necessary to determine the isoelectric point of the DLC tip before measuring surface forces at the substrates of interest. The surface force measurements were conducted between a DLC tip and a thoroughly cleaned glass substrate in 1mM KCl at varying pH values. The glass substrate is completely hydrophilic with contact angle of 0˚. It is expected that there is no hydrophobic interaction present in this system.

Figure 3.2 illustrates some examples of collected surface force curves as a function of separation distances. For a common AFM surface force curve, when the tip and the substrate are in large separation, a straight line is observed, indicating that there is no interaction and the force is zero. When the tip is brought closer to the surface, the cantilever's tip senses the substrate through long-range or short-range forces from which the repulsion force or attractive force are identified. After the tip contacted the substrate and as the sample continues to press the tip, the cantilever is deflected mechanically and strong resistance force is observed. After reaching the maximum approach distance, the sample is retracted again.

As shown in Figure 3.2, repulsive forces were observed when the pH value was greater than 4 and their magnitude increased with increasing pH. It is known that the isoelectric point of the glass is around pH 2; therefore, the glass substrate should be negatively charged in this pH range. The observation of repulsive forces indicates that the DLC tip is negatively charged above pH 4. At pH 4, no interaction was observed, suggesting that the electrostatic interaction is absent and the isoelectric point of the DLC tip should be around pH 4. In order to confirm this finding, the surface force measurements were also performed between the DLC tip and the glass substrate in 5mM and 10 mM KCl at pH 4. As shown in Figure 3.3, similar to the force curves collected for 1mM KCl at pH 4, no interaction was observed in either of these two electrolyte solutions. It suggests that the surface force is not affected by the ionic strength at this pH value and the absence of interaction is not from the cancellation of other surface forces. All these results suggest that the isoelectric point of the DLC tip is around pH 4.

Fitting with the theoretical DLVO model, the surface charge density and surface potential of the DLC tip at different pH values were calculated. The surface charging of the glass substrate at different pH values was taken from reference (Gupta and Miller 2010) and used in these calculations. The surface potential of the DLC tip was then calculated from the surface charge density using eqs. (3-7) to (3-9). The results, shown in Figure 3.4, suggest that the isoelectric point of the DLC tip is around pH 4 and the surface charge remains relatively constant above pH 4. The following AFM experiments to determine the wettability of phyllosilicate minerals were all performed at pH 4, where electrostatic interactions are insignificant.

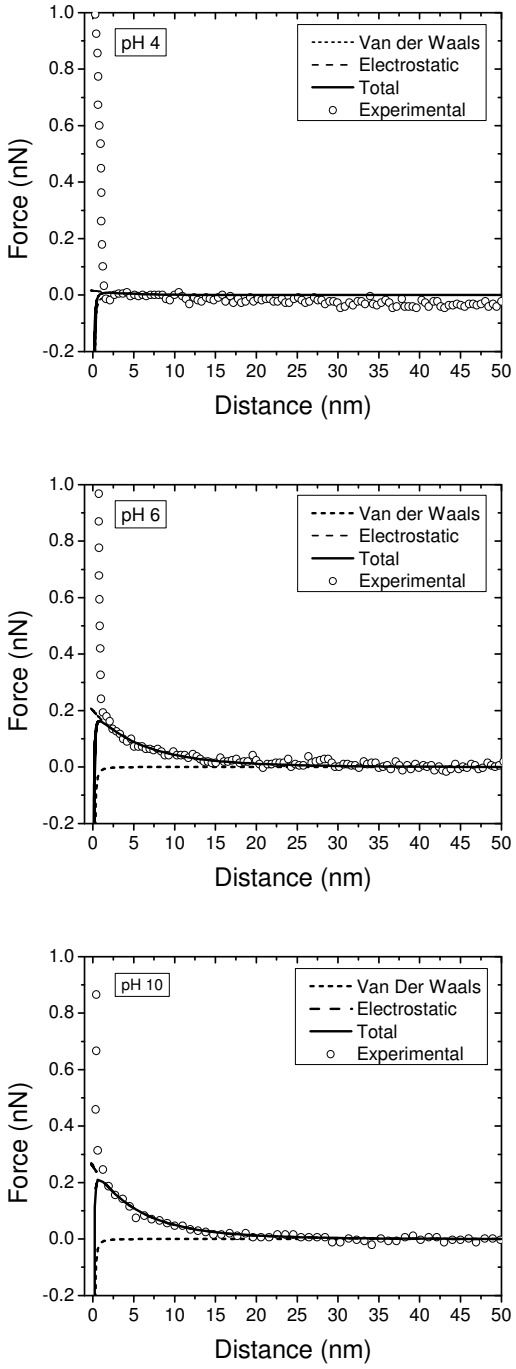

Figure 3.2 – Interaction force curves between a DLC tip and a glass substrate in 1mM KCl at pH 4, pH 6, and pH 10. The solid and dashed lines represent the theoretical DLVO fit.

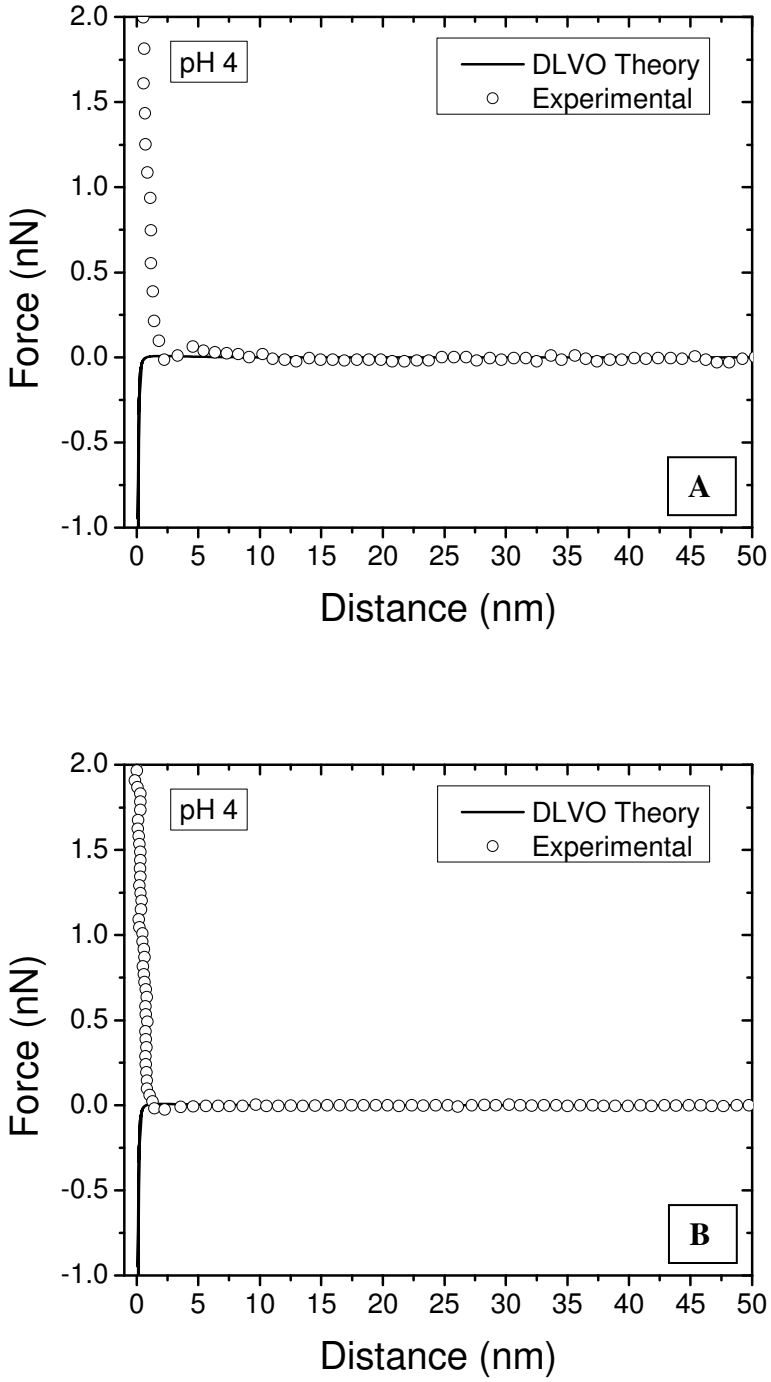

Figure 3.3 – Interaction force curves between a DLC tip and a glass substrate in 5mM (A) and 10 mM (B) KCl at pH 4. The solid line represents the theoretical DLVO fit.

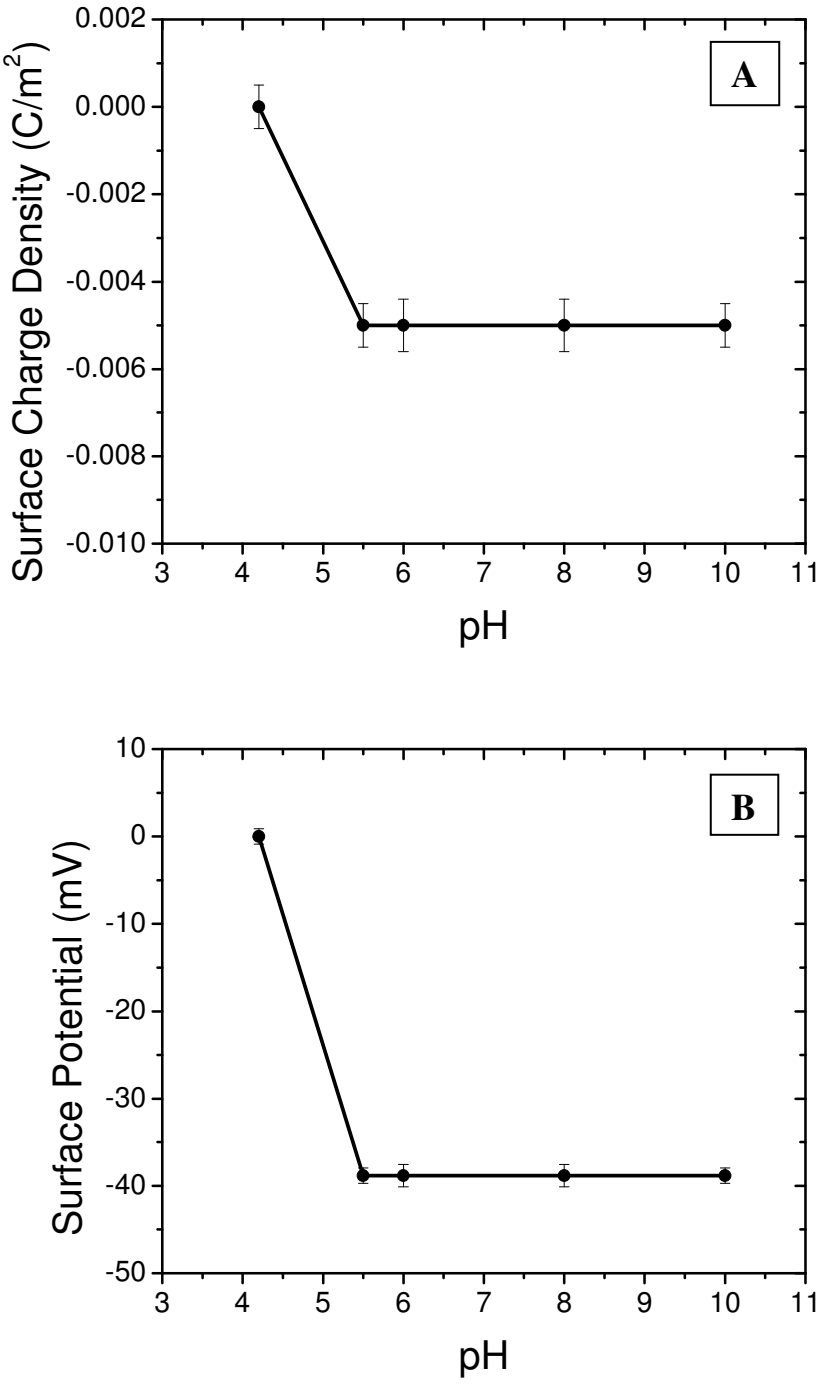

Figure 3.4 – The surface charge density (A) and surface potential (B) of the diamond-like-carbon AFM tip as a function of pH determined by fitting the surface force curves with the DLVO model.

3.3.2 Interaction Forces at Silica Substrates with Different Hydrophobicity

In order to demonstrate the capability of this AFM-based technique for determining the surface wetting characteristics, the surface force measurements were performed between the DLC tip and the two silica substrates having a different level of hydrophobicity. Two silica samples were hydrophobized in the OTS solutions with different concentrations to obtain different hydrophobic surface states. The advancing and receding contact angles for these two hydrophobized samples as well as the concentration of OTS solution are presented in Table 3.3. The concentration of OTS for the preparation of sample 1 is ten times higher than the OTS concentration for sample 2. The advancing contact angle for sample 1 and sample 2 are 104˚ and 72˚, respectively. These results suggest that the hydrophobicity of the silica substrates can be controlled by adjusting the concentration of OTS solution and sample 1 has a greater contact angle than sample 2, due to the higher concentration OTS solution used in the preparation.

The interaction forces between the DLC tip and two silica substrates with different levels of hydrophobicity were measured in 1mM KCl at pH 4 which is close to the isoelectric point of the DLC tip. At this pH value, it is expected that the electrical double layer force is insignificant. As shown in Figure 3.5, the jump-to-contact distance for sample 1 is 11 nm, whereas the jump-to-contact distance for sample 2 is around 5 nm, suggesting that sample 1 showed a stronger attractive hydrophobic force than sample 2.

Table 3.3 – Water contact angles for the silica substrates with different hydrophobicty.

Sample	Advancing Contact Angle(˚)	Receding Contact Angle(˚)	OTS Concentration
1	104±3	95±2	1.29×10^{-2} M
2	72±1	64±2	1.29×10^{-3} M

The hydrophobic force at the two hydrophobized silica substrates were obtained by subtracting the contribution of the van der Waals force from the total surface force. After normalizing with the tip radius, the hydrophobic force curve was fitted with a single exponential function, as shown in eq. (3-10). The fitted hydrophobic force curves are shown in Figure 3.6 and the fitting parameters C and D are listed in Table 3.4. The decay length (D) for sample 1 and sample 2 are 3.5 nm and 2.0 nm, respectively. The parameter C which represents the magnitude of the hydrophobic force for sample 1 and sample 2 are -120 mN/m and -30 mN/m, respectively. These results demonstrate that the magnitude of the detected hydrophobic force correlates with the contact angle and this technique can be used to characterize surface hydrophobicity. Because of the high resolution of AFM surface force measurement, this technique is especially suitable for investigating the surface properties of phyllosilicates of submicron particle size.

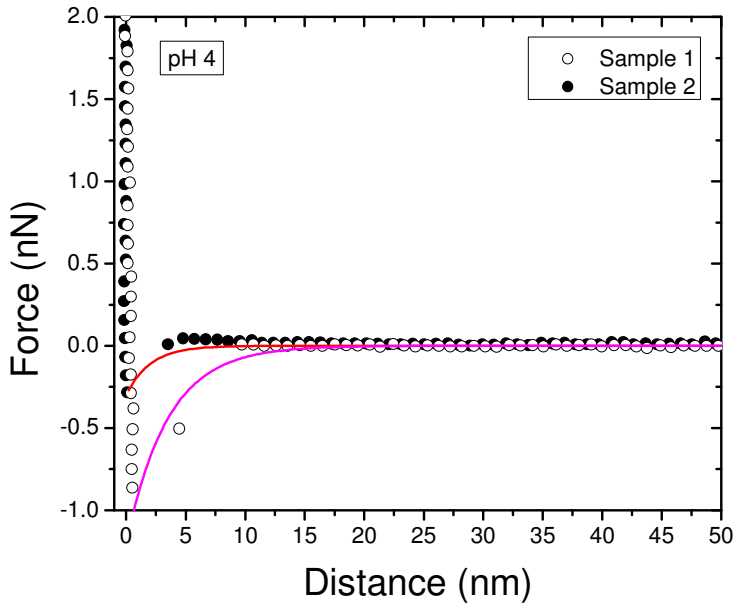

Figure 3.5 – Interaction forces between the DLC tip and the hydrophobized silica substrates with different wetting characteristics in 1mM KCl at pH 4. The solid line represents the fitted hydrophobic force.

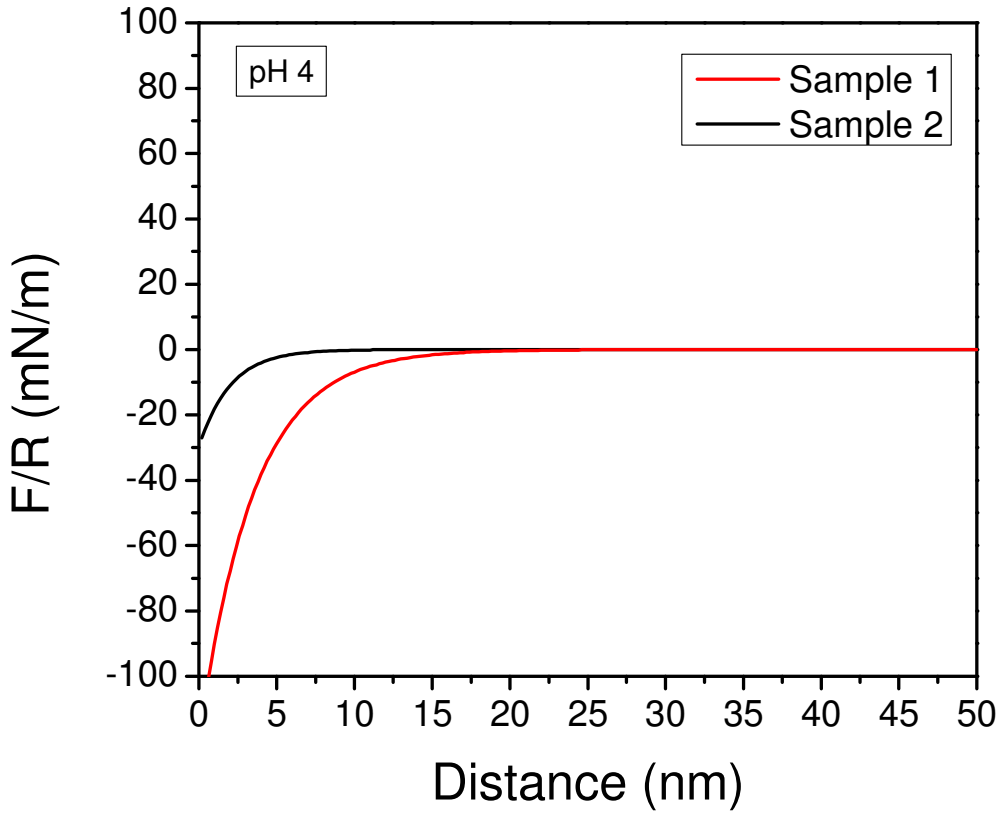

Figure 3.6 – Comparison of fitted hydrophobic force measured at the two hydrophobized silica substrates.

Table 3.4 – Comparison of fitting parameters of the hydrophobic forces for the silica substrates with different hydrophobicity.

	C (mN/m)	D (nm)	θa(˚)	θr(˚)
Sample1	-120	3.5	104±3	95±2
Sample2	-30	2.0	72±1	64±2

3.4 Summary

An AFM-based technique was developed to determine the wetting characteristics of surfaces. Force measurements were performed between reference silica surfaces and a hydrophobic diamond-like-carbon AFM tip. The hydrophobicity was determined by the magnitude of the hydrophobic attraction force. The surface charging behavior of the DLC tip was characterized by measuring the surface force between the DLC tip and a hydrophilic glass substrate. Fitting with the DLVO theoretical model, the isoelectric point of the DLC tip was determined to be ~pH 4. It is expected the effect of electrostatic interaction can be eliminated at this pH value. To demonstrate the validity of this technique, the surface force measurements were carried out at two hydrophobized silica substrates with different wetting characteristics. Attractive hydrophobic forces were observed for both of the two substrates and the magnitude of the hydrophobic force for the sample with a higher contact angle was found to be greater than for the sample with a small contact angle. The results suggest that this AFM-based technique can be utilized to describe the hydrophobic surface state and is used to examine the hydrophobic character of kaolinite basal planes which is discussed in Chapter 4.

CHAPTER 4

SURFACE CHEMISTRY OF KAOLINITE BASAL PLANES

4.1 Introduction

Kaolinite is an important and valuable material for the paper making industry, the ceramic industry, and other industries. Frequently, however, in mineral processing operations, kaolinite and other phyllosilicate minerals are considered as gangue minerals which can bring problems during flotation and tailings disposal. Therefore, the surface properties, especially the wetting characteristics of kaolinite, play a critical role in the recovery and production of kaolinite as well as in the separation of other minerals from kaolinite. In past decades, some effort has been made on the investigation of kaolinite wettability. Kaolinite has an extremely small degree of isomorphous substitution relative to a perfect lattice, and in this regard, some extent of hydrophobicity for the kaolinite silica face can be expected.

Characterization of kaolinite wettability is quite challenging, since unlike muscovite and talc which are found as pure and large crystal specimens with atomically smooth surfaces suitable for contact angle measurements, kaolinite, illite, and many other clay minerals are commonly found as small, submicron particles. Consequently, the effects of particle size, roughness, surface heterogeneity, and anisotropy impact contact angle measurements whether the measurement is made by the clay film technique or by the capillary rise technique. The objective of this chapter is to characterize the wettability

of kaolinite 001 and 00$\underline{1}$ basal planes using atomic force microscopy. The measurements are performed between a hydrophobic diamond-like-carbon (DLC) tip and well-ordered kaolinite particle substrates. The results are compared with the corresponding surface force curves obtained for the well-known talc and mica surfaces. The origin of the observed hydrophobic forces is then discussed in terms of the van der Waals interaction under the consideration of the water exclusion zone at such hydrophobic surfaces. Moreover, molecular dynamics simulation is utilized to further explain the interaction between water molecules and kaolinite surfaces.

4.2 Materials and Methods

4.2.1 Sample Preparation

A pure, untreated kaolinite sample with a particle size of less than 2 μm was obtained from the St. Austell area in Cornwall, UK (Imerys Inc., UK). The kaolinite particles with size around 500 nm were prepared as a 1 g/L suspension with a pH of 5.5 in high purity Milli-Q water (Millipore Inc). Two ordered kaolinite substrates were prepared using the technique developed by Gupta et al. (Gupta and Miller 2010). By using this sample preparation technique, kaolinite particles can be successfully ordered, as confirmed by observing the difference in surface charge density at the two kaolinite faces. In one case, the kaolinite particles are deposited from suspension on a glass substrate which is cleaned following the SC1 procedure (Nalaskowski et al. 2003). In this cleaning process, the glass substrates were cleaned in a 5:1:1 mix of H_2O:NH_4OH:H_2O_2 solution, at 80 ˚C for 20 min, followed by rinsing with high purity Milli-Q water, and dried with ultra high purity N_2 gas.

At pH 5.5, the positively charged kaolinite alumina face is more favorable to attach to the negatively charged glass surface, thus leaving the kaolinite particles with their silica tetrahedral face exposed. For the other case, the alumina octahedral face is exposed on an alumina substrate since the negatively charged kaolinite silica face is more likely to attach to the positively charged alumina substrate. The schematic of this kaolinite deposition procedure is displayed in Figure 4.1. The deposited particles are air-dried overnight in a petri-dish cover, and then sonicated in water for 1 min to remove loosely attached particles. Finally, the samples are rinsed with water and dried by N_2 gas.

High quality muscovite and talc samples were obtained from the Curator at the College of Mines and Earth Sciences, University of Utah. Two freshly cleaved muscovite and talc sheets were mounted on a standard sample puck using double sided tape for subsequent surface force measurements.

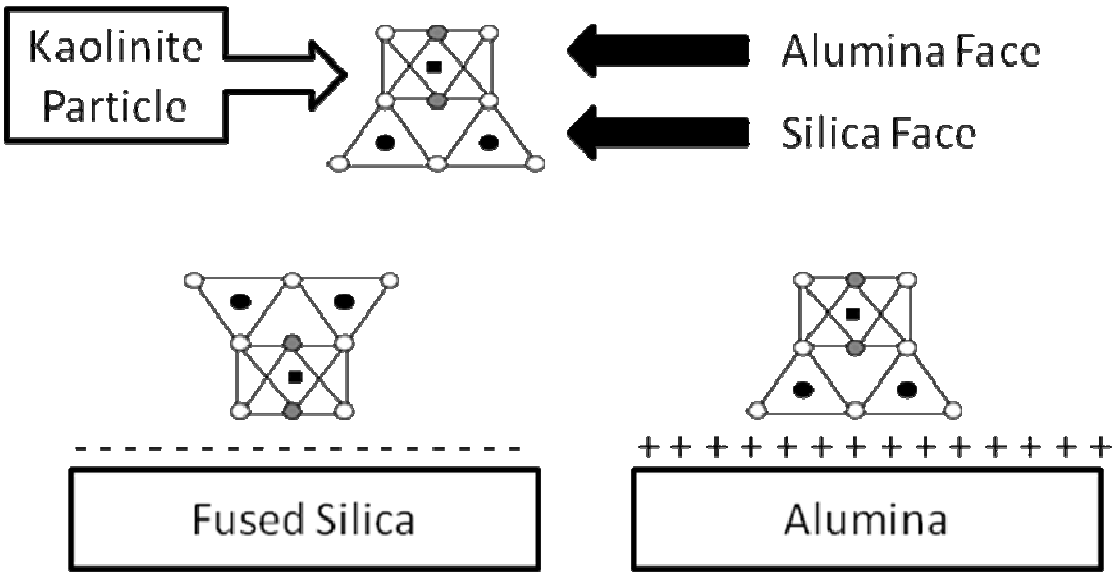

Figure 4.1 – Schematic of kaolinite particle deposition procedure.

4.2.2 Surface Force Measurements Using AFM

A picoforce AFM with a Nanoscope V controller (Bruker Corporation, Santa Barbara, CA) was used with a PF-type scanner designed for picoforce measurements. Contact mode AFM cantilevers (Budget Sensors, Sofia, Bulgaria) and tips coated with a thin layer of hydrophobic diamond-like-carbon (DLC) were used in this research. The spring constant was determined by the manufacturer as 0.12 N/m. The tip had a radius of curvature of 15 nm.

In order to understand the hydrophobicity of kaolinite, talc and muscovite substrates were used as reference samples due to their well-known hydrophobic and hydrophilic characteristics. The advancing and receding water contact angles for talc and muscovite samples were measured by the sessile drop technique using a contact angle goniometer. The results show that the advancing and receding contact angles are 75˚ and 69˚ for the talc basal plane, 9˚ and 7˚ for the muscovite basal plane. These contact angle results are in good agreement with results reported in the literature (Nalaskowski et al. 2007; Bryant et al. 2006)

The surface force measurements were conducted at the muscovite and talc surfaces at five different locations in 1 mM KCl at pH 4. At the kaolinite substrates, an AFM image was first obtained under contact mode with a scan size of 5 microns and scan rate of 1 Hz. Then the surface force measurements were performed on the kaolinite particles in 1 mM KCl at pH 4 using the point and shoot feature of the software. In this study, about 10 to 15 kaolinite particles were selected for each sample. All the force measurements were performed at a scan rate of 1 Hz and captured at a resolution of 512 points/measurement. SPIP software (Image Metrology, Lyngby, Denmark) was used to

convert the deflection-distance curves to force-distance curves. Baseline correction and hysteresis correction were involved in preparation of the force curves.

4.2.3 Theoretical Model

The force curves collected from AFM surface force measurements were fitted with the DLVO (Derjaguin-Landau-Verwey-Overbeek) theoretical model plus the single exponential hydrophobic force model. Details about the theoretical model have been discussed in the Section 3.2.3. The final equation can be expressed as:

$$F_{(SEI)} = \frac{4\pi\sigma_1\sigma_2 e^{-\kappa h}}{\varepsilon\varepsilon_0\kappa^2}\left\{e^{-2\kappa R} + \kappa \mathrm{Re}^{-2\kappa R} + \kappa R - 1\right\} + \frac{2A(h,\kappa)R^3}{3h^2(h+2R)^2} - RC\exp(-\frac{h}{D}) \quad (4\text{-}1)$$

where the first term refers to the electrical double layer force, the second term refers to the van der Waals force, and the third term is the hydrophobic force. σ_1 is the surface charge density of the substrate and σ_2 is the surface charge density of the tip, κ^{-1} is the Debye length, h is the separation distance, R is the tip radius, ε and ε_0 are the permittivity of water and vacuum, C and D are fitting parameters for hydrophobic force, and A is the Hamaker-Lifshitz function which is described in Section 3.2.3. The van der Waals parameters, refractive index, and dielectric constant, for diamond-like-carbon, glass, kaolinite, talc, and muscovite are listed in Table 4.1.

When the surface force measurements of talc, muscovite, and kaolinite were performed at the pH value which is close to the point of zero charge of the DLC tip, the electrostatic interaction is eliminated and only van der Waals and hydrophobic interactions need to be considered.

Table 4.1 – Parameters for the calculation of van der Waals force (Isrealachvili 1985; Nguyen and Schulze 2004; Rosenholtz and Dudley 1936; Smietana et al. 2007).

	Refractive index	Dielectric constant
Diamond-like-carbon	1.8	4.20
Glass	2.10	3.81
Kaolinite	1.56	11.18
Talc	1.54	9.41
Muscovite	1.55	10.00
Water	1.33	80

4.2.4 Molecular Dynamics Simulation

MD simulation package Amber 9 was used for the analysis of interfacial water structure at the kaolinite silica face and alumina face surfaces (Case et al. 2005). A simple cubic cell (26 × 27 × 40 Å) containing the kaolinite surface and 700 water molecules was constructed with periodic boundary conditions. The initial configuration of the kaolinite surface was created according to the lattice parameters provided by American Mineralogist Crystal Structure Database (Bish and Von Dreele 1989). The number of atoms for the kaolinite surface is listed in Table 4.2. The simple point charge (SPC) water model (Berendsen 1981), together with the CLAYFF force field (Cygan, Liang, and Kalinichev 2004) were used to describe the water interactions. The intermolecular potential parameters are listed in Table 4.3.

Table 4.2 – Number of atoms in the kaolinite surface.

Species	Number of atoms
Silicon	60
Bridging oxygen	90
Hydroxyl oxygen	120
Hydroxyl hydrogen	120
Octahedral oxygen	60
Aluminum	60

Table 4.3 – Potential parameters for kaolinite/water interaction.

Species	Charge [e]	ε [Kcal/mol]	σ [A]	Ref
Silicon	2.1	1.84×10^{-6}	3.706	(Cygan, Liang, and Kalinichev 2004)
Bridging oxygen	-1.05	0.1554	3.165	(Cygan, Liang, and Kalinichev 2004)
Hydroxyl oxygen	-0.95	0.1554	3.165	(Cygan, Liang, and Kalinichev 2004)
Hydroxyl hydrogen	-0.42	0	0	(Cygan, Liang, and Kalinichev 2004)
Octahedral oxygen	-1.05	0.1554	3.165	(Cygan, Liang, and Kalinichev 2004)
Aluminum	1.575	1.33×10^{-6}	4.794	(Cygan, Liang, and Kalinichev 2004)
Water hydrogen	0.41	0	0	(H. J. C. Berendsen 1981)
Water oxygen	-0.82	0.1554	3.169	(H. J. C. Berendsen 1981)

The pair potential force field used in the simulations is given as a combination of the Lennard-Jones and the Coulomb electrostatic interactions, and can be expressed as:

$$U_{pair} = \sum_i \sum_j \left(4\varepsilon \left[\left(\frac{\sigma_{ij}}{r_{ij}} \right)^{12} - \left(\frac{\sigma_{ij}}{r_{ij}} \right)^{6} \right] + \frac{q_i q_j}{r_{ij}} \right) \tag{4-2}$$

where ε is the energy parameter, σ is the size parameter, q is the charge, and r is the distance between species i and j. Lorentz-Berthelot mixing rules were applied to calculate the potential parameters of pairs:

$$\varepsilon_{ij} = \sqrt{\varepsilon_i \varepsilon_j} \tag{4-3}$$

$$\sigma_{ij} = \frac{\sigma_i + \sigma_j}{2} \tag{4-4}$$

Following the procedure reported in previous studies (Du and Miller 2007b, Kirkpatrick, Kalinichev, and Wang 2005, Wang et al. 2010), the kaolinite crystal was simulated as a NPT assembly with the pressure fixed at 0.1 Mpa and the temperature fixed at 298 K. After adding water molecules into the system, the simulations were performed with periodic conditions under NVT assembly using Hoover's thermostat (Melchionna, Ciccotti, and Holian 1993). The Ewald sum has been used to account for the electrostatic interactions. The Leapfrog method with a time step of 1 fs was used to integrate the particle motion. A total simulation time of 1.5 ns including an equilibrium time of 500 ps was applied. The results were analyzed based on the last 1 ns in the simulation (10^6 steps of 1 fs).

4.3 Results and Discussion

4.3.1 Interaction Forces at Talc and Muscovite Substrates

The interaction forces between a hydrophobic DLC tip and talc, and muscovite surfaces were measured in 1mM KCl at varying pH values. Five regions were selected to conduct the surface force measurements. Examples of the force-distance curves for talc and muscovite surfaces are shown in Figures 4.2 and Figure 4.3, respectively. It is known that the isoelectric points for talc and muscovite are below pH 4 (Hartley, Larson, and Scales 1997; Nalaskowski et al. 2007). Thus, these two minerals are negatively charged at pH = 4 in a KCl solution. The surface charge densities of talc and muscovite at different pH values used in the calculation of DLVO theoretical curves were taken from ref. (Nalaskowski et al. 2007).

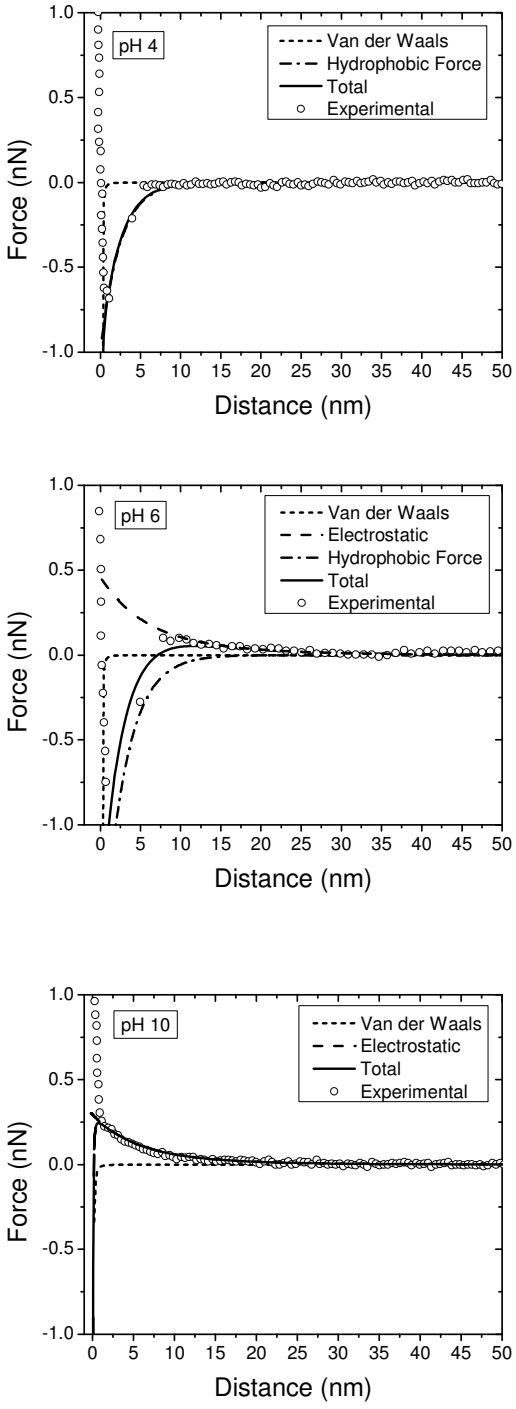

Figure 4.2 – Interaction forces measured between a hydrophobic DLC tip and the talc basal plane surface in 1mM KCl at pH 4, pH 6, and pH 10. The solid lines represent the theoretical fit, including the DLVO forces and hydrophobic force.

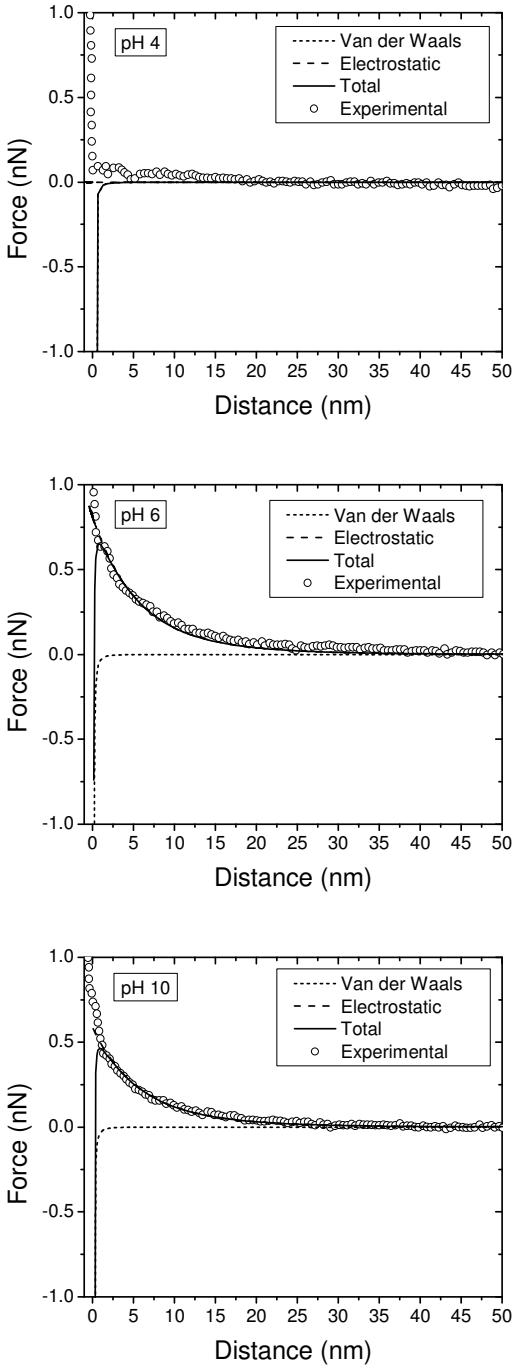

Figure 4.3 – Interaction forces measured between a hydrophobic DLC tip and the muscovite basal plane surface in 1mM KCl at pH 4, pH 6, and pH 10. The solid lines represent the theoretical DLVO fit.

At pH 4, a relatively strong attraction force with a distance of 7 to 10 nm was observed at the talc surface. Since pH 4 is close to the isoelectric point of the DLC tip, the electrostatic interaction should be very weak. Moreover, calculated from the theoretical model, the van der Waals forces for both of these two systems were found to be of very short range (<2 nm). This is in agreement with the common understanding that the van der Waals force is usually present as an attractive force within a distance of 5 nm (Isrealachvili 1985). The observed attraction force at the talc surface is found at a distance of 7 nm to 10 nm, which is much greater than the distance for the calculated van der Waals force. Hence, this attraction force should be attributed to the hydrophobic interaction. In contrast, no interaction was observed at the muscovite surface, confirming the hydrophilic nature of muscovite.

At pH 6, besides a short-range attraction force, a weak repulsion force appeared at the talc surface with a separation distance between 10 nm to 30 nm. These results indicate that the electrostatic force increases due to the increasing negative surface charge of the DLC tip as well as that of the talc surface (see Figure 4.2). However, this electrostatic interaction still cannot overcome the hydrophobic force at these short distances. The same surface charge effect was observed for the DLC/muscovite system (see Figure 4.3). The results suggest that at both the DLC tip and the muscovite surface are negatively charged at pH 6.

When the pH value is increased to pH 10, repulsive forces were found at both talc and muscovite surfaces. It suggests that the electrostatic interaction overcomes the hydrophobic interaction in the case of talc basal plane surface and dominates the surface force.

4.3.2 Interaction Forces at the Kaolinite Silica and Alumina Surfaces

The kaolinite particles in suspension (~pH 5.5) were deposited on a glass substrate and an alumina substrate. At this pH, the glass substrate is negatively charged and the kaolinite alumina face with positive charge tends to attach to the glass substrate. On the other hand, the kaolinite silica face with negative charge tends to attach to the positively charged alumina substrate. In this way, the silica face and alumina face of kaolinite particles are exposed when the particles are then ordered as described in Section 4.2.1.

Figure 4.4 and Figure 4.5 show the AFM images of kaolinite particles on the glass and fused alumina substrates. The particles have an average size of 500 nm and about 1 nm in thickness. The surface force measurements were then performed at the particles surfaces using the point and shoot function of the software.

The surface force measurements were performed between a DLC tip and the kaolinite basal plane surfaces in 1mM KCl at pH 4 which is the isoelectric point of DLC and under these circumstances, the electrostatic interaction is insignificant. Examples of the force curves are shown in Figure 4.6. It is noted that an attractive force between the kaolinite silica face and the hydrophobic AFM tip was observed. This attraction is greater than the calculated theoretical van der Waals force, suggesting that the hydrophobic interaction contributes significantly. However, the magnitude of this hydrophobic force is smaller than that observed for the talc surface. These results show that the kaolinite silica face has a modest level of hydrophobicity.

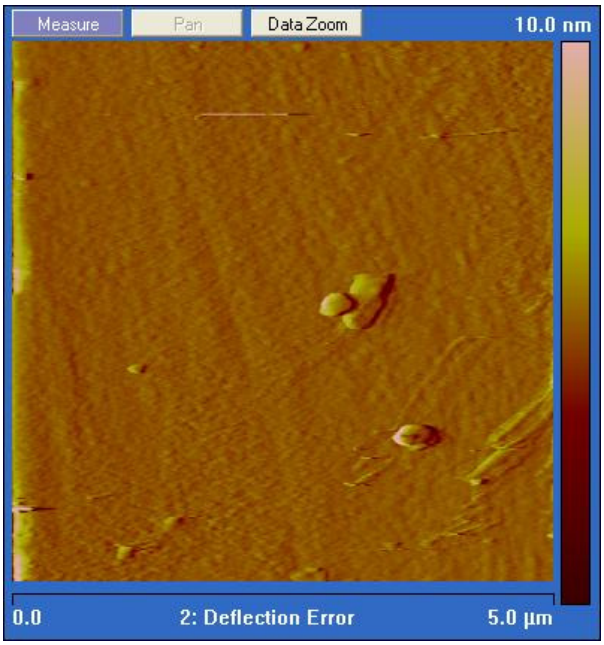

Figure 4.4 – Topographic AFM images of kaolinite particles deposited on glass. The image was obtained using a DLC tip in the contact mode before measuring the surface force on the particles.

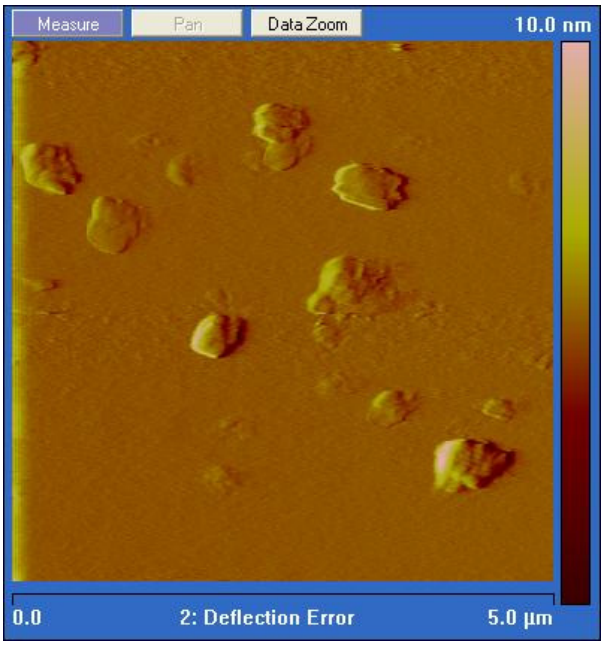

Figure 4.5 – Topographic AFM images of kaolinite particles deposited on fused alumina substrate. The image was obtained using a DLC tip in the contact mode before measuring the surface force on the particles.

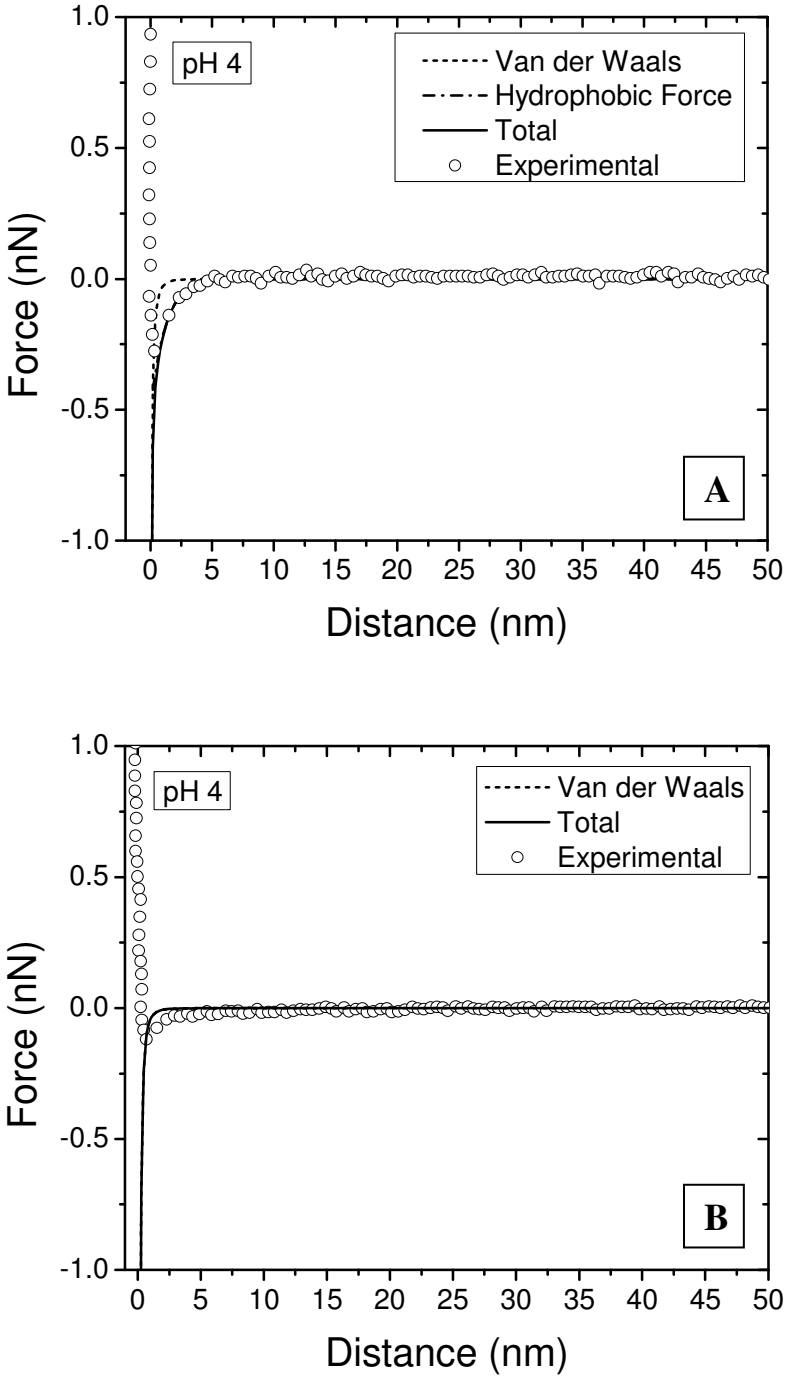

Figure 4.6 - Interaction forces measured between a hydrophobic DLC tip and a kaolinite-silica face (A) and a kaolinite-alumina face (B) in 1mM KCl at pH 4. The solid lines represent the theoretical fit, including the van der Waals force and hydrophobic force.

The kaolinite silica face has the same structure as the talc basal surface; however, the results show that the kaolinite silica face is less hydrophobic than the talc surface. This may be due to some isomorphous substitutions in the kaolinite lattice. It has been reported that natural kaolinite has various defects, including substitution of Mg, Ca, and Fe. The concentrations vary from 0.07% to 0.71% for Mg, 0.14% to 0.54% for Ca, and 0.07% to 0.31% for Fe (Frost et al. 2004; Wang and Chen 2004). These ismorphous substitutions may lead to a slight charge imbalance which could influence the interaction between water molecules and the kaolinite surface. A detailed discussion regarding the effect of isomorphous lattice substitution on the hydrophobicity of the phyllosilicate silica tetrahedral surface is discussed in Chapter 5.

Parameters C and D were obtained by fitting the normalized hydrophobic force to the single-exponential function eq. (3-10) to further compare with the wetting characteristics of the talc surface. The AFM surface force curves measured at pH 4 (the isoelectric point for the DLC tip) were selected and the hydrophobic force was obtained by subtracting the contribution of the van der Waals force from the total force. The fitted hydrophobic force curves for talc and the kaolinite silica face as well as the two hydrophobized silica substrates after normalization with the tip radius are shown in Figure 4.7.

Table 4.4 shows the value of C and D for the muscovite basal plane, talc basal plane, and kaolinite silica face in comparison with the hydrophobized silica substrates. Also, the advancing and receding water contact angle (θ_a and θ_r) for muscovite, talc, and hydrophobized silica substrates are listed for comparison.

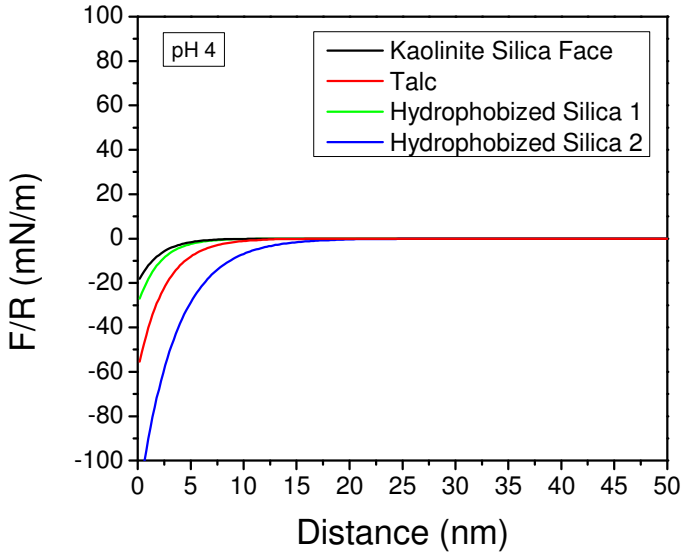

Figure 4.7 - Comparison of fitted hydrophobic force measured at the silica tetrahedral basal surface of talc and kaolinite as well as the two hydrophobized silica substrates.

Table 4.4 – Fitting parameters used to determine the hydrophobic force parameters for talc basal plane, kaolinite silica face, and two hydrophobized silica substrates. *The advancing and receding contact angle for the kaolinite silica face was obtained by comparing the fitting parameters C and D with talc and hydrophobized silica samples.

	C (mN/m)	D (nm)	θa(˚)	θr(˚)
Talc	-63	2.5	75	69
Kaolinite Silica Face	-20	2.0	64*	58*
Hydrophobized Silica (1)	-120	3.5	104	95
Hydrophobized Silica (2)	-30	2.0	72	64

The decay lengths (D) of the talc and kaolinite silica face are 2.5 and 2.0, respectively. This short decay length may be attributed to the small tip radius of the DLC cantilever which results in a weak hydrophobic attraction force. Subramanian studied the hydrophobic force between mica surfaces in the presence of a secondary amine using the surface force apparatus (SFA) and correlated the results with contact angle measurements (Subramanian 1998). Zhang et al. also presented the relationship between hydrophobic

force and contact angle by measuring the surface force between a silica sphere and a fused silica plate in octadecyltrimethylammonium chloride solutions using AFM (Zhang et al. 2005). However, due to the difference in techniques and the difference in systems studied, it is difficult to compare their results with our study. In this regard, we compared the fitting parameters C for the kaolinite silica face with that for talc and the two hydrophobized silica substrates. Since DLC tips were used in all these experiments, the results from these surface force measurements should be comparable. Assuming the influence from the decay length D is insignificant and the contact angle has a linear relationship with parameter C, a rough estimation of the contact angle of the kaolinite silica face can be obtained. As shown in Table 4.4, the advancing and receding contact angle of the kaolinite silica face were estimated as 64˚ and 58˚, respectively. The estimated contact angles for the kaolinite silica face are only slightly smaller than that for talc, suggesting that the kaolinite silica face has a moderate hydrophobicity.

As shown in Figure 4.6 (B), only a very small attraction, in the range of the van der Waals force region, was found for the kaolinite alumina face. This result indicates that the alumina face of kaolinite is relatively hydrophilic. From the crystal structure perspective, the kaolinite silica face has a hexagonal ring structure which offers no hydrogen bonding sites, whereas the alumina face has a layer of hydroxyl groups at its surface where water molecules are easily hydrogen bonded, resulting in a hydrophilic surface state. It should be noted that there were some inconsistencies during the surface force measurements at the kaolinite alumina face. Some particles showed an attraction force with magnitude similar to the kaolinite silica face. This may be due to a mixed-layer structure in some kaolinite particles in which case the two faces of the kaolinite

particle may both be a silica face. Another reason may be the imperfection in the sample preparation process. When the kaolinite particles are deposited on the substrate, some particles may flip over to inadvertently expose a silica face.

4.3.3 The Calculation of van der Waals Forces

Although the hydrophobic force has been recognized in many systems by various techniques, its origin is still under debate. In this research, short-range attractive hydrophobic forces were observed between the hydrophobic DLC tips and hydrophobic substrates using AFM, for example, the talc basal plane surface. Previous research has been reported that a water void, or water exclusion zone, is present at the hydrophobic surface as supported by the molecular dynamics simulation and x-ray reflectivity measurements (Du and Miller 2007a; Mezger et al. 2006). The thickness of this exclusion zone is estimated as several angstroms. When taking this water exclusion zone into consideration, the van der Waals interaction between two hydrophobic surfaces should be influenced by the thickness of this exclusion zone. Such analysis has been used to explain the attractive van der Waals force between a bubble and a hydrophobic surface (Wang, Yin, and Miller 2012). In this regard, the van der Waals force between the kaolinite silica face and the DLC tip was calculated taking into consideration the water exclusion zone. The effect of the exclusion zone thickness on the magnitude of the attractive van der Waals interaction was examined. It is expected this analysis may help to explain the origin of the hydrophobic force.

The existence of a general attractive interaction between neutral atoms or molecules was first discovered by van der Waals in 1873 to account for certain

anomalous phenomena occurring in nonideal gases and liquids (van Oss 1994). These nonelectrostatic intermolecular interactions were subsequently named "van der Waals forces." They are composed of three different, but closely related, phenomena:

1. Randomly orienting dipole-dipole interactions, described by Keesom. Keesom energies are proportional to the fourth power of the dipole moment (μ):

$$V_{Keesom} = -\frac{\mu^4}{kTD^6} \tag{4-4}$$

2. Randomly orienting dipole-induced dipole interactions, described by Debye. Debye energies are proportional to the polarizability (α) and to the square of the dipole moment (μ):

$$V_{Debye} = -\frac{\alpha\mu^2}{D^6} \tag{4-5}$$

3. Fluctuating dipole-induced dipole interactions, described by London. London energies are proportional to the characteristic energy (hν):

$$V_{London} = -\frac{3\alpha^2 h\nu}{4D^6} \tag{4-6}$$

where D is the interatomic distance, k is the Boltzmann's constant, and T is the absolute temperature. All three interactions (Keesom, Debye and London) decrease as a function of distance D, and are treated together as the total van der Waals interactions.

The dispersion (van der Waals-London) interaction energy for large bodies by a pair-wise summation of the properties of the individual molecules was first calculated by

Hamaker. Using this approximation, the total attractive dispersion energy per unit area for two semi-infinite flat parallel bodies, separated by a distance D, can be calculated:

$$F_{vdw} = \frac{A_{ii}}{6\pi D^3} \tag{4-7}$$

The total constant A_{ii}, controlling the interaction between the two bodies at short distances is called the Hamaker constant. For two materials 1 and 2, immersed in medium 3, the combining rules are described by:

$$A_{132} = \left(\sqrt{A_{11}} - \sqrt{A_{33}}\right)\left(\sqrt{A_{22}} - \sqrt{A_{33}}\right) \tag{4-8}$$

Based on the classical van der Waals theory, Israelachvili derived the expressions for the nonretarded dispersion forces between macroscopic bodies with adsorbed surface layers (Israelachvili 1972). When two solid surfaces with thin adsorbed layers of another component adsorption approach together in aqueous solution, the interface can be considered as five phases, solid, adsorbed layer, liquid, adsorbed layer, and solid. The schematic of this scenario is shown in Figure 4.8.

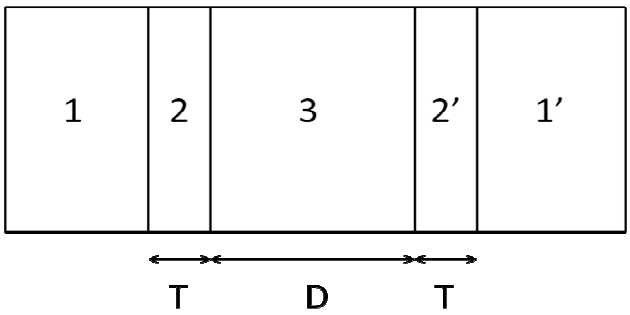

Figure 4.8 – Schematic of the interface between two solid surfaces with adsorbed thin layers. 1 and 1’ represent two solid surfaces. 2 and 2’ represent the adsorbed thin layers. T and T’ represent the thickness of the adsorbed layers. 3 represents the liquid medium and D is its thickness.

The derived equation for the calculation of the van der Waals forces between two solid surfaces with adsorbed thin layers is given as:

$$F(D) = \frac{1}{6\pi}\left[\frac{A_{232'}}{D^3} - \frac{\sqrt{A_{121} \times A_{32'3}}}{(D+T)^3} - \frac{\sqrt{A_{1'2'1'} \times A_{323}}}{(D+T')^3} + \frac{\sqrt{A_{1'2'1'} \times A_{121}}}{(D+T+T')^3}\right] \quad (4\text{-}9)$$

where F(D) is the van der Waals force per unit area, D is the thickness of the liquid phase, T and T' are the thickness of the adsorbed thin layer, and A_{abc} is the Hamaker constant between a and c in the medium b. This equation indicates that the van der Waals interaction is dominated by the properties of the solid surfaces when the separation distance is much greater than the thickness of the adsorbed thin layer. In contrast, when the separation distance is close to the thickness of the adsorbed thin layer, the van der Waals interaction is mainly controlled by the properties of the adsorbed layers.

Using this equation, the van der Waals force between the kaolinite silica face and the DLC tip was calculated where the thickness of the water exclusion zone (gas phase) at the surfaces was considered. The values of the nonretarded Hamaker constant of the kaolinite silica face, diamond-like-carbon, and water are shown in Table 4.5. The Hamaker constant for the gas phase is considered as zero. The Hamaker constant of the combined system was calculated using eq. (4-8). Figure 4.9 shows the calculated van der Waals force between the kaolinite silica face and the DLC tip as a function of separation distance. It can be noted that the magnitude of the van der Waals force increases with an increase in the thickness of the exclusion zone. When the exclusion zone is 0.2 – 0.5 angstroms in thickness, the jump-to-contact distance is in a range of 1 nm to 2 nm which is in the normal van der Waals region.

Table 4.5 – The Hamaker constant for the calculation of van der Waals force.

Phase		Hamaker constant
1	Kaolinite silica face	6.8×10^{-20}
2	Gas	0
3	Water	3.7×10^{-20}
2’	Gas	0
1’	Diamond-like-carbon	15.45×10^{-20}

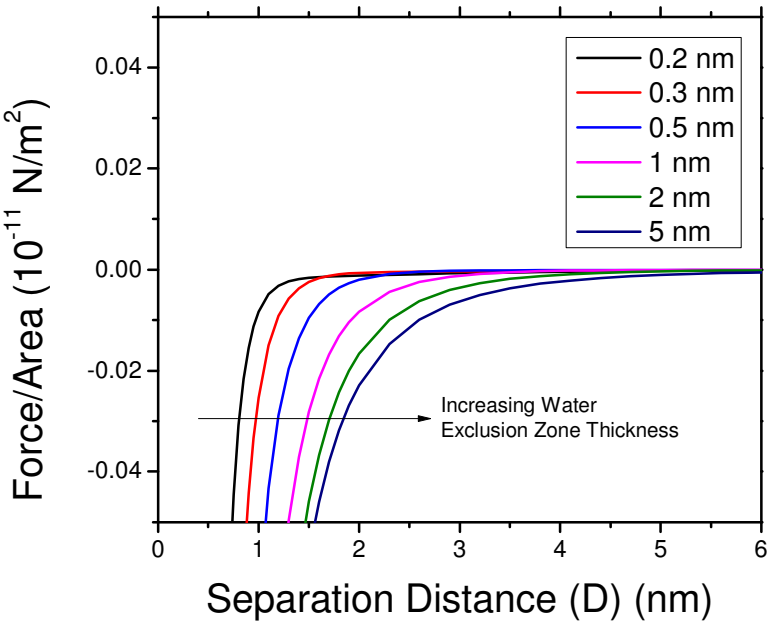

Figure 4.9 – The calculated van der Waals forces between the kaolinite silica face and the surface of the diamond-like-carbon tip when a thin layer of gas phase, the water exclusion zone, is considered at both of the surfaces.

In contrast, when the thickness of exclusion zone increases to several nanometers, which can be considered as flattened nano bubbles, the van der Waals force increases significantly and the jump-to-contact distance increases as much as 5 nm. If the thickness of the exclusion zone is considered in the calculation of the separation distance, the van der Waals interaction can be extended to above 10 nm. This attractive van der Waals force appears to contribute to what is known as the short-range hydrophobic force.

4.3.4 Molecular Dynamics Simulation at Kaolinite Basal Surfaces

A kaolinite crystal was placed in the center of a water box as the initial configuration for the molecular dynamics simulation, which is shown in Figure 4.10 (A). The water molecules interact with the silica face surface and alumina face surface of kaolinite simultaneously. After 500 ps of simulation, the energy reaches the minimum state and the system can be considered as the equilibrium state. A snapshot of the kaolinite/water interface after the equilibration is shown in Figure 4.10 (B). The yellow balls represent the silicon atoms, the green balls represent the aluminum atoms, the red balls represent the oxygen atoms, and the white balls represent the hydrogen atoms.

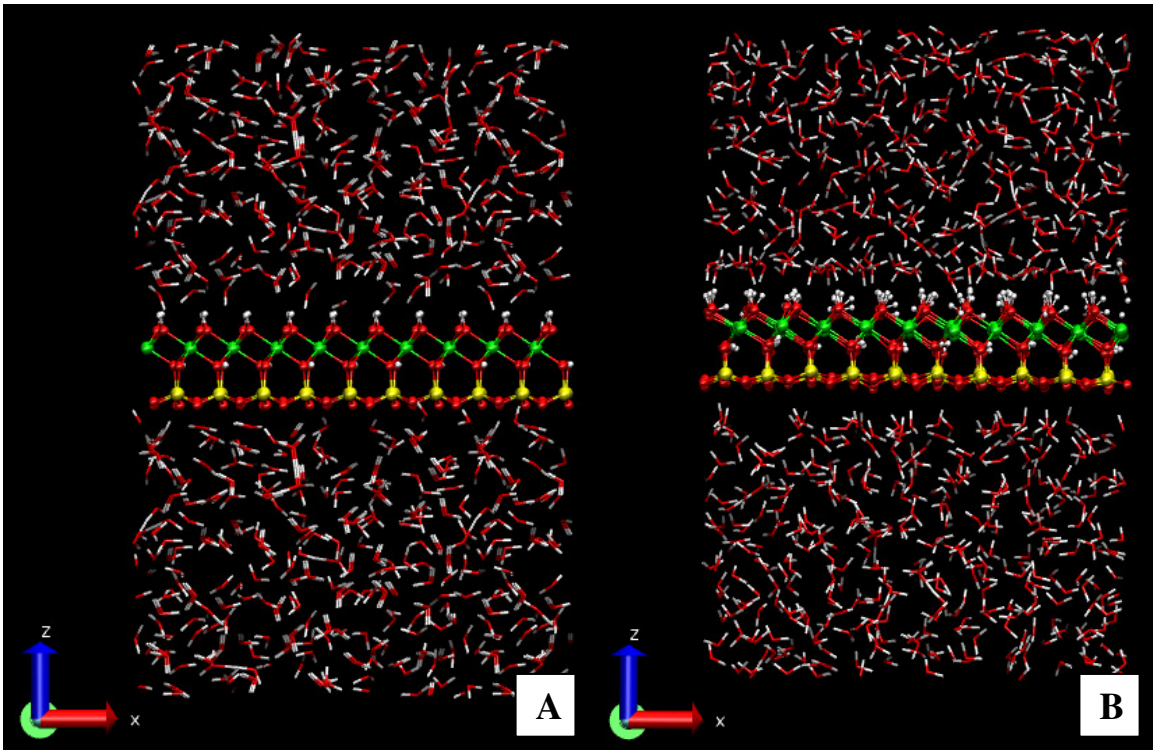

Figure 4.10 – Snapshots of the initial configuration (A) and equilibrated configuration (B) of kaolinite/water surface. Red: oxygen; Yellow: silicon; Green: aluminum; White: hydrogen.

A significant difference in the wetting characteristics for the two faces of kaolinite was found. Compare the silica face of kaolinite with the alumina face of kaolinite. It can be noted that there is gap between the water phase and kaolinite silica tetrahedral surface. This gap, also known as the “exclusion zone” or “hard wall” effect, is usually observed at hydrophobic surfaces (Mezger et al. 2006; Yu et al. 1999).The siloxane structure at the kaolinite silica tetrahedral face does not provide hydrogen bond sites, which results in a weak interaction between the surface and water molecules. This phenomenon was also observed at the surface of other phyllosilicates in previous MDS studies. For example, the basal plane of talc which has a similar crystalline structure to the kaolinite silica tetrahedral face also exhibits the water exclusion zone (Du and Miller 2007a; Wang, Kalinichev, and Kirkpatrick 2009). However, the AFM surface force measurements in this research found that the magnitude of the attractive hydrophobic force at the kaolinite silica face is lower than at the talc surface, suggesting that the hydrophobicity of the kaolinite silica tetrahedral surface is weaker than the talc basal surface. This may be due to the presence of defects or isomorphous substitution in the tetrahedral layer of the silica face. The effect of the lattice substitution on the surface hydrophobicity will be discussed in detail in Chapter 5.

In contrast to the silica tetrahedral surface (001), the water molecules are tightly bonded to the alumina octahedral basal plane surface (00$\underline{1}$), indicating the hydrophilic nature of the kaolinite alumina face. This hydrophilic characteristic was explained by the presence of surface hydroxyl groups which can provide many hydrogen bonding sites and facilitate the formation of strong hydrogen bonds (Du and Miller 2007a; Wang et al. 2005).

The water density distribution profiles along the surface normal of the kaolinite silica tetrahedral face and the alumina octahedral face are shown in Figure 4.11 (A) and (B), respectively. The zero distances represent the position of the kaolinite surfaces. At the kaolinite silica tetrahedral surface, two close packed water peaks are observed. As expected, a gap with a distance of 3 Å was found between the kaolinite silica face and the first peak of the water oxygen, suggesting the weak interaction between the water molecules and kaolinite silica face. It also can be noticed that the peak of water hydrogen in the primary water layer splits into two peaks, indicating that some of the water hydrogen atoms are closer to the kaolinite silica face. These results suggest that interaction between surface oxygen and water hydrogen is still present.

In contrast, the water molecules strongly interact with the kaolinite alumina octahedral surface, since it terminates with a layer of surface hydroxyl groups. As shown in Figure 4.11 (B), the first water hydrogen peak is in close contact with the kaolinite alumina face. Similar to the kaolinite silica face, the water hydrogen in the primary water layer tend to be oriented toward the surface. The shape of the primary water oxygen peak is more compact than the primary water oxygen peak at the kaolinite silica face. The thickness of the primary water oxygen peak at the kaolinite alumina face is 2.5 Å, whereas the thickness of the primary water oxygen peak at the silica face is 3 Å. All these results suggest that the water/alumina face interaction is stronger than the water/silica face interaction. This is attributed to the surface hydroxyl groups at the kaolinite alumina face that provide plenty of electron donor/acceptor sites and facilitate the formation of the hydrogen bonds with adjacent water molecules.

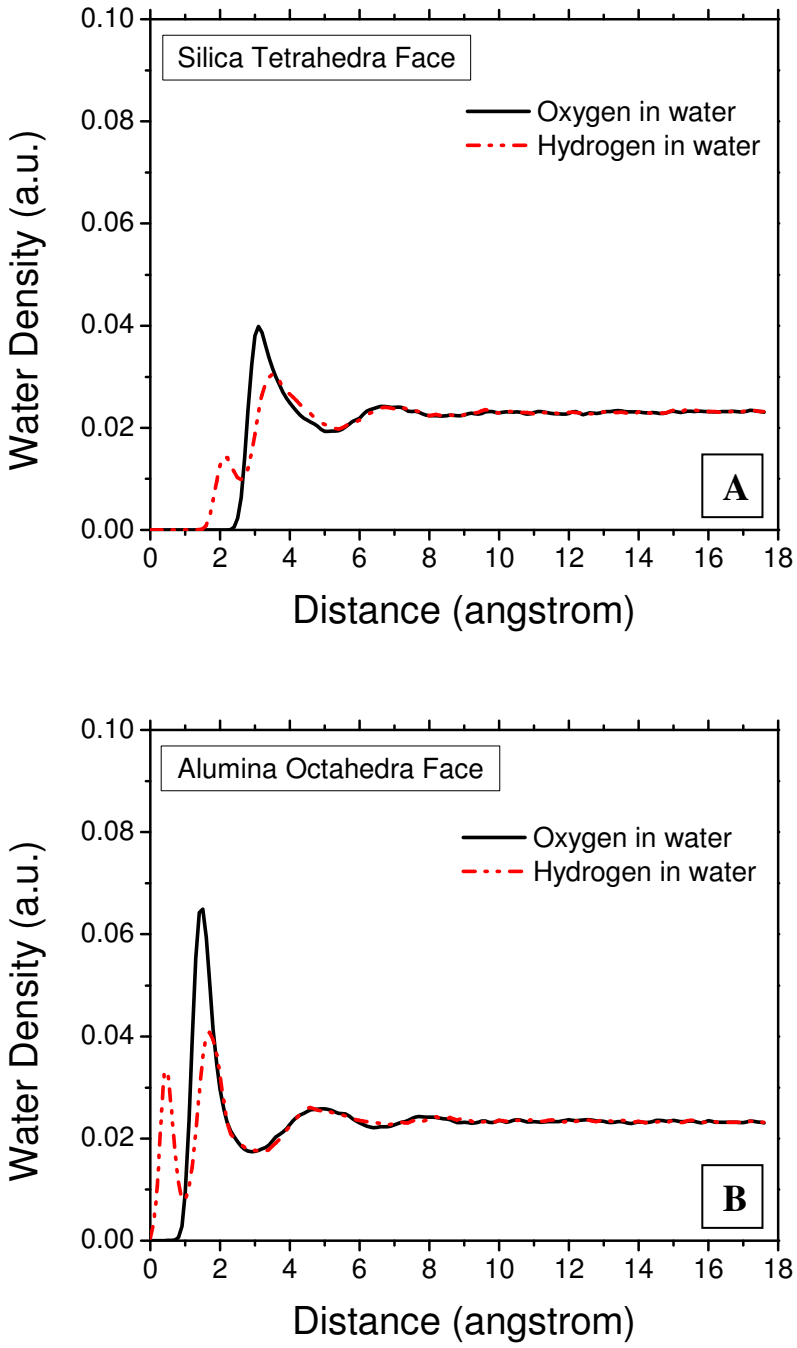

Figure 4.11 – Water density distribution at the kaolinite silica tetrahedral face surface (A) and alumina octahedral face surface (B). The zero distance represents the surface of the kaolinite crystal.

In order to further understand the interfacial water structure of the kaolinite surface, the water dipole moment distributions at the kaolinite silica tetrahedral surface and alumina octahedral surface were studied. Two critical angles were calculated to describe the orientation of water molecules. The angle α is defined as the angle between a water dipole moment and the surface normal, while β represents the relative position of hydrogen atoms with respect to the surface normal (Du and Miller 2007c).

The density distribution of angles α and β along the surface normal of the kaolinite silica tetrahedral face and alumina octahedral face are shown in Figure 4.12 and Figure 4.13, respectively, as the contour plots. As shown in Figure 4.11, the dipole orientation (angle α) for the interfacial water at the kaolinite silica face ranges from 30˚ to 130˚ with a center position at 60˚. The hydrogen position orientation (angle β) distributed more randomly, ranging from 10˚ to 90˚ and the peak center occurs at about 40˚. These results suggest that the randomness of the orientation for interfacial water molecules can be explained by the weak interaction between the water molecules and the kaolinite silica face.

At the kaolinite alumina octahedral surface, the dipole orientation (angle α) for the interfacial water is between 30˚ to 130˚ with a center position at 60˚. A sharp peak at 90˚ is found in the distribution of hydrogen position (angle β), suggesting that the direction of the hydrogen atoms is preferentially perpendicular to the surface normal. Moreover, it is observed that the intensities of two water orientation peaks for the kaolinite alumina face are higher than the silica face. These results indicate that the dipole moments of the water molecules are more oriented and most of them are facing the surface with their hydrogen atoms pointing to the surface.

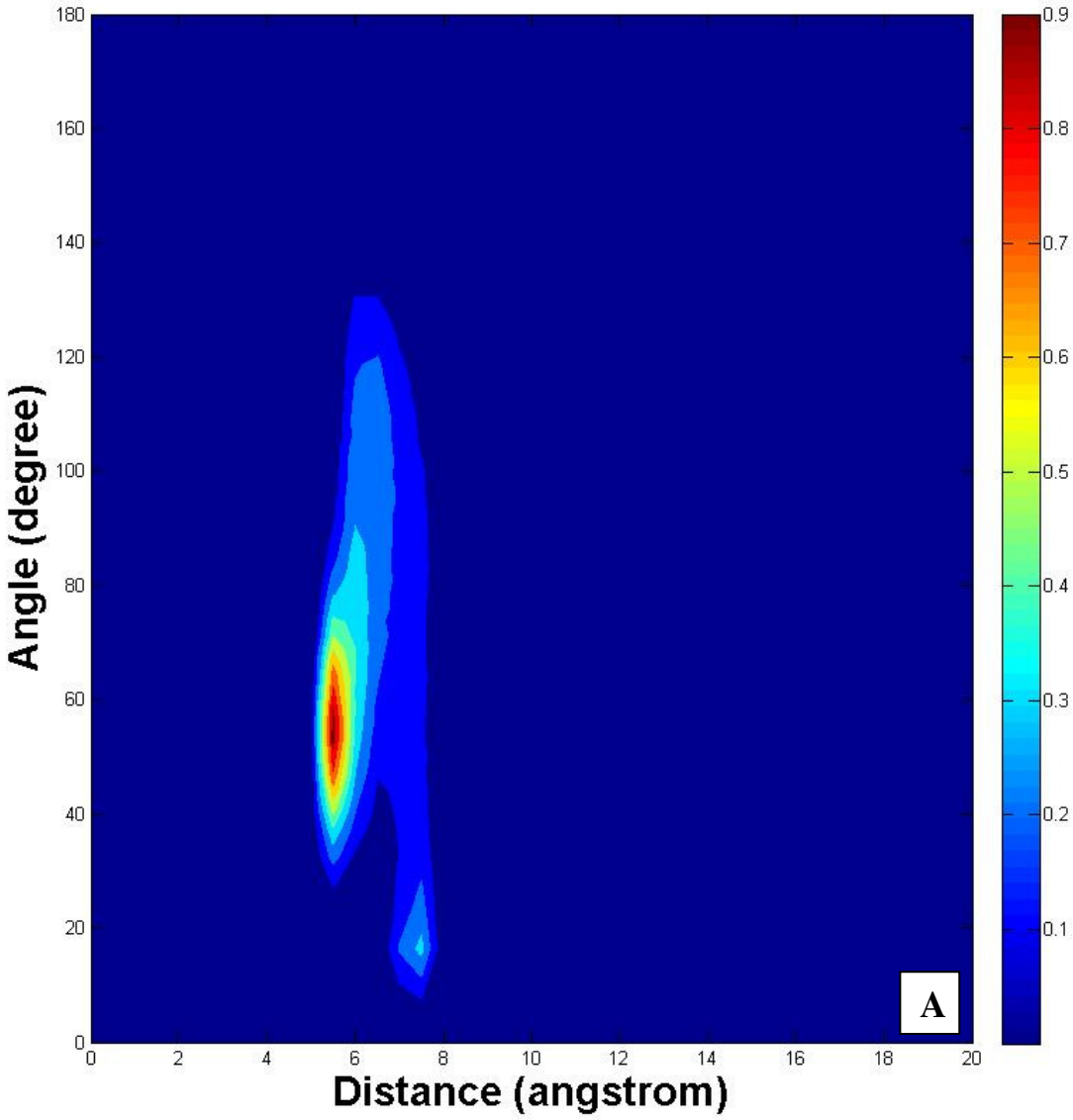

Figure 4.12 – Water dipole moment density distribution (A) and the hydrogen position density distribution (B) along the surface normal of kaolinite silica tetrahedral face surface.

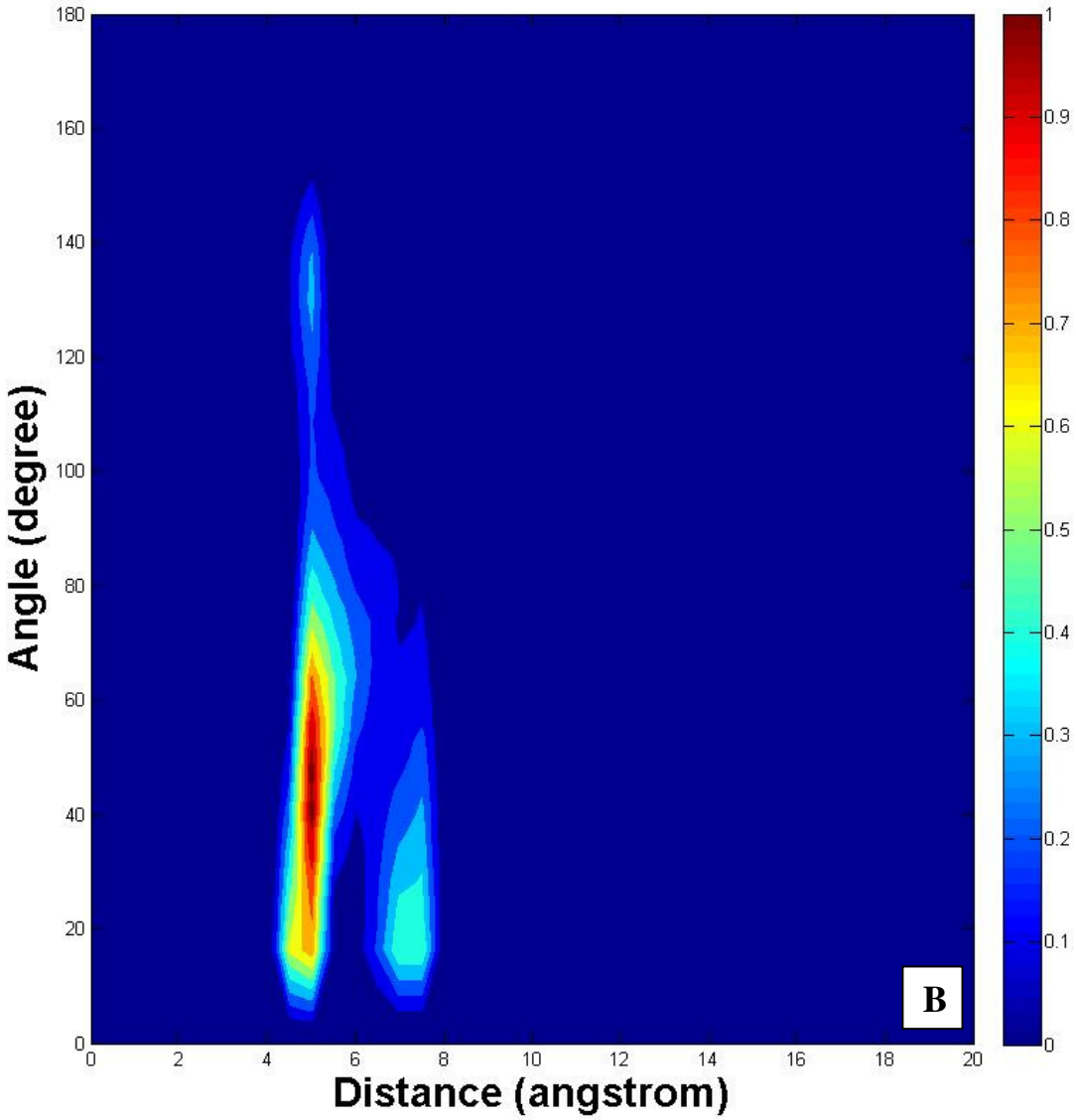

Figure 4.12 – Continued

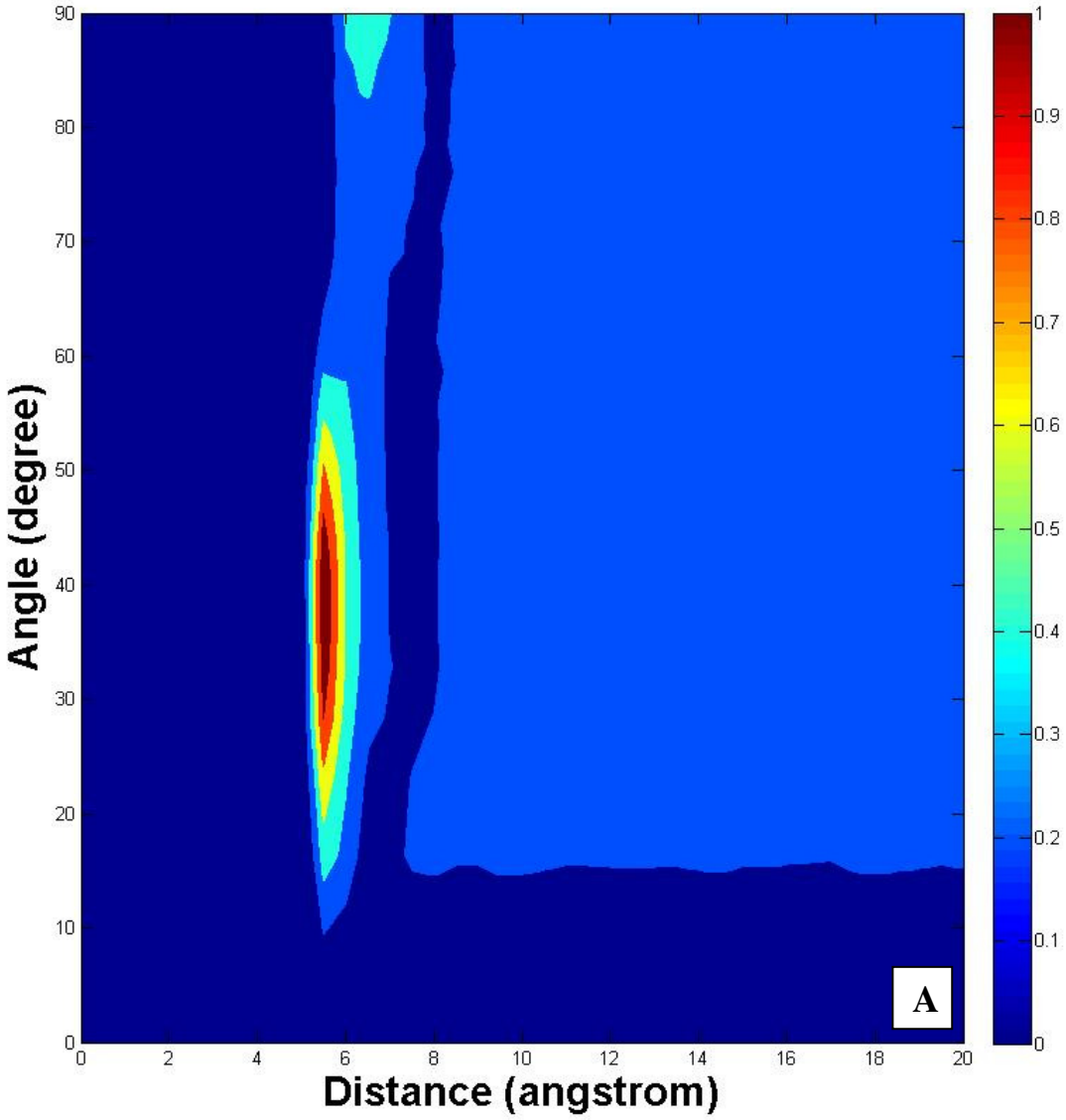

Figure 4.13 – Water dipole moment density distribution (A) and the hydrogen position density distribution (B) along the surface normal of kaolinite alumina octahedral face surface.

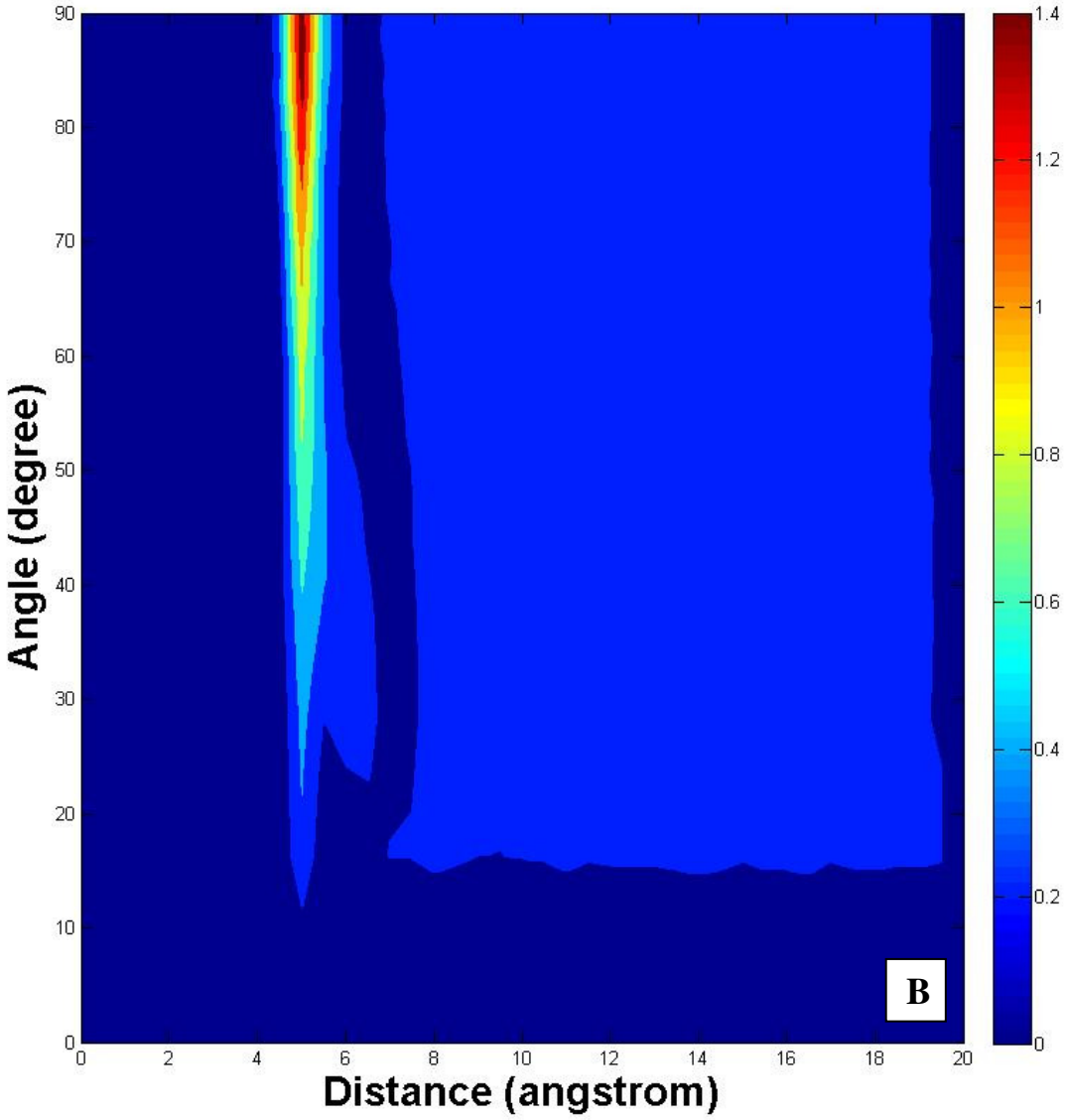

Figure 4.13 – Continued

The dynamic properties of water molecules at the kaolinite silica tetrahedral face and alumina octahedral face were also analyzed. The water residence time was calculated as a function of distance along the kaolinite surface normal. The residence time τ refers to the time for a water molecule to stay in each water layer and was calculated using the correlation function, R(t) (Berendsen, Grigera, and Straatsma 1987, Koneshan et al. 1998):

$$\tau = \int_0^\infty \langle R(t) \rangle dt \tag{4-10}$$

where R(t) is defined by:

$$R(t) = \frac{1}{N_h} \sum_{i=1}^{N_h} [\theta_i(0)\theta_i(t)] \tag{4-11}$$

where $\theta_i(t)$ is the Heaviside unit step function which has the value 1 if a water molecule is in the hydration shell at time t and zero otherwise. N_h is the hydration number.

The residence times for water molecules at the kaolinite silica surface and alumina surface were calculated along the surface normal and the results are shown in Figure 4.14. It can be noted that the residence time of interfacial water molecules at the kaolinite alumina surface is greater than the kaolinite silica surface, with magnitudes of 29.3 ps and 21.4 ps, respectively. It suggests that the water molecules are more stable at the alumina surface than at the silica surface. This is due to the stronger interaction between the water molecules and the hydroxyl groups at the kaolinite alumina surface so that a tight hydrogen bonding network can be formed.

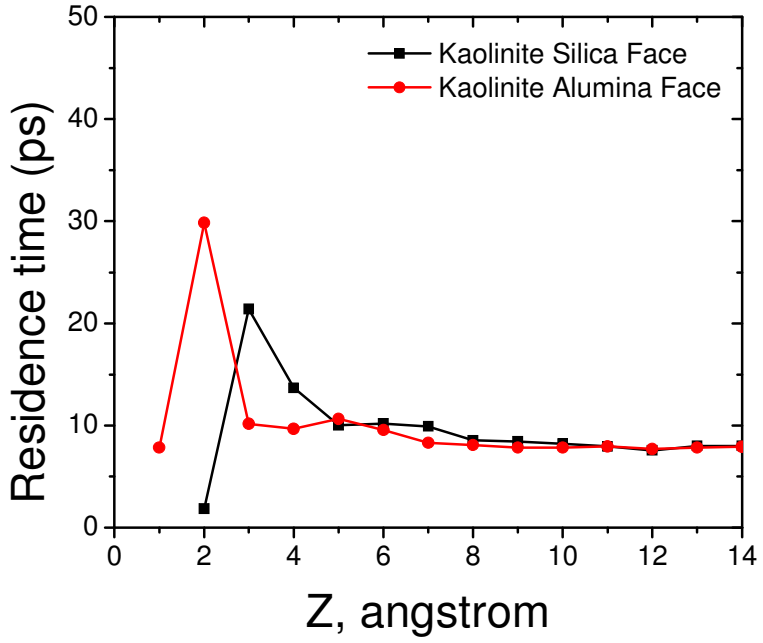

Figure 4.14 – Water residence times along the surface normal at the kaolinite silica tetrahedral and alumina octahedral basal surface. The zero distance represents the surface of the kaolinite crystal.

In contrast, at the kaolinite silica face, due to the saturated valence siloxane structure, the hydrogen bonds are difficult to form. Thus, the water molecules are more flexible at the silica tetrahedral face. In the bulk water region, with decreasing influence of surface, water molecules move faster than interfacial water molecules and their residence time is about 7.9 ps.

4.4 Summary

A new AFM-based technique was developed to describe the wetting characteristics of the two basal planes of kaolinite. The hydrophobicity was determined by the magnitude of the hydrophobic attraction force between a hydrophobic diamond-like-carbon (DLC) AFM tip and the clay mineral surfaces. The measured surface force

curves for the two basal planes of kaolinite were compared with the force curves for talc and muscovite surfaces. The results demonstrate that the kaolinite silica face has a moderate degree of hydrophobicity. Theoretical calculations of van der Waals interactions suggest that the short-range hydrophobic force detected between the DLC tip and the kaolinite silica basal surface should take into consideration the presence of the water exclusion zone at hydrophobic surfaces. In contrast, the kaolinite alumina face did not show any hydrophobic interactions with the DLC tip, suggesting its hydrophilic state. This behavior can be explained by the crystalline structure of kaolinite. The silica tetrahedral face does not offer hydrogen bonding sites, whereas the kaolinite alumina octahedral face is covered by a layer of surface hydroxyl groups, which results in a strong interaction with water molecules. Future work can investigate the effect of ionic strength, electrolyte type, and spring constant of AFM tip on the surface force curves.

The results from molecular dynamic simulation (MDS) confirmed the experimental findings. The interfacial water structure at the kaolinite silica tetrahedral face and alumina octahedral face were examined based on the analysis of water density distribution, dipole orientation distribution, and water residence time. A gap was observed between the water phase and kaolinite silica tetrahedral surface, suggesting the lack of hydrogen bonds at the kaolinite silica face. In contrast, the kaolinite alumina face is well wetted by water, since a large number of hydrogen bonds are formed between the surface hydroxyl groups and water molecules. In addition, the findings from water dipole orientation analysis and water residence time analysis also support the conclusion that the kaolinite silica tetrahedral surface has weaker interaction with the water molecules than the alumina octahedral surface.

CHAPTER 5

HYDROPHOBICITY OF THE SILICA TETRAHEDRAL FACE FOR SELECTED PHYLLOSILICATE STRUCTURES

5.1 Introduction

The silica tetrahedral sheet is a basic structural unit for all the phyllosilicates. The tetrahedral sheet is composed of silica tetrahedrons. In each tetrahedron, the silicon atom located at the center position and four oxygen atoms are tetrahedrally coordinated with the silicon atom. These tetrahedrons are connected together forming a hexagonal pattern (six member ring structure) and extending to an infinite sheet, the tetrahedral layer. Although phyllosilicates basically have the same tetrahedral layer, the surface wetting characteristics differ significantly. For example, talc is well known as a naturally hydrophobic mineral, whereas muscovite is a naturally hydrophilic mineral. They are both 2:1 phyllosilicates in which an octahedral sheet is sandwiched between two silica tetrahedral sheets.

However, in the muscovite, one quarter of the silicon atoms in the silica tetrahedral face are replaced by the aluminum atoms. This replacement is known as isomorphous substitution. In contrast, talc has no isomorphous substitution. Thus, it can be expected that the degree of isomorphous lattice substitution, especially in the silica tetrahedral face, can be a critical factor which can explain the difference in wetting

characteristics. In this chapter, we utilized the molecular dynamics simulation (MDS) method to study the effect of isomorphous substitution on the interfacial water structure as well as the water contact angle of the silica surface of phyllosilicates.

The wettability of phyllosilicates has been studied by many researchers using different experimental techniques. Contact angle measurement is one of the most prevailing techniques. The water contact angle results for selected phyllosilicates are summarized in Table 2.2, Chapter 2. However, due to the sample shape, surface preparation, sample pretreatment, and experimental procedures, it is difficult to systematically compare the surface hydrophobicity using contact angle measurements.

In recent years, as a powerful computational method, molecular dynamics simulation has provided an opportunity to elucidate the surface/water interactions and the origin of surface hydrophobicity. Wang et al. studied both water/talc and water/mica interfaces which can be considered as hydrophobic and hydrophilic surfaces (Wang, Kalinichev, and Kirkpatrick 2009). They demonstrated that the substrate structure and composition significantly influence the interfacial water behavior. Although some efforts have been made, the effect of isomorphous lattice substitution on the interfacial water structure is still not fully understood. In this regard, the surface/water interactions at three alumino-phyllosilicates, including pyrophyllite, illite, and muscovite, were studied having levels of isomorphous substitution of about 0%, 15%, and 25% (see Table 5.1).

Pyrophyllite, illite, and muscovite are three types of trilayer phyllosilicates. See Figure 5.1. The general information, including chemical formula, crystal symmetry, and density, are shown in Table 5.1.

Table 5.1 – General information about pyrophyllite, illite, and muscovite.

Minerals	Chemical Formula	Crystal Symmetry	Density	% of IS
Pyrophyllite	$Al_2Si_4O_{10}(OH)_2$	Monoclinic/Triclinic	2.65-2.9	~0%
Illite	$K_yAl_4(Si_{8-y},Al_y)O_{20}(OH)_4$, (usually with $1<y<1.5$, but always with $y<2$)	Monoclinic	2.6-2.9	12.5 ~18.5%
Muscovite	$KAl_2(AlSi_3O_{10})(F,OH)_2$	Monoclinic	2.76-3	25%

Pyrophyllite has a TOT (tetrahedral-octahedral-tetrahedral) trilayer structure with a gibbsite sheet sandwiched between the two silica tetrahedral sheets. This structure is similar to talc. The only difference is that talc has a brucite sheet as the octahedral layer. The gibbsite sheet in pyrophyllite has a positive charge to compensate the surface charge from the two silica tetrahedral sheets. These repeating trilayers are held together by van der Waals forces and each of the trilayer structures is electrically neutral. There is almost no substitution of silicon by aluminum or magnesium in the silica tetrahedral sheet. The low substitution and low polarity provide pyrophyllite with a natural hydrophobicity.

Illite and muscovite are in the mica group also with a TOT trilayer structure. Varying degrees of lattice substitution occur predominantly in the tetrahedral sheet where Si^{4+} can be substituted by Al^{3+}. Usually, the counter ions which compensate the net negative lattice charge are potassium ions. These potassium ions are fixed and the ion exchange capacity is low. Illite and muscovite have a similar crystalline structure, but differ from each other by the degree of lattice substitution. One quarter of the silicon atoms in the tetrahedral sheet of muscovite are substituted by aluminum, while illite has less lattice substitution than muscovite (van Olphen 1963).

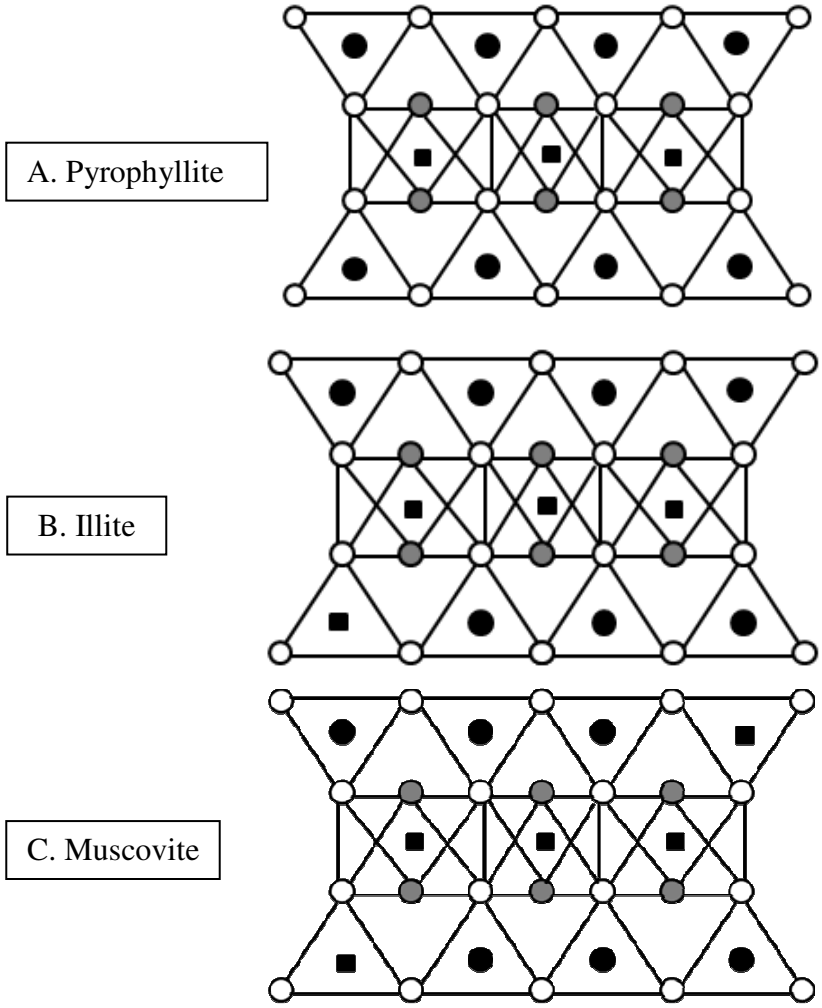

Figure 5.1 – Crystalline structure of (A) pyrophyllite, (B) illite and (C) Muscovite. Empty circles represent oxygen atoms, black circles represent silicon atoms, grey circles represent hydroxyls and the squares represent aluminum atoms.

A common assumption is that when illite or muscovite is cleaved, the surface carries a constant negative charge, with the magnitude depending on the degree of substitution. Due to this charge imbalance and the nature of ionic interlayer forces, illite and muscovite are usually considered to be hydrophilic (Miller et al. 2011). The comparison of the amount of isomorphous substitution (IS) is listed in Table 5.1. The crystalline structure of pyrophyllite, illite, and muscovite are shown in Figure 5.1.

5.2 Simulation Details

The MD simulation program, Amber 9, was utilized to study the interfacial water structure at the surface of the trilayer phyllosilicates surfaces (Case et al. 2005). The initial configurations of the pyrophyllite and muscovite surfaces were created according to the lattice parameters provided by the American Mineralogist Crystal Structure Database. The simple point charge (SPC) water model (Berendsen 1981), together with the CLAYFF force field (Cygan, Liang, and Kalinichev 2004) which was used to describe the water interactions and the intermolecular potential parameters are listed in Table 5.2.

Table 5.2 – Potential parameters for phyllosilicate minerals.

Species	Charge [e]	ε [Kcal/mol]	σ [A]	References
Silicon	2.1	1.33×10^{-6}	3.706	(Cygan, Liang, and Kalinichev 2004)
Bridging oxygen	-1.05	0.1554	3.165	(Cygan, Liang, and Kalinichev 2004)
Surface oxygen	-0.95	0.1554	3.165	(Cygan, Liang, and Kalinichev 2004)
Aluminum	1.575	1.84×10^{-6}	4.794	(Cygan, Liang, and Kalinichev 2004)
Potassium ion	1	0.1	3.25	(Du and Miller 2007c, Koneshan et al. 1998)
Water hydrogen	0.41	0	0	(H. J. C. Berendsen 1981)
Water oxygen	-0.82	0.1554	3.169	(H. J. C. Berendsen 1981)

The pair potential force field used in the simulations is given as a combination of the Lennard-Jones and the Coulomb electrostatic interactions, and can be expressed as:

$$U_{pair} = \sum_i \sum_j \left(4\varepsilon \left[\left(\frac{\sigma_{ij}}{r_{ij}} \right)^{12} - \left(\frac{\sigma_{ij}}{r_{ij}} \right)^{6} \right] + \frac{q_i q_j}{r_{ij}} \right) \tag{5-1}$$

where ε is the energy parameter, σ is the size parameter, q is the charge, and r is the distance between species i and j. Lorentz-Berthelot mixing rules were applied to calculate the potential parameters of pairs:

$$\varepsilon_{ij} = \sqrt{\varepsilon_i \varepsilon_j} \tag{5-2}$$

$$\sigma_{ij} = \frac{\sigma_i + \sigma_j}{2} \tag{5-3}$$

The surfaces with 5% and 15% isomorphous substitution were created by adjusting the ratio of aluminum and silicon atoms based on the muscovite surface. Two sections are included in this study, the calculation of contact angle and the analysis of interfacial water structure. Simple cubic cells (80 × 80 × 80 Å) containing the phyllosilicate surfaces and 500 water molecules were constructed with periodic boundary conditions to simulate the water contact angle. The simulation was initiated with the water molecules as a spherical shaped droplet placed on the silica surface. The drop then spread to an equilibration contact angle and the contact angle was then measured based on a two-dimensional water density distribution map. For the study of the interfacial

water structure, simple cubic cells (26 × 28 × 40 Å) containing the phyllosilicates surfaces and 700 water molecules were created.

Following the procedure reported in the literature (Du and Miller 2007b; Kirkpatrick, Kalinichev, and Wang 2005; Wang et al. 2010), the phyllosilicates surfaces with 0%, 5%, 15%, and 25% isomorphous substitution in the silica tetrahedral face were simulated as a NPT assembly with the pressure fixed at 0.1 Mpa and the temperature fixed at 298 K for 100 ps. Then a pre-equilibrated water box with 700 water molecules was introduced into the system to analyze the interfacial water structure. For the study of contact angle, a pre-equilibrated water droplet was placed on the top of the surface. After adding the water molecules, the simulations were performed in periodic cells under NVT assembly using Hoover's thermostat (Melchionna, Ciccotti, and Holian 1993). The Ewald sum has been used to account for the electrostatic interactions. The Leapfrog method with a time step of 1 fs was used to integrate the particle motion. A total simulation time of 1.2 ns including an equilibrium time of 200 ps was applied. The results were analyzed based on the last 1 ns of the simulation.

5.3 Results and Discussions

5.3.1 Effect of Isomorphous Substitution on the Water Contact Angle

Contact angle is a term which is used to describe the surface wettability. It is defined as the angle between the liquid/vapor interface and the solid/vapor interface measured at the three phases of contact. The contact angle for a solid surface is determined by the nature of the material (surface free energy, polarity, crystalline structure, etc.), sample features (shape, porosity, surface roughness, etc.) and the environmental factors (temperature, humidity, etc.).

In this study, the molecular dynamics simulation method was used to study the effect of the extent of isomorphous lattice substitutions in the silica tetrahedral face on the wettability. A droplet was placed on the top of the silica tetrahedral surface of the trilayer phyllosilicate with different amounts of isomorphous substitutions. As examples, snapshots of the initial configuration and after equilibration of the water droplet at the pyrophyllite and muscovite surfaces are shown in Figure 5.2. The simulations were first carried out for 200 ps in order to equilibrate the systems and then continued for 1 ns. Based on the simulation results during the last 1 ns, two-dimensional water density distribution maps were constructed from the x-z plane.

Figure 5.3 presents the color visualization of the two-dimensional water density distribution maps at the silica tetrahedral surfaces with different isomorphous substitutions. The red color refers to a high water density, whereas the blue color refers to a low water density. It can be noted that at the pyrophyllite surface, the water molecules cannot spread over the surface and the water droplet keeps the round shape with a contact angle of about 70˚. The water density along the surface normal is not uniform. Two layers of close compact water molecules followed by the bulk water were observed at the pyrophyllite surface. When the silica tetrahedral surface of pyrophyllite contains 5% isomorphous substitution of Al^{3+} for Si^{4+}, the shape of the water droplet changes significantly. As shown in Figure 5.3 (B), the water contact angle at the silica tetrahedral surface with 5% of isomorphous substitution is found to be about 30˚. This sharp decrease of contact angle results from the increase surface polarity which is due to the surface charge imbalance and the presence of interlayer potassium ions. In this regard, the water droplet has a greater tendency to spread over the surface.

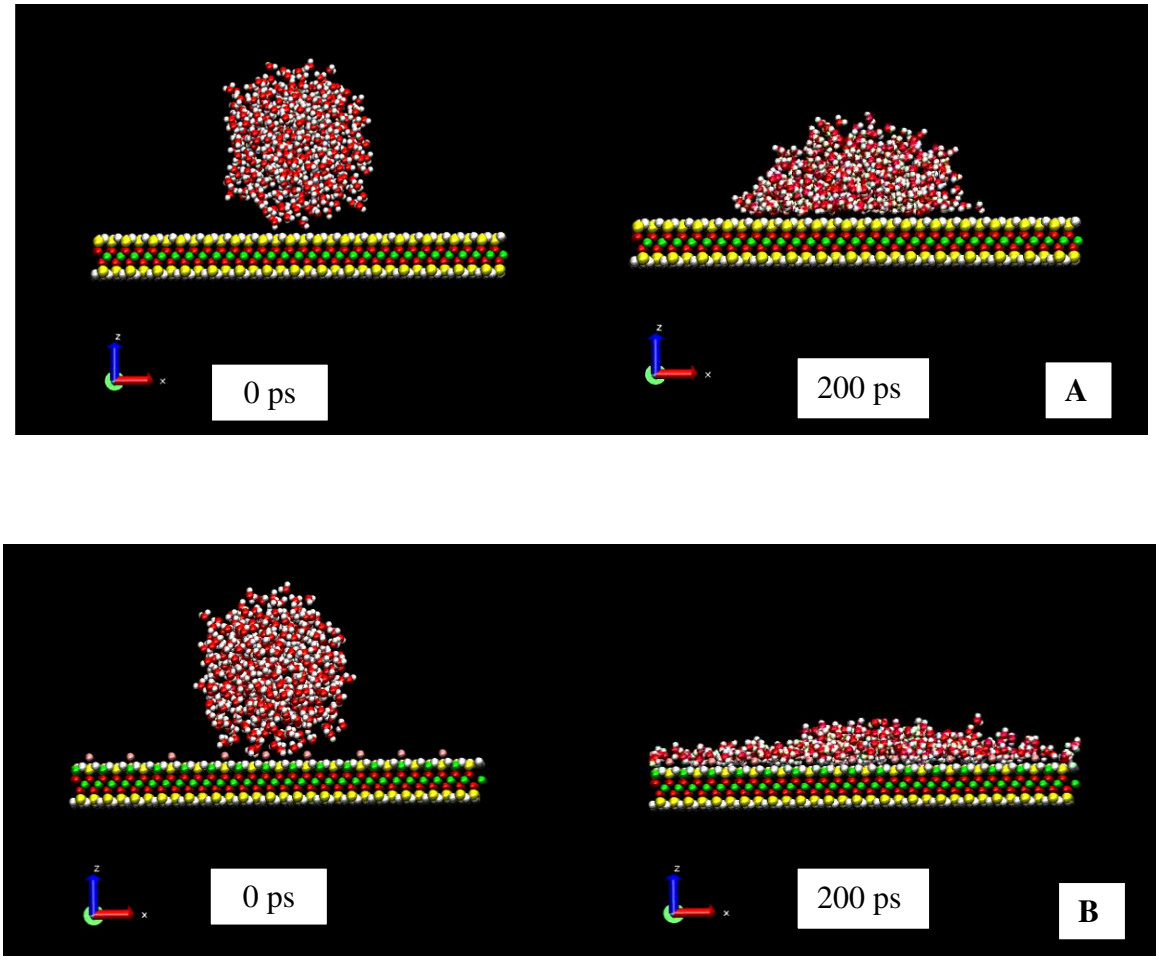

Figure 5.2 – Snapshot of the initial configuration and the configuration after 200 ps for droplet/pyrophyllite simulation (A) and droplet/muscovite simulation (B).

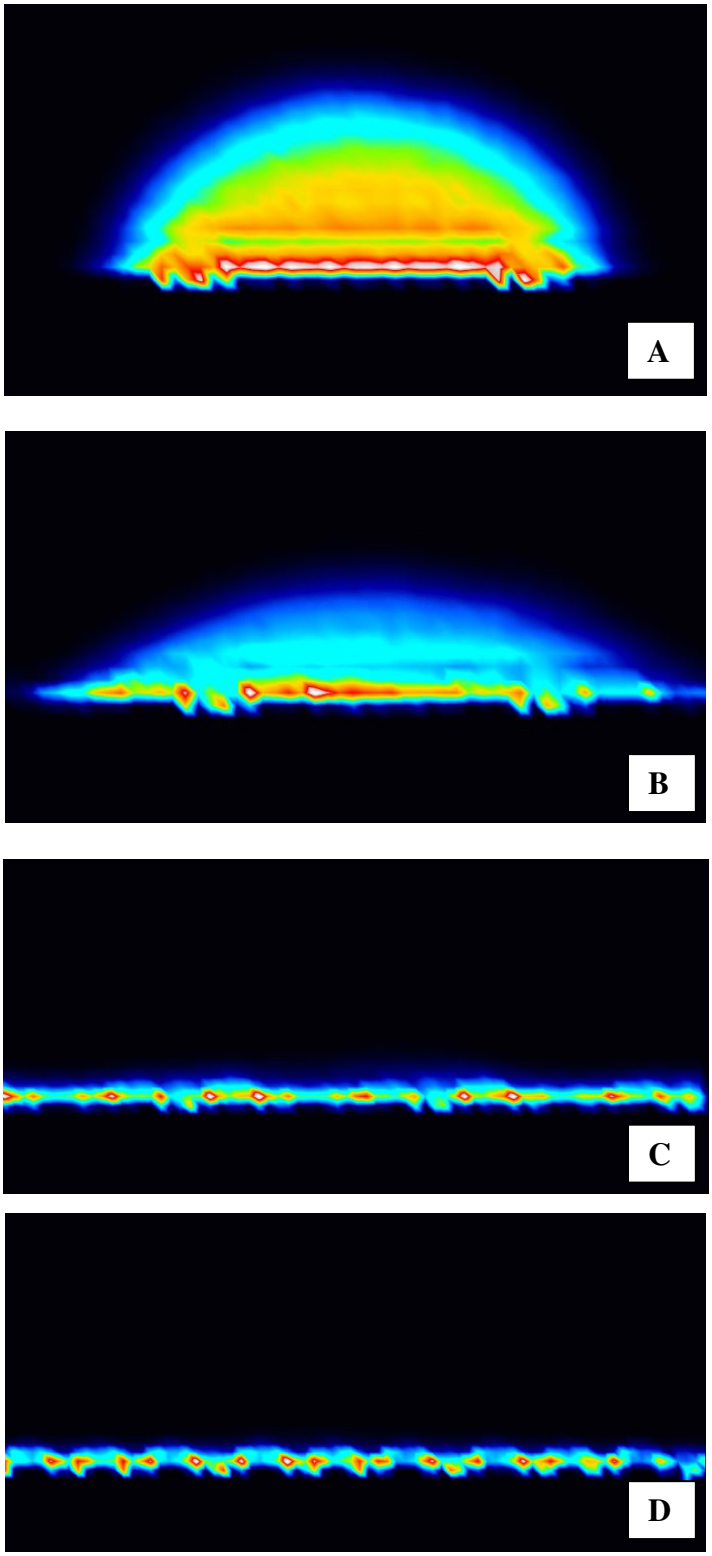

Figure 5.3 – Visualization of the two-dimensional water density analysis for a water droplet at the silica tetrahedral surface of pyrophyllite (A), 5% isomorphous substitution (B), illite (C), and muscovite (D).

At the illite surface which has about 15% of isomorphous substitution, the surface is completely wetted by the water droplet after equilibration. The contact angle is determined to be 0˚. This finding is in good agreement with the experimental findings that illite is a natural hydrophilic mineral. In addition, it can be noticed that the distribution of water molecules at the illite surface is not homogeneous and some water molecules are more likely to surround the potassium ions. This is attributed to the hydration of potassium ions which results in a strong interaction between potassium ions and water molecules. As expected, similar behavior was found at the hydrophilic muscovite surface, as shown in Figure 5.3 (D).

Based on this contact angle analysis from MDS results, the effect of isomorphous substitution in the silica tetrahedral layer on the wetting characteristics of the silica surface can be estimated. The measured contact angle as a function of the percentage of isomorphous substitution is shown in Figure 5.4.

The results indicate that the presence of isomorphous lattice substitution significantly influences the surface wettability. The contact angle decreases rapidly with only 10% lattice substitution. This simulation result may explain the finding from AFM that the talc silica surface has a greater hydrophobicity than the kaolinite silica surface. Previous studies have reported that natural kaolinite has various defects, including Mg, Ca, and Fe with concentrations of less than 1% (Frost et al. 2004; Wang and Chen 2004). The elemental composition of the kaolinite sample used in this research is 7.98% aluminum, 7.95% silicon, 0.35% potassium, 0.15% calcium, and 0.08% iron. The percentage of isomorphous substitution is calculated from the ratio of the number of substitutions and the number of silicon atoms in the perfect lattice arrangement.

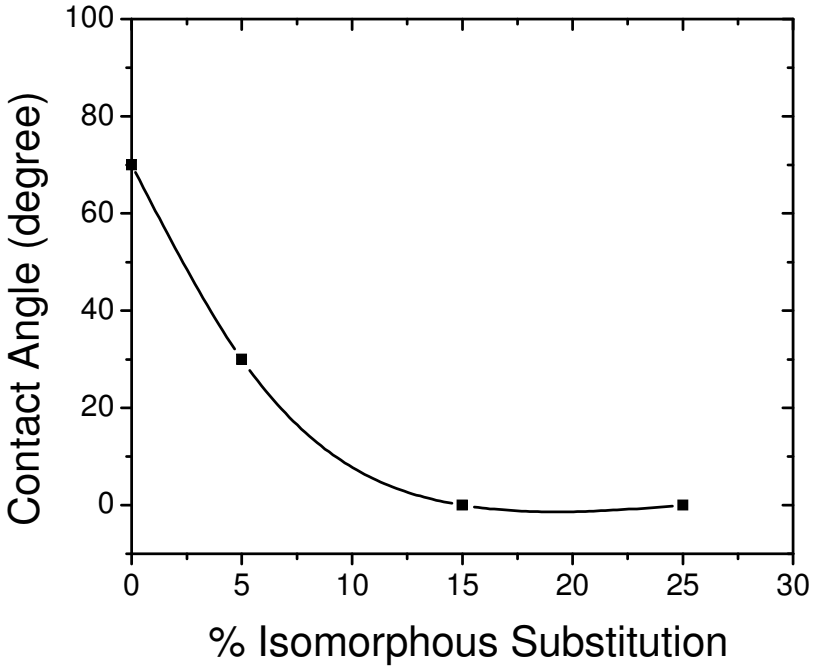

Figure 5.4 – Water contact angle as a function of the percentage of isomorphous substitution in the silica tetrahedral surface of phyllosilicate.

Therefore, if the calcium, iron, and aluminum substitute into the silica tetrahedral face, the calculated percentage of isomorphous substitution for the kaolinite sample used in this research is approximately 3.2%. According to Figure 5.4, the contact angle of kaolinite should be around 40˚. This value is slightly lower than the value predicted from the fitting of hydrophobic force data (~60˚). See Table 4.4. However, it should be noted that these trace amounts of calcium, iron, and aluminum may be present as impurities instead of substitutions. It is also possible that these elements substituted into the octahedral sheet. Therefore, in the real situation, the percentage of substitution may be less than 3.2% and the predicted contact angle may be higher than 40˚. Also, the error from the elemental analysis or the error in the AFM surface force measurements may also be the reason for the difference between the measured and predicted contact angles.

5.3.2 Effect of Isomorphous Substitution on the Interfacial Water Structure

The effect of isomorphous substitution on the interfacial water structure of the phyllosilicate silica tetrahedral surface was investigated using molecular dynamics simulation. Figure 5.5 and Figure 5.6 show the water density distribution profiles along the surface normal of the silica tetrahedral surfaces with 0% (pyrophyllite), 5%, 15% (illite), and 25% (muscovite) of silicon atoms substituted by aluminum. Since the surfaces with lattice substitution have a deficiency of surface charge, potassium ions were placed at the surfaces as the interlayer cations to compensate the surface charge. The position of the potassium ions are marked on the graphs by the symbol K.

At the hydrophobic pyrophyllite silica tetrahedral surface, as expected, a gap with a distance about 3Å was observed between the water phase and the pyrophyllite surface. As shown in Figure 5.5 (A), the first water hydrogen peak is closer to the surface than the first water oxygen peak, indicating that some of the water hydrogen atoms tend to point toward the surface. When there is 5% isomorphous substitution in the silica tetrahedral surface, it can be noted that the primary water layer is close and adjacent to the surface potassium ions. In addition, a small number of water molecules penetrate through the potassium ions. These phenomena are due to the hydration of the potassium ions as well as the charge effect caused by the lattice substitutions. When the percentage of isomorphous substitution is increased to 15% and 25%, more water molecules penetrate through the potassium ions and stay between the potassium ions and surface oxygen atoms. Moreover, the number of water molecules in the primary hydration layer increases significantly, indicating the stronger interaction between water molecules and silica tetrahedral surfaces with presence of isomorphous substitutions.

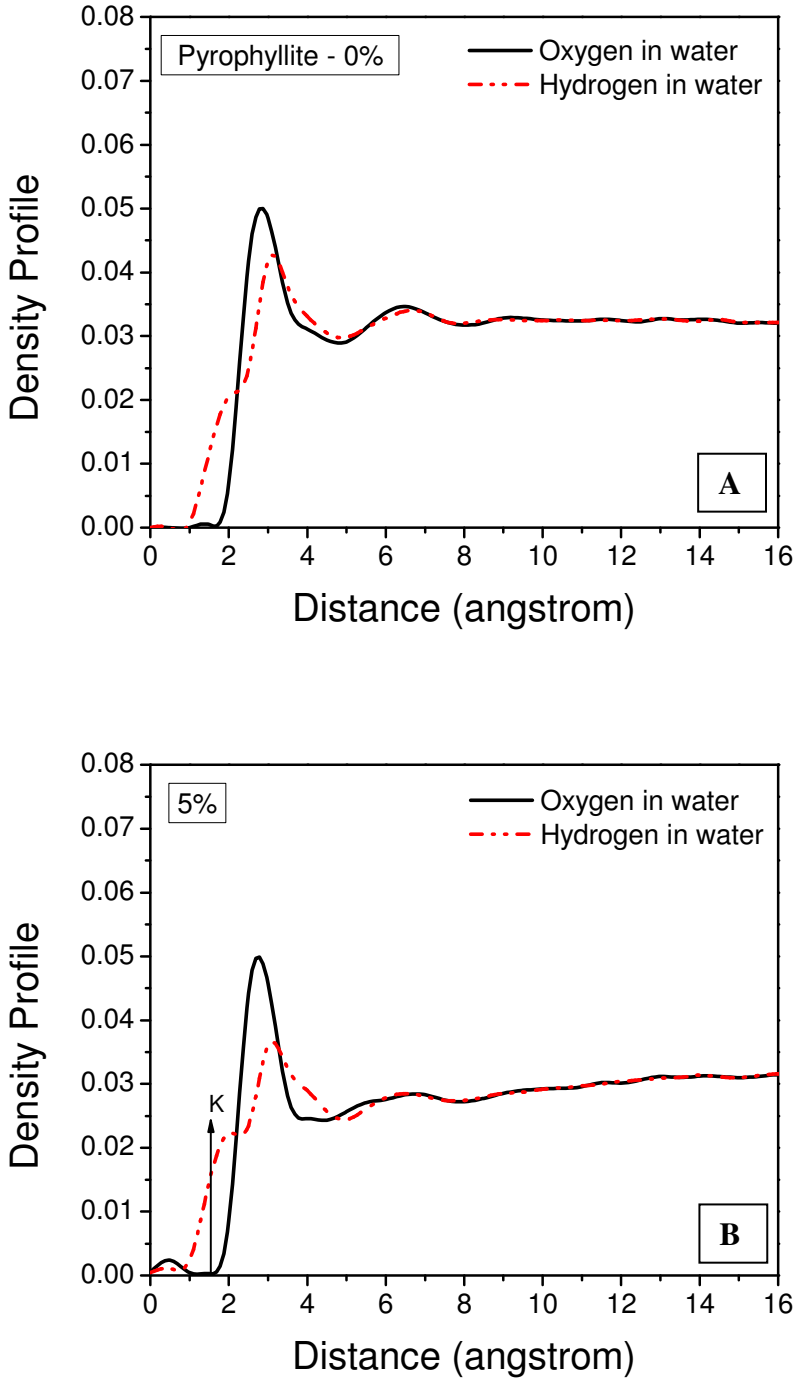

Figure 5.5 – Water density distribution at the silica tetrahedral surface of pyrophyllite (A) and 5% isomorphous substitution (B). The zero position refers to the position of surface oxygen atoms. The position of interlayer potassium ions is marked on the graph by the symbol K.

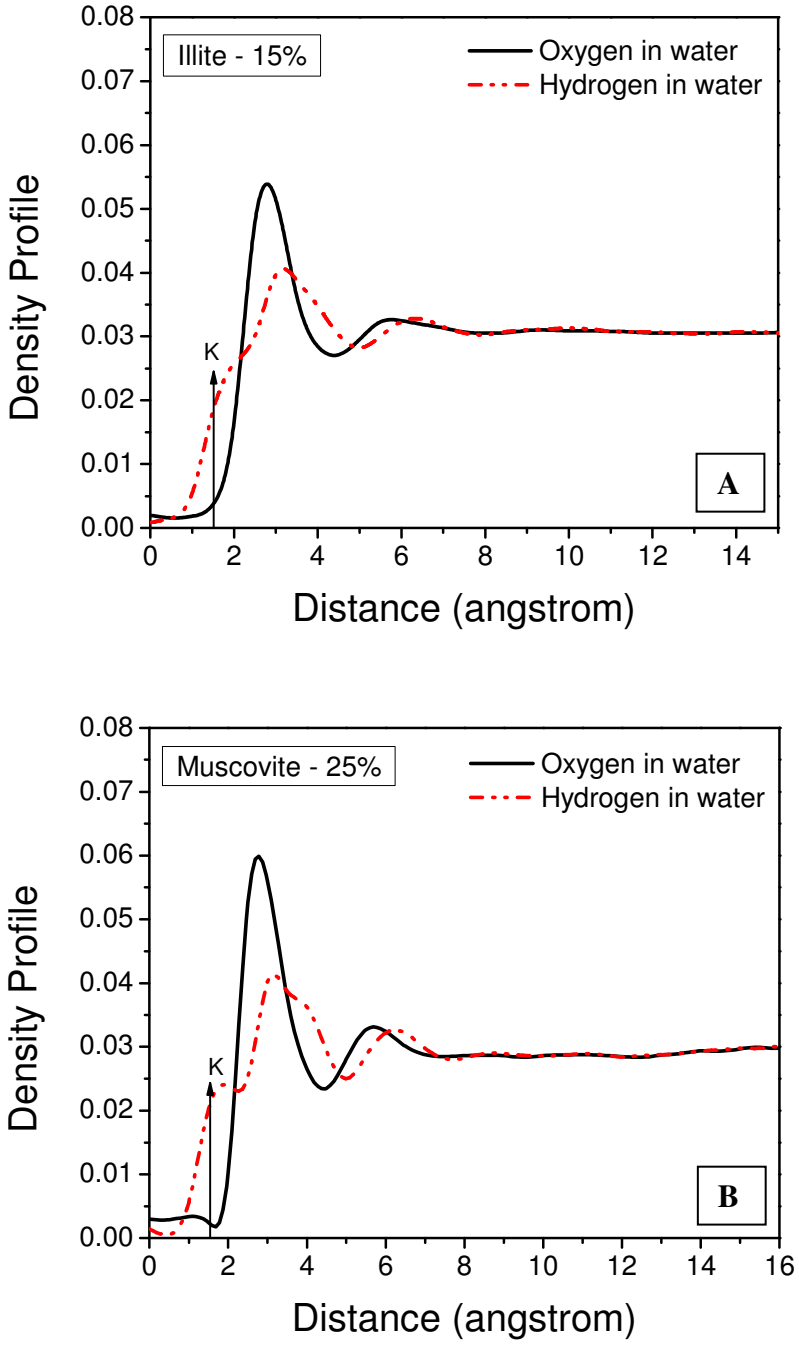

Figure 5.6 – Water density distribution at the silica tetrahedral surface of illite (A) and muscovite (B). The zero position refers to the position of surface oxygen atoms. The position of interlayer potassium ions is marked on the graph by the symbol K.

In order to have a better understanding about the effect of lattice substitutions on the interfacial water structure, the water residence times at the phyllosilicate silica tetrahedral surfaces with different extents of isomorphous substitutions were calculated along the surface normal.

As shown in Figure 5.7, due to the presence of the water exclusion zone at the pyrophyllite surface, the water molecules cannot get close to the surface; therefore, the peak of residence time for the primary water layer is located at 3Å from the pyrophyllite surface. At the silica tetrahedral surface with 5% of isomorphous substitutions, the shape of the water residence time profile changes significantly. Due to the penetration of the water molecules, in addition to the peak at 3 Å, another peak is present at 1.5 Å which is close to the position of interlayer potassium ions. It is also noted that the magnitude of the peak at 1.5 Å is greater than the peak at 3 Å, suggesting that the water molecules are likely to stay longer surrounding the potassium ions, which is attributed to the strong interaction between potassium and water molecules.

When the isomorphous substitutions in the silica tetrahedral surface increases to 15%, the peak of the water residence time at 3 Å disappears, suggesting that the water molecules at this layer move fast and behave similar to bulk water. In contrast, the water molecules tend to be immobilized at the distance of 1.5 Å from the surface. These results indicate that the interfacial water molecules are dominated by the interaction between the water molecules and potassium ions/aluminum substitutions. The water residence time profile at the muscovite surface (25% ismorphous substitutions) is similar to the illite surface (15% ismorphous substitutions). The magnitude of the peak at 1.5 Å for the muscovite surface is slightly greater than for the illite surface.

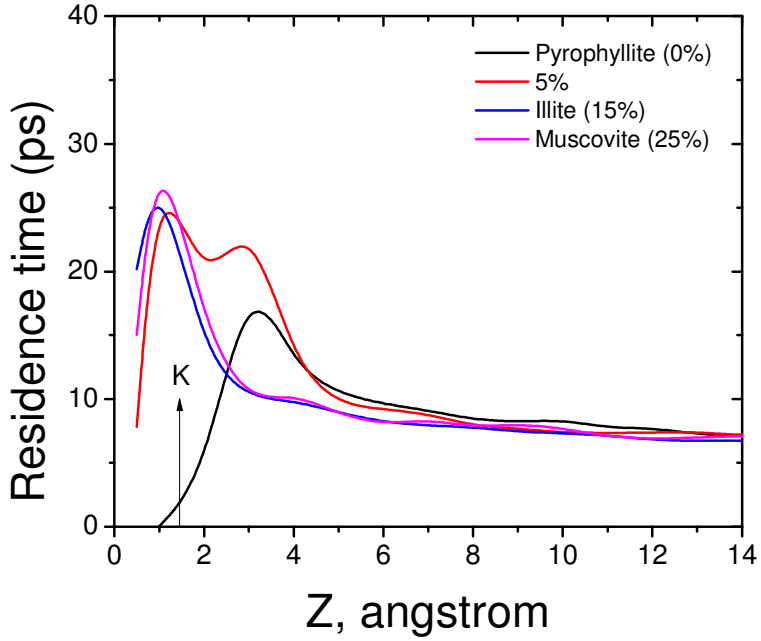

Figure 5.7 – Water residence time along the surface normal of the phyllosilicate silica tetrahedral basal surfaces with different degrees of isomorphous substitution. The zero position represents the position of surface oxygen atoms.

5.4 Summary

The effects of isomorphous lattice substitution on the hydrophobicity and the interfacial water structure of the phyllosilicate silica tetrahedral basal surfaces were studied using molecular dynamics simulation. The silica tetrahedral surfaces of 0% (pyrophyllite), 5%, 15% (illite), and 25% (muscovite) isomorphous substitutions were created and water droplets were placed on these surfaces. The contact angles were measured based on the two-dimensional water density distribution map. Results show that in the case of pyrophyllite, the water molecules cannot spread over the surface and the contact angle was measured as about 70˚. When there is 5% isomorphous substitution present in the silica tetrahedral surface, the water contact angle decreases to 30˚ due to the increase in surface polarity and the presence of interlayer potassium ions. At the illite

surface which has about 15% isomorphous substitution, the surface is completely wetted by the water droplet after equilibration and the contact angle is 0˚. Based on this MDS study, the relationship between the percentage of isomorphous substitution and water contact angle was established and the water contact angle of the kaolinite silica face was predicted. It should be noted that the phyllosilicate crystals constructed in the MDS study as well as the water droplet size are nanometer in scale. In this regard, the MDS results may not be completely consistent with the experimental water contact angle results.

The interfacial water structures at the phyllosilicate silica tetrahedral surfaces with different extents of isomorphous substitution have been studied. The water density distribution profiles suggest that when isomorphous substitutions occur, the water molecules can penetrate through the interlayer potassium ions, resulting in a more hydrophilic surface state. Moreover, with an increasing amount of isomorphous substitution, the number of water molecules in the primary hydration layer increases significantly, which is owing to the strong interaction between the potassium ions/aluminum substitutions and the water molecules. The results from water residence time analysis show that water molecules at the silica tetrahedral surface with isomorphous substitution are immobilized closer to the surface when compared with the water molecules at the surface without substitutions, which is due to the strong hydration of the interlayer cations. From the findings of this study, it can be concluded that the isomorphous substitutions in the silica tetrahedral surface significantly influence the hydrophobicity as well as the interfacial water structure. The decrease in water contact angle appears to arise from the surface charge imbalance and the presence of the interlayer cations.

CHAPTER 6

SURFACE CHARGE ANALYSIS OF CHLORITE SURFACES

6.1 Introduction

The chlorite group of minerals is a major group of magnesia silicate gangue minerals found in both sulfide and nonsulfide ores. Previous research from the literature reports that fine chlorite particles can contaminate sulfide concentrates, such as pentlandite, which reduces the grade of the concentrate and increases the slag melting point (Fornasiero and Ralston 2005; Pietrobon et al. 1997). Therefore, the depression of chlorite mineral particles is very important in order to achieve acceptable separation efficiencies in certain flotation systems.

The principle mechanism that may explain the enrichment of chlorite in the concentrate is slime coating, in which these fine chlorite particles are likely to attach to the valuable sulfide minerals and thus report to the flotation concentrate. The surface charge is believed to be the main factor that influences the slime coating, since it controls the interaction between the valuable sulfide minerals and slime particles (Bremmell, Fornasiero, and Ralston 2005; Edwards, Kipkie, and Agar 1980; Fornasiero and Ralston 2005; Pietrobon et al. 1997). In this regard, a better fundamental understanding of the surface charging properties of chlorite should help in the design of improved flotation separations. Moreover, the adsorption of flotation reagents at mineral surfaces is also

significantly affected by their surface charging. Due to the small particle size and low specific gravity, the chlorite particles may flow with water and be convectively transported to the froth phase during flotation, a phenomenon which is called entrainment. Poor liberation of chlorite from the valuable minerals may also cause an increased amount of chlorite in the concentrate. Finally, Fornasiero et al. reported that Cu^{2+} and Ni^{2+} can activate the surfaces of chlorite, lizardite, and quartz and promote the adsorption of xanthate, resulting in an enhanced floatability of these gangue minerals (Fornasiero and Ralston 2005).

Chlorite is a 2:1 type phyllosilicate with a general chemical formula of $(Mg_5Al)(AlSi_3)O_{10}(OH)_8$. Each repeating unit of chlorite has one magnesium hydroxide layer, which is also known as a brucite-like layer, and one mica-like layer (see Figure 1.8). The thickness between chlorite layers is about 1.4 nm. The lattice structure of the brucite-like layer and mica-like layer of chlorite has been imaged using atomic force microscopy (Vrdoljak et al. 1994). When a chlorite crystal is cleaved, both a mica-like face and brucite-like face can be exposed. It is expected that the mica-like face carries a permanent negative charge, as there are 25% of the silicon atoms substituted by aluminum atoms in the tetrahedral layer. This charge deficiency is compensated by the positively charged brucite-like layer. Both the negatively charged mica-like layer and the positively charged brucite-like layer contribute to the overall surface charge density. In addition to the basal plane surfaces, the edges of chlorite particles may also have a different charging behavior. The edge surface of phyllosilicates is composed of broken covalent or ionic bonds which have high polarity and a strong pH dependence (Fuerstenau and Pradip 2005; Nalaskowski et al. 2007).

Electrophoresis is a common method to determine the zeta potential, which represents the potential at the slipping plane when the particles are moving in the aqueous solution under the influence of an electric field. The pH value at which the zeta potential reaches zero is known as the isoelectric point (IEP). The zeta potential of chlorite has been studied by several researchers using the electrophoresis technique (Fornasiero and Ralston 2005; Sondi, Bišćan, and Pravdić 1996; Sondi, Milat, and Pravdić 1997; Sondi and Pravdić 1996). The measured IEP is in the range of pH 3 to pH 6, depending on different mineralogy and electrolyte conditions. Mular-Roberts titration is another technique to characterize the surface charging, as proposed by two researchers, Mular and Roberts, in 1966. In this method, the pH value of a suspension is measured at different ionic strengths. The suspension is first prepared at given pH and ionic strength, then the ionic strength is increased to yield a change in pH (Mular and Roberts 1966). When there is no change of pH, the pH value is determined as the point of zero charge (PZC), which represents the potential at the particle surface. Using Mular-Roberts titration technique, Alvarez-Silva et al. determined the PZC of chlorite as pH 4.7, compared to an electrophoretic IEP of pH < 3 (Alvarez-Silva et al. 2010).

Atomic force microscopy has been widely applied in the investigation of the surface properties for different minerals since first used in the study of fluorite (Assemi et al. 2006; Long et al. 2006; Nalaskowski et al. 2007; Yan et al. 2011; Yin and Drelich 2008; Zhao et al. 2008). According to the geometry of the AFM tips, several theoretical models have been developed based on the DLVO theory in which the electrostatic interaction and van der Waals interaction are considered. A common technique used for surface force measurements is known as the colloidal probe technique in which a small

particle with spherical shape is glued at the end of a tipless AFM cantilever (Nalaskowski et al. 2003; Wallqvist et al. 2006; Zhang, Yoon, and Eriksson 2007). The colloidal probe technique can greatly enhance the sensitivity of surface force measurements. However, the spherical particles used in the measurements are usually 5 to 20 microns in size. Thus, it is difficult to obtain a high resolution image during the surface force measurements. The roughness of the particle surfaces may also significantly influence the surface forces.

By using the colloidal probe technique, Nalaskowski et al. found the different surface charging behavior of the talc basal plane surface and the edge surface (Nalaskowski et al. 2007). However, the surface roughness of their samples was still too high to acquire reliable AFM force curves and perform a detailed quantitative analysis. Then Zhao et al. improved the quality of edge surfaces using a microtome cutting technique to create a smooth surface. Then the interaction forces between a silica probe particle and muscovite face and edge surfaces were measured (Zhao et al. 2008). Recently, Yan et al. successfully prepared ultra smooth (roughness < 1 nm) mica and talc face and edge surfaces. The anisotropic surface charging characteristics for mica and talc basal and edge planes have been characterized using atomic force microscopy (Yan et al. 2011). Their results showed that the PZC for both the mica and talc basal planes are less than pH 5.6. The edge surfaces for mica and talc are pH-dependent. The PZC of the edge surface for muscovite (~pH 7.5) is slightly lower than that for the talc edge surface (~pH 8.1).

This chapter discusses the surface charging of chlorite as a function of pH measured by electrophoresis and atomic force microscopy. The isoelectric points for the chlorite mica-like face, brucite-like face, and edge surfaces are determined from surface

force measurements using atomic force microscopy. In this way, the anisotropic charging properties for chlorite are established. It is expected that this research will provide a better understanding of anisotropic surface chemistry properties of chlorite, which is significant for developing suitable flotation reagent schedules (collectors, depressant, modifiers, and pH) and improving the flotation separation processes.

6.2 Materials and Methods

6.2.1 Sample Preparation

A high purity chlorite crystal with natural cleavage on the plane (001) was obtained from Chester, Pennsylvania. The sample was identified as pure clinochlore with (001) cleavage plane using x-ray diffraction (XRD). X-ray photoelectron spectroscopy (XPS) analysis showed that the chlorite sample contains 7.45% silicon, 4.93% aluminum, 9.87% magnesium, and trace amounts of sodium (0.2%), iron (0.31%), chromium (0.73%), and chloride (0.17%). A few flakes of chlorite sample were ground to -45 μm size to measure the zeta potential using the electrophoresis method.

One thin layer of chlorite was peeled from the chlorite crystal using sticky tape. Then, this thin layer of the chlorite crystal as well as the chlorite crystal itself were glued on two thoroughly cleaned glass substrates. Since chlorite is composed of alternating mica-like and brucite-like sheets, when a chlorite sample is cleaved, two different faces will be exposed. Therefore, by using this method, the chlorite samples with the exposure of the mica-like surface and the brucite-like surface were prepared. The schematic of this cleavage procedure is depicted in Figure 6.1. After keeping the sample in a petri-dish for 24 hrs until the glue was completely dried, the samples were mounted on magnetic disks as the substrate for study of the charging properties of chlorite surfaces using AFM.

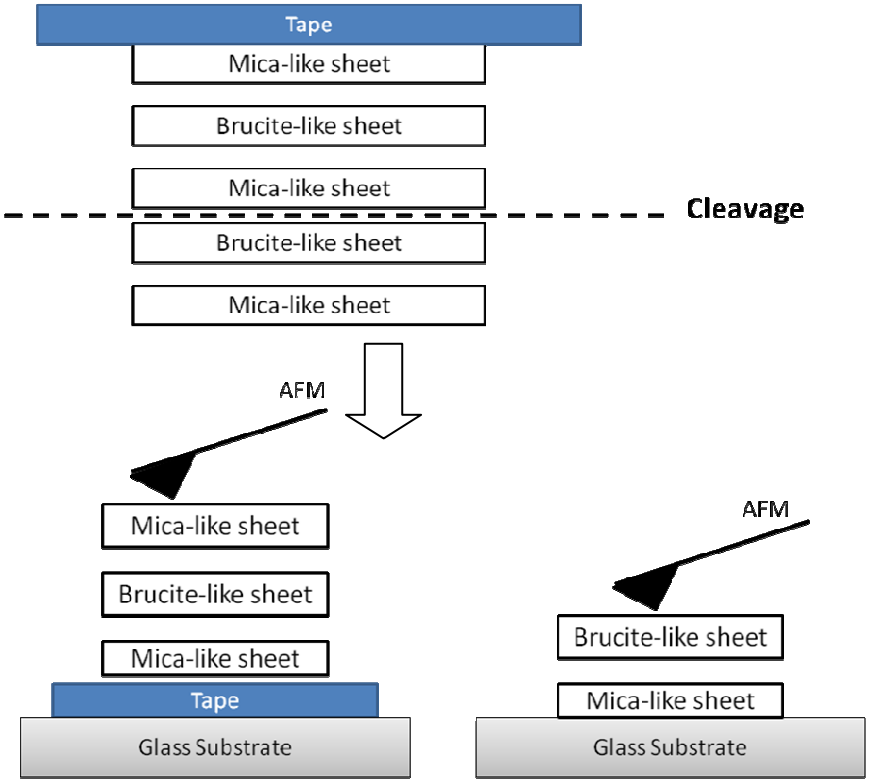

Figure 6.1 – Schematic of the preparation procedure for chlorite basal planes.

The chlorite edge surface was also prepared. A small flake of the chlorite sample was embeded in epoxy resin (Electron Microscopy Sciences, Hatfield, PA, USA) and baked for 24 hrs at 60 ˚C. See Figure 6.2 (A). Then the sample was trimmed by a razor blade under an optical microscope to make the sample perpendicular to the cutting edge. When the chlorite edge was exposed, the sample was glued on a magnetic disk and cut using the ultramicrotome (EM UC 7, Leica Microsystems Inc.) to obtain a smooth surface for subsequent AFM study. Before measuring the surface force by AFM, the samples were rinsed with Milli-Q water, ethanol, and cleaned with high purity nitrogen gas to remove any contaminants. The samples after cutting with the ultramicrotome are shown in Figure 6.2 (B).

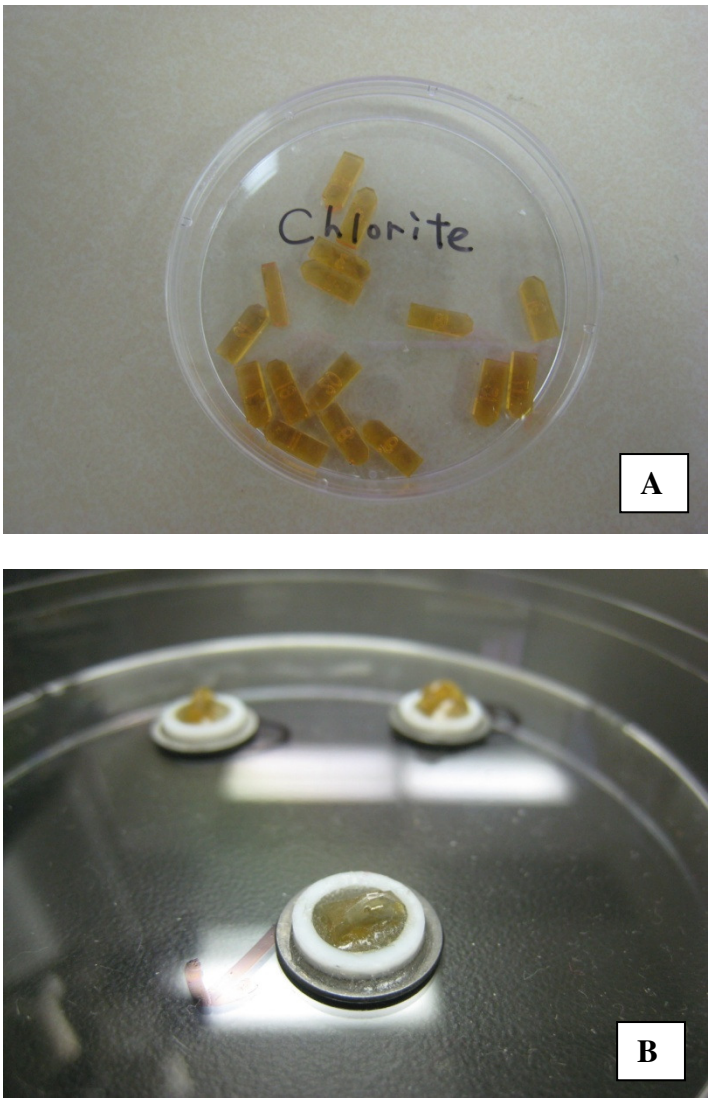

Figure 6.2 – Chlorite samples embedded in the epoxy resin (A) and the chlorite samples after the coarse cutting and ultramicrotome cutting with exposure of edge plane (B).

6.2.2 Zeta Potential Measurements

The zeta potential measurements were carried out by the electrophoresis technique (ZetaPALS, Brookhaven Instrument Corp.). A chlorite suspension with a concentration of 0.05% was prepared. The mobilities of chlorite particles were measured at varying pH and then converted to zeta-potentials (ξ) using Smoluchowski's model as follows:

$$U = \frac{\varepsilon\zeta}{4\pi\eta} E_{\infty} \tag{6-1}$$

where U is the particle mobility, E_{∞} is the applied electric field, and ε and η are the dielectric constant and viscosity of the solvent.

6.2.3 Surface Force Measurements Using AFM

A picoforce AFM with a Nanoscope V controller (Bruker Corporation, Santa Barbara, CA) was used with a PF-type scanner designed for picoforce measurements. A contact mode silicon nitride cantilever was used to study the surface charging of chlorite. The spring constant was determined by the thermal tuning function provided in Nanoscope v 7.20 software and this value is used later in data analysis. AFM images of chlorite basal planes and edge planes were collected before the surface force measurements. The images were captured with a scan size of 5 microns and scan rate of 1 Hz. The resolution of the image is 512 points/line.

The surface force measurements were conducted at the chlorite mica-like surface, the brucite-like surface, and the edge surface at five different locations in 1 mM KCl at pH 5.6, 8, and 9. At each location, five force curves were collected. All the force

measurements were performed at a scan rate of 1 Hz and captured at a resolution of 512 points/measurement. SPIP software (Image Metrology, Lyngby, Denmark) was used to convert the deflection-distance curves to force-distance curves. Baseline correction and hysteresis correction were involved in preparation of the force curves. The force-distance curves were fitted with the theoretical DLVO model under constant surface charge density or constant surface potential. The surface charge density and the surface potential of the substrates were obtained from fitting data to the DLVO theory.

6.2.4 Theoretical Model

The geometry of the silicon nitride AFM tip can be approximated as conical with a spherical cap at its apex. Geometry of the system and the parameters used are shown in Figure 6.3. The symbols α and β are the geometrical angles for the spherical cap at the tip end and conical tip with α+β=90°, D is the distance from the end of the tip to the substrate, L is the distance between a differential surface section of the tip and the substrate, r is the radius of the circle of the tip at a given vertical position, and R is the radius of the spherical cap at the tip end (Drelich, Long, and Yeung 2007).

The Derjaguin, Landau, Verwey, and Overbeek (DLVO) theoretical model with this geometry was derived and discussed in the literature (Drelich, Long, and Yeung 2007) and only the final equations are given here.

The van der Waals force between the spherical segment of the tip and flat substrate surface is given by:

$$F_{TS}^{vdw-S} = \frac{A}{6}\left[\frac{(R+D)-2L_1}{L_1^2} - \frac{R-D}{D^2}\right] \tag{6-2}$$

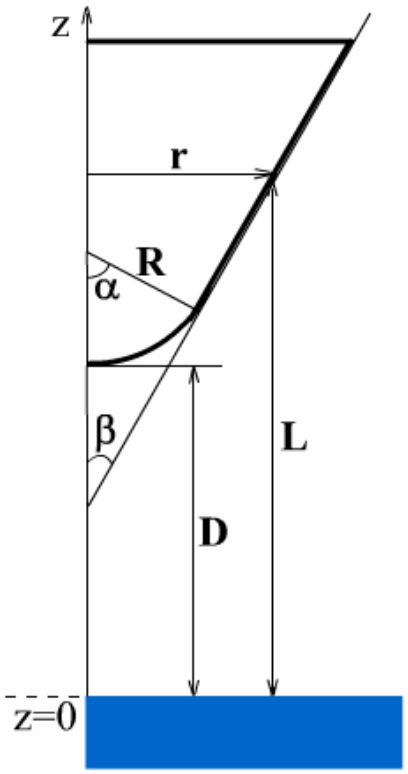

Figure 6.3 – Geometry of the system and parameters used for theoretical DLVO calculations.

The formula describing the van der Waals force for the conical segment of the AFM tip is:

$$F_{TS}^{vdw-C} = -\frac{A}{3\tan^2\alpha}\left(\frac{1.0}{L_1} + \frac{R\sin\alpha\tan\alpha - D - R(1-\cos\alpha)}{L_1^2}\right) \quad (6\text{-}3)$$

where L_1=D+R(1-cosα), A is the combined Hamaker constant, ε is the dielectric constant of the solution in this system, ε_0 is the permittivity of a vacuum, 1/κ is the Debye length, D is the distance between two surfaces, and subscripts 1 and 2 refer to two surfaces. (A_{water} = 3.7 × 10^{-20} J, A_{tip} = 1.62 × 10^{-19} J, $A_{chlorite}$ = 2.33 × 10^{-19} (Isrealachvili 1985, Vincent and Jean Marc 2007)).

The electrostatic force with constant surface potential for the spherical part and the conical part of the tip is given by:

$$F_{TS}^{S} = 4\pi\varepsilon_0\varepsilon\Phi_T\Phi_S\left(a_0e^{-\kappa D} - a_1{}^{-\kappa L_1}\right) - 2\pi\varepsilon_0\varepsilon\left(\Phi_T^2 + \Phi_S^2\right)\left(a_1e^{-2\kappa D} - a_3e^{-2\kappa L_1}\right) \tag{6-4}$$

where Φ_T and Φs are the surface potentials of AFM tip and surface, $a_0=\kappa R-1$, $a_1=\kappa R\cos\alpha-1$, $a_2=a_0+0.5$, and $a_3=a_1+0.5$:

$$F_{TS}^{C} = \frac{4\pi\varepsilon_0\varepsilon\kappa}{\tan\alpha}\left[b_1\Phi_T\Phi_Se^{-\kappa L_1} - b_2\frac{\left(\Phi_T^2 + \Phi_S^2\right)}{2}e^{-2\kappa L_1}\right] \tag{6-5}$$

The electrostatic force with constant surface charge density for the spherical part and the conical part of the tip is given by:

$$F_{TS}^{S} = \frac{4\pi}{\varepsilon_0\varepsilon\kappa^2}\sigma_T\sigma_S\left(a_0e^{-\kappa D} - a_1e^{-\kappa L_1}\right) + \frac{2\pi}{\varepsilon_0\varepsilon\kappa^2}\left(\sigma_T^2 + \sigma_S^2\right)\left(a_2e^{-2\kappa D} - a_3e^{-2\kappa L_1}\right) \tag{6-6}$$

$$F_{TS}^{C} = \frac{4\pi}{\varepsilon_0\varepsilon\kappa\tan\alpha}\left[b_1\sigma_T\sigma_Se^{-\kappa L_1} + b_2\frac{\left(\sigma_T^2 + \sigma_S^2\right)}{2}e^{-2\kappa L_1}\right] \tag{6-7}$$

where σ_T and σs are the surface charge densities of AFM tip and surface:

$$b_1 = \left[R\sin\alpha - \frac{D + R(1-\cos\alpha)}{\tan\alpha}\right] + \frac{1}{\tan\alpha}\left[\left(L_1 + \frac{1}{\kappa}\right)\right] \tag{6-8}$$

$$b_2 = \left[R\sin\alpha - \frac{D + R(1-\cos\alpha)}{\tan\alpha}\right] + \frac{1}{\tan\alpha}\left[\left(L_1 + \frac{1}{2\kappa}\right)\right] \tag{6-9}$$

The total electrostatic force between the tip and the substrate can then be obtained for either constant surface potential or constant surface charge density by the sum of these two parts:

$$F^e = F_{TS}^S + F_{TS}^C \tag{6-10}$$

The total DLVO force for the system with geometry shown in Figure 2.6 is given by adding the electrostatic force and the van der Waals force:

$$F = F^e + F^{vdw} \tag{6-11}$$

The surface potential is calculated from the surface charge density using the Grahame equation which is described in eq. (3-7), (3-8), and (3-9).

6.3 Results and Discussions

6.3.1 Zeta Potential of Chlorite Measured by Electrophoresis

The zeta potentials of chlorite particles determined by electrophoresis are shown in Figure 6.4. The results indicate that the isoelectric point (IEP) of chlorite is around pH 5.5. This result is in good agreement with the literature (Fornasiero and Ralston 2005). Chlorite is composed of alternating mica-like and brucite-like layers (see Figure 1.8). Both faces can be exposed at a particle surface and contribute to the surface charge density of chlorite. Usually, mica group minerals have an isoelectric point less than pH 2, whereas brucite has a higher isoelectric point which is around pH 11 (Pokrovsky and Schott 2004). The measured IEP for chlorite in this study is close to the average value of the IEP for mica and brucite.

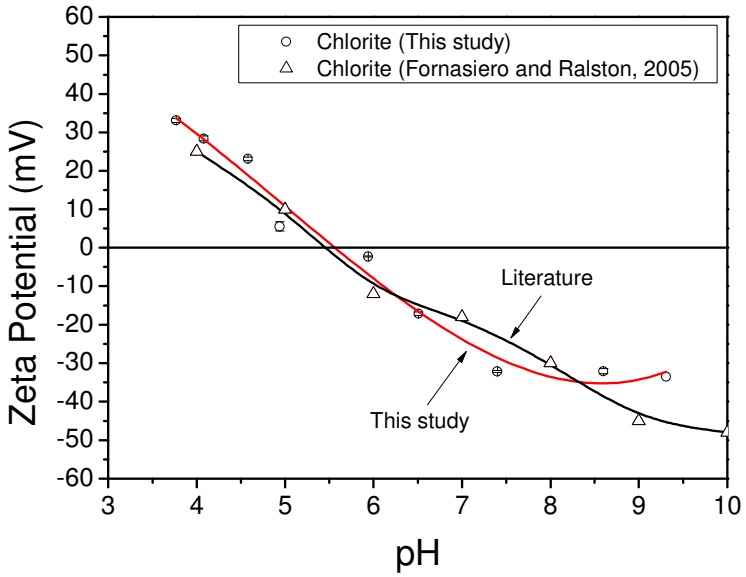

Figure 6.4 – Zeta potential of chlorite as a function of pH measured in 1mM KCl by the electrophoresis method compared with results reported in the literature.

However, it should be noted that the isoelectric point determined from electrophoretic mobility may be misleading due to the basic assumption in the Smoluchowski model that the particles are of spherical shape and of homogeneous surface charge density (Wypych and Satyanarayana 2004; Nalaskowski et al. 2007). It is known that chlorite is a mineral with platy shape and anisotropic surface characteristics. The surface charging at the two basal planes (mica-like face and brucite-like face) and at the edge surface can be different. Therefore, the zeta potential obtained from electrophoresis with the Smoluchowski model may not reflect the surface potential at the shear plane. So far, there is no model available to describe the movement of platy shaped particles with anisotropic surface charging characteristics. Hence, the anisotropic surface charge of chlorite needs to be characterized using other techniques.

6.3.2 Interaction Forces at Chlorite Basal Plane Surfaces

Surface forces were measured at both the mica-like face surface and the brucite-like face surface. A representative AFM image of the chlorite basal plane surface is shown in Figure 6.5. This surface was determined to be the mica-like face by the subsequent AFM surface force measurements. The root-mean-square surface roughness for chlorite basal planes is determined as 0.1 nm to 0.4 nm. This roughness suggests that the chlorite basal planes are smooth enough to satisfy the requirement of AFM surface force measurement.

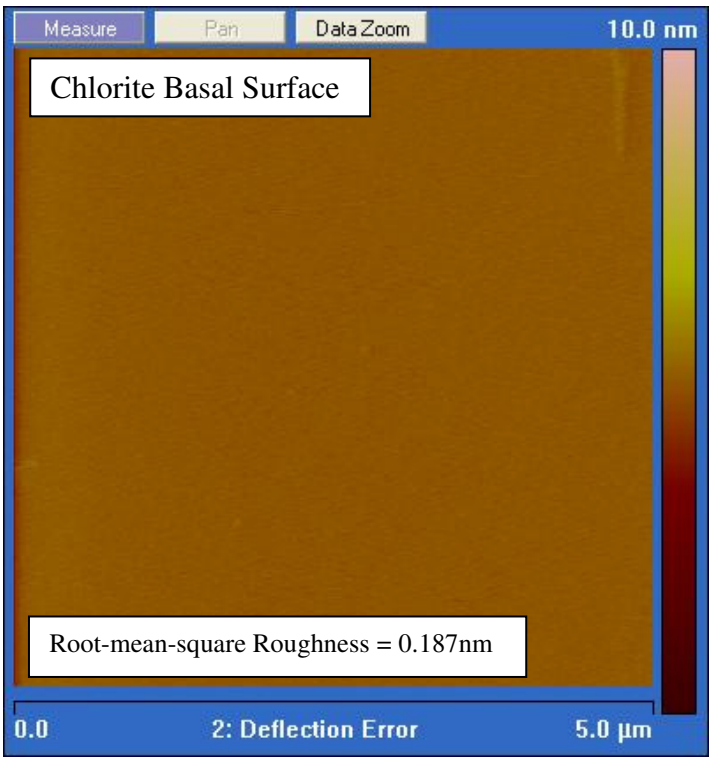

Figure 6.5 – Typical AFM image of chlorite basal plane surface.

The approaching surface force curves were collected at both of the two basal plane surfaces of chlorite. The typical interaction forces between the silicon nitride AFM tip and the chlorite mica-like surface in 1mM KCl solutions with varying pH values are shown in Figure 6.6. The open circles on the graphs refer to the experimental data, whereas the solid lines represent the calculated DLVO theoretical model which is described in Section 6.2.4. The surface force curves were fitted using constant surface charge density and constant surface potential.

During the curve fitting, the surface charge densities of the silicon nitride AFM tip at different pH values were taken from the literature (Yan et al. 2011). It has been noticed that the isoelectric point of the silicon nitride AFM tip is around pH 4.0. Thus, the tip should be negatively charged at pH 5.6, 8.0, and 9.0. As shown in Figure 6.6, experimental surface force curves are in good agreement with the curves calculated from the theoretical model. The long-range repulsive forces were observed at all three pH conditions. The magnitude of the repulsion force gradually increases with an increase in pH. The results indicate that the chlorite mica-like face is negatively charged in this pH range and the IEP of the chlorite mica-like face is below pH 5.6.

Figure 6.7 shows the interaction forces between the silicon nitride tip and the chlorite brucite-like surface in 1mM KCl solutions at pH 5.6, 8.0, and 9.0. In contrast to the mica-like face of chlorite, attractive interactions dominate at all the three pH values, suggesting that the brucite-like layer of chlorite is positively charged in this pH range and the IEP of the chlorite brucite-like face should be above pH 9. In order to prevent the precipitation of magnesium, the surface force measurements were not performed in the solution with pH value greater than pH 9.

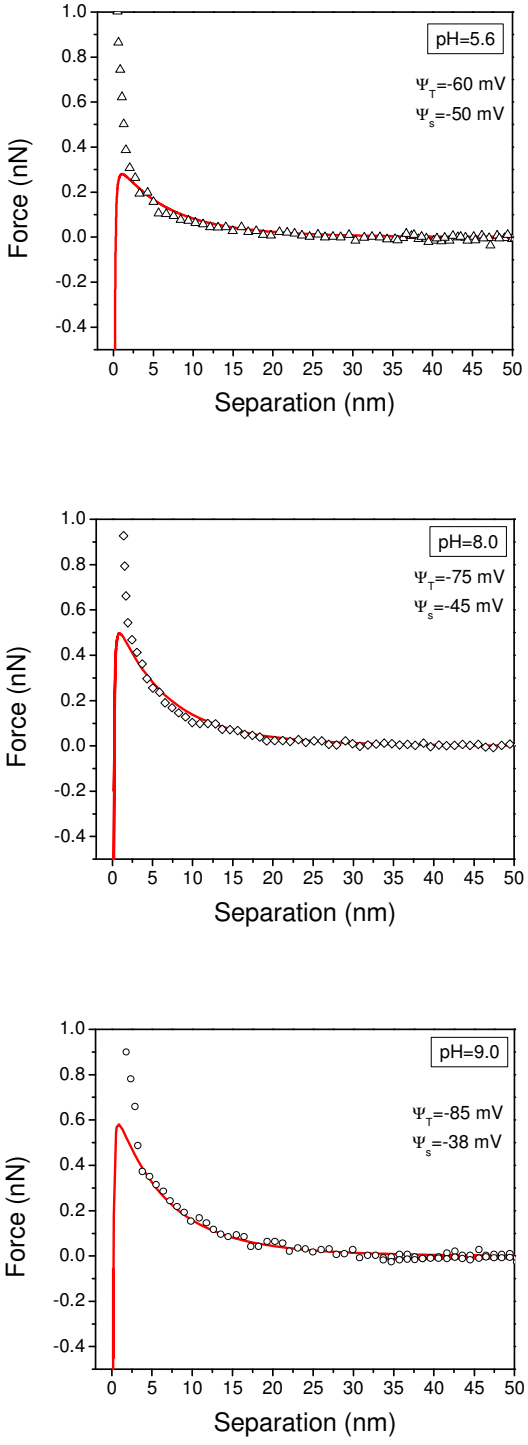

Figure 6.6 – Interaction forces between a silicon nitride AFM tip and chlorite mica-like basal plane surface in 1mM KCl at pH 5.6, 8.0, and 9.0. The solid lines represent the theoretical DLVO fit. Ψ_T is the surface potential of the silicon nitride AFM tip and Ψ_S is the surface potential of the chlorite mica-like surface.

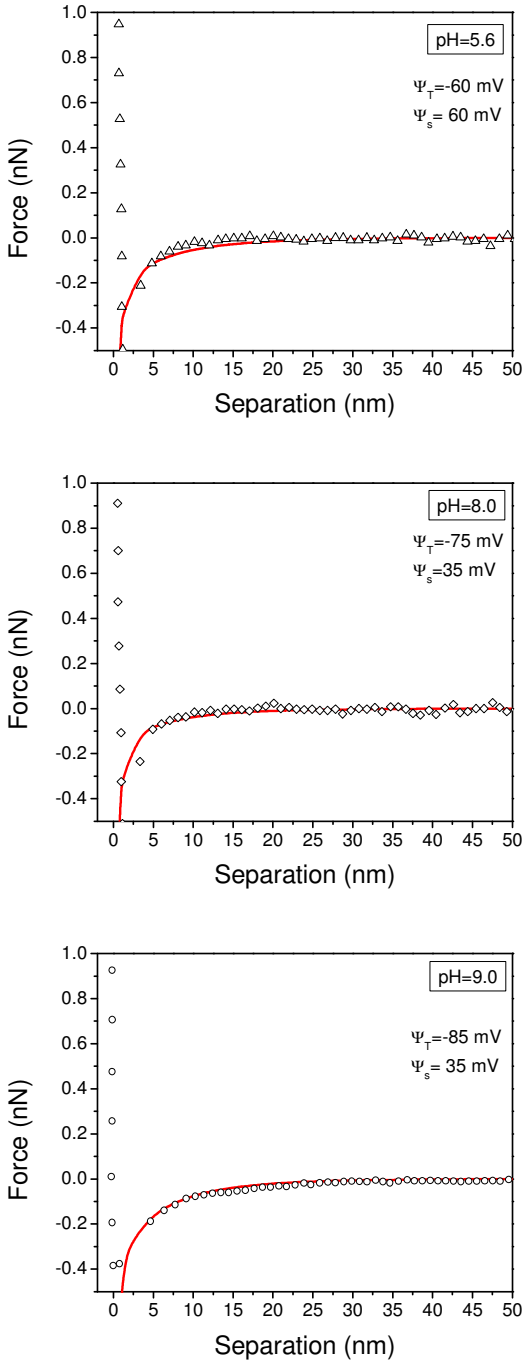

Figure 6.7 – Interaction forces between a silicon nitride AFM tip and chlorite brucite-like basal plane surface in 1mM KCl at pH 5.6, 8.0, and 9.0. The solid lines represent the theoretical DLVO fit. Ψ_T is the surface potential of the silicon nitride AFM tip and Ψ_S is the surface potential of the chlorite brucite-like surface.

6.3.3 Interaction Forces at Chlorite Edge Surfaces

A representative AFM image of the chlorite edge surface is shown in Figure 6.8. The root-mean-square surface roughness was determined to be 0.692 nm. It confirms that the ultramicrotome cutting technique is capable of creating a molecularly smooth flat surface which can be used for AFM surface force measurements. As shown in Figure 6.8, the pattern of lines is explained to arise from the chlorite sheets. The thicknesses between the lines were measured to be 80 nm to 130 nm. Compared to the thicknesses between repeating chlorite units which is about 1.4 nm, the results suggest that there are about 60 to 90 repeating units between two lines.

The surface force measurements were performed at the well-prepared chlorite edge surface using AFM. Representative surface force curves between the silicon nitride AFM tip and chlorite edge surface in 1mM KCl with varying pH values are shown in Figure 6.9.

The experimental data were fitted with the theoretical DLVO model and good agreement was observed. At pH 5.6 and 8.0, attractive interaction forces were found between the AFM tip and chlorite edge surface. When the pH value of the electrolyte was increased to pH 9.0, the interaction force became repulsive. Since the silicon nitride AFM tip is negatively charged at all three pH conditions, these surface force results suggest that the chlorite edge surface is pH-dependent. It is positively charged below pH 8.0 and negatively charged above 9.0, indicating that the IEP of the chlorite edge lies between pH 8.0 and pH 9.0.

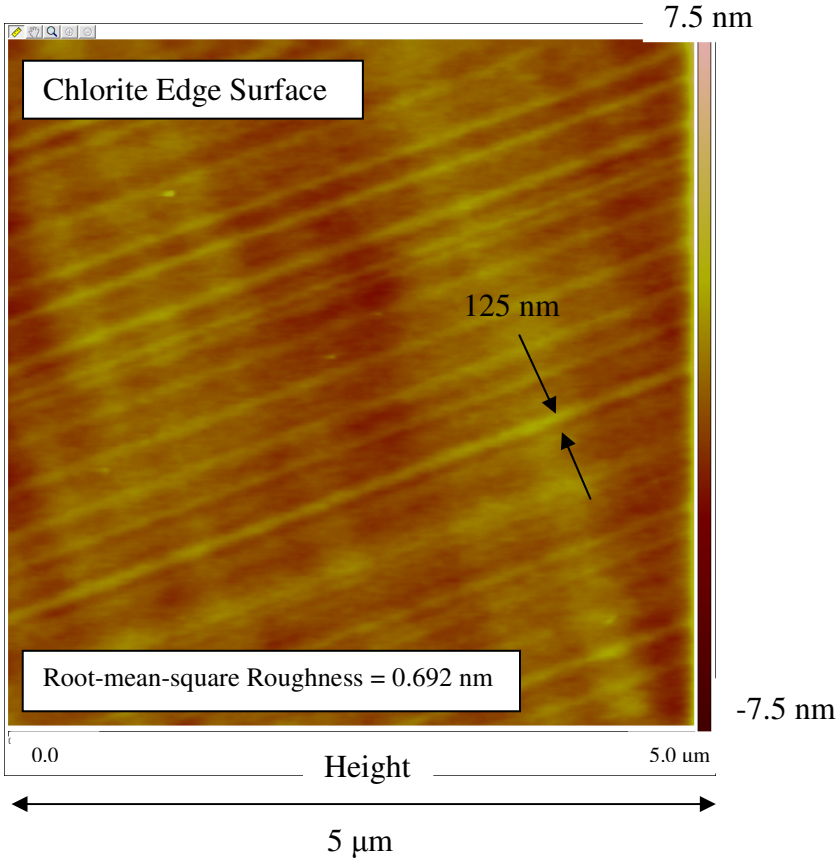

Figure 6.8 – Typical AFM image of chlorite edge plane.

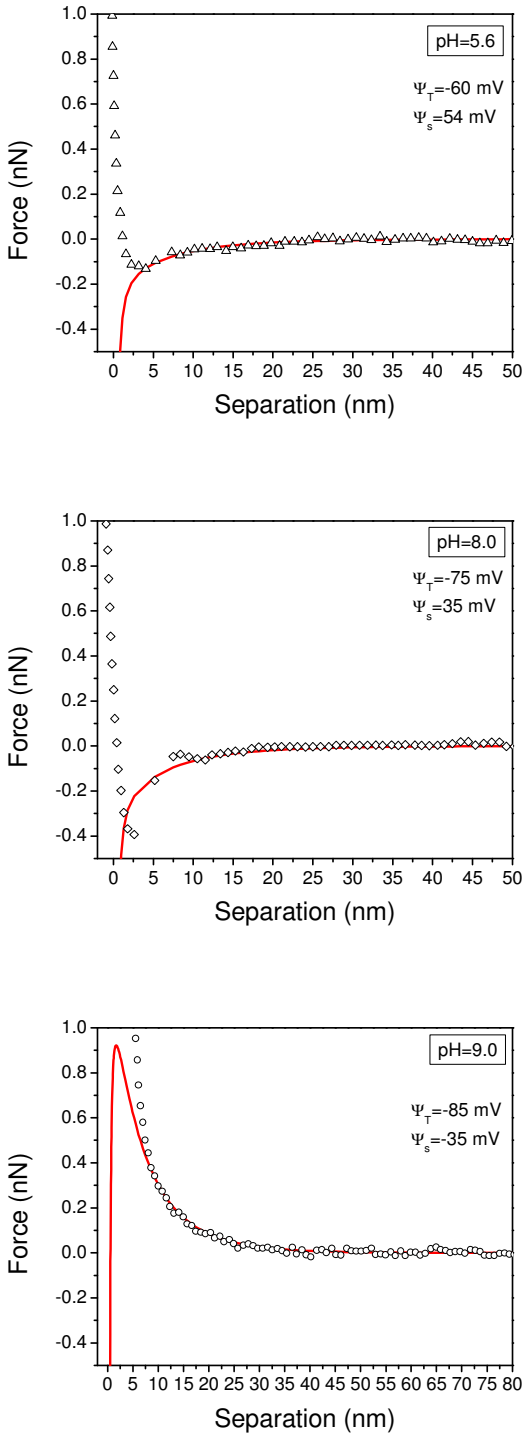

Figure 6.9 – Interaction forces between a silicon nitride AFM tip and chlorite edge surface in 1mM KCl at pH 5.6, 8.0, and 9.0. The solid lines represent the theoretical DLVO fit. Ψ_T is the surface potential of the silicon nitride AFM tip and Ψ_S is the surface potential of the chlorite edge surface.

6.3.4 Surface Potential and Surface Charge Density

The surface charge densities and surface potentials of the chlorite mica-like surface and the brucite-like surface are shown in Figure 6.10 as a function of pH. The magnitude of surface charge density and surface potential were determined from fitting the experimental force curves to the DLVO model.

At pH 5.6, 8.0, and 9.0, the mica-like face of chlorite is negatively charged, with the surface potential between -45 mV to -50 mV and the surface charge density between -5.8 mC/m^2 to -6.6 mC/m^2. It is noted that the surface potential of the chlorite mica-like face is nearly constant over the pH range. This is attributed to the fact that there is a permanent and fixed amount of isomorphous substitution of Si^{4+} by Al^{3+} in the chlorite mica-like face. It is known that the silica tetrahedral basal surface which has a hexagonal ring structure is difficult to protonate. Therefore, the charge deficiency caused by lattice substitution is believed to account for the permanent negative charge on the basal plane.

Yan et al. characterized the surface charging of muscovite and talc basal planes using AFM (Yan et al. 2011). Their results are shown in Figure 6.10 (B) for comparison. Similar to the chlorite mica-like face, the basal planes for talc and muscovite are also negatively charged and the surface potentials are nearly constant. These results confirm the inert nature of the silica tetrahedral face for phyllosilicates minerals. However, it can be noted that the magnitude of the surface potentials for the basal planes of these three phyllosilicates are in a sequence of $\Psi(\text{talc}) < \Psi(\text{chlorite mica-like}) < \Psi(\text{muscovite})$. This may be due to the different level of isomorphous substitution.

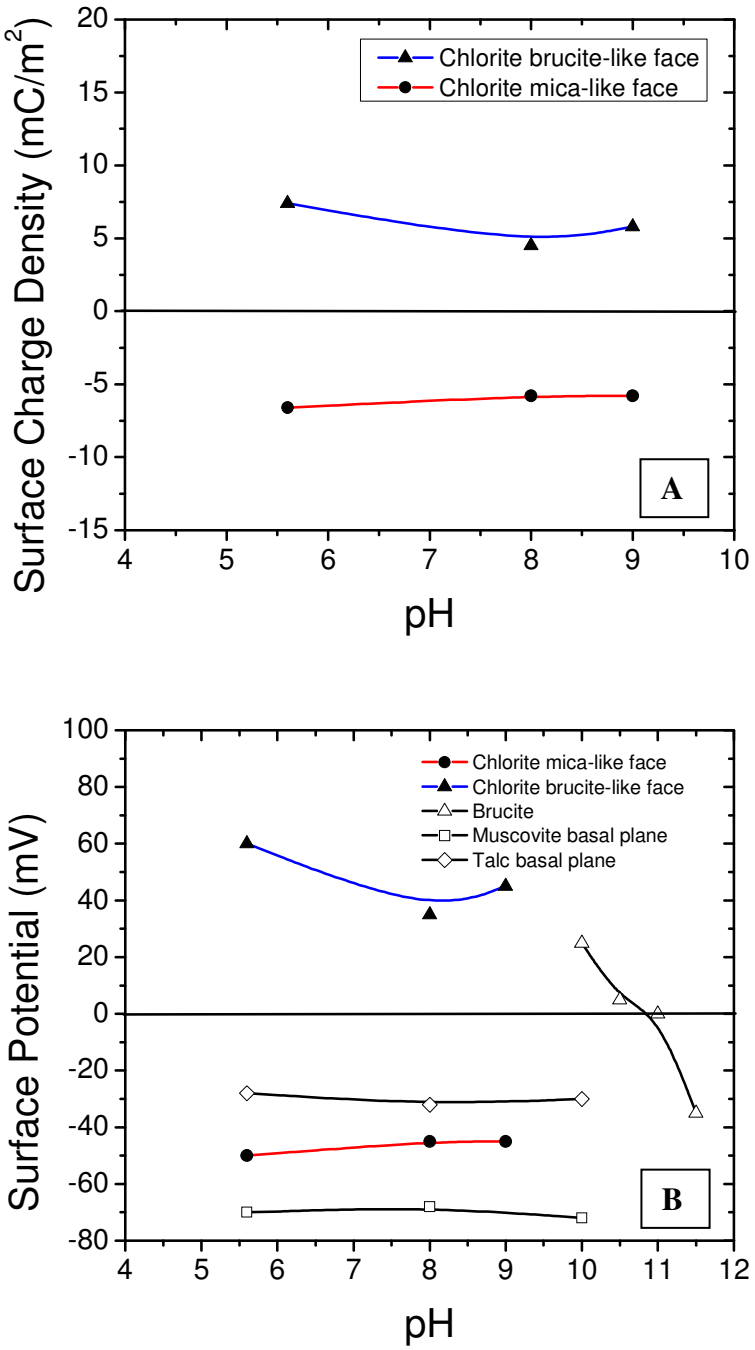

Figure 6.10 – Surface charge density (A) and surface potential (B) of the chlorite mica-like basal plane surface and brucite-like basal plane surface as a function of pH. The surface potentials of chlorite basal planes are compared with the literature results.

In a perfect muscovite lattice, the isomorphous substitution should be 25%. In contrast, talc has a much lower amount of isomorphous substitution (0.01% - 3.4%), which results in a lower surface potential (Deer, Howie, and Zussman 1997). In the case of chlorite, Al^{3+} could be present in both the mica-like face and in the brucite-like face by isomorphous subsitution. Thus, the level of substitution in the mica-like face is difficult to estimate. Moreover, from the elemental composition analysis, it can be noticed that other cations including Fe^{2+}, Cr^{2+}, and Na^{+} are also involved in the chlorite lattice. These cations will also affect the magnitude of the surface potential.

The surface charge densities and surface potentials of the chlorite brucite-like face are also plotted and shown in Figure 6.10. At all three pH values, the brucite-like face of chlorite is positively charged. The surface potentials are in a range of 35 mV to 60 mV and the surface charge densities are between 4.5 mC/m^2 to 7.5 mC/m^2. A slight decrease in surface potential with increasing pH was observed, suggesting that the brucite-like face of chlorite is slightly pH-dependent.

In order to compare the surface charging behavior of the chlorite brucite-like face and brucite, the surface potential of brucite particles from electrophoresis measurements reported by Pokrovsky and Schott are also shown in Figure 6.10 (B) (Pokrovsky and Schott 2004). Below pH 11.0, the brucite particles are positively charged which is similar to the chlorite brucite-like face. Nevertheless, as mentioned previously, the Al^{3+} cations are also present in the chlorite brucite-like layer. Thus, the IEP of the chlorite brucite-like face could be lower than pH 11.0.

Figure 6.11 shows the surface charge density and surface potential of the chlorite edge surface in 1mM KCl at pH 5.6, 8.0, and 9.0. At pH 5.6 and pH 8.0, the surface potentials of the chlorite edge surface are positive with magnitudes of 54 mV and 35 mV. When increasing the pH value to pH 9.0, the surface potential is reversed to negative and the surface potential is -35 mV. These results suggest that the chlorite edge surface is strongly pH-dependent and the IEP is estimated to be around pH 8.5.

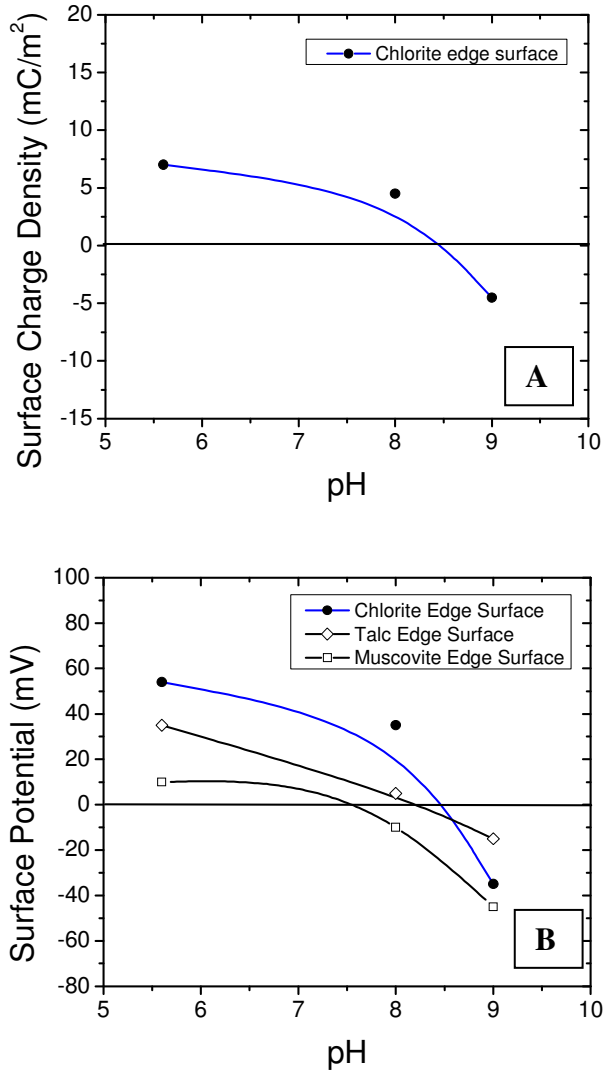

Figure 6.11 – Surface charge density (A) and surface potential (B) of the chlorite edge surface as function of pH. The results are compared with the surface potentials of talc and muscovite edge surfaces from the literature.

As shown in Figure 6.11 (B), the surface potentials of the chlorite edge surface are compared with the surface potential values of muscovite and talc edge surfaces from the literature (Yan et al. 2011). It is noted that the IEP of the chlorite edge surface (~pH 8.5) is higher than the IEP of the muscovite edge surface (~pH 7.5) and talc edge surface (~pH 8.1). The charges at the edge plane of phyllosilicates mainly arise from the protonation and deprotonation reactions of the broken bonds of the surface groups. The general reaction formula is given as:

$$A^x + H^+ = AH^{x+1}$$

where A^x represents a functional group with a charge of x and AH^{x+1} is the protonated form. Based on a MUltiSIteComplexation model (MUSIC), Avena et al. studied the proton affinity of different surface groups at both basal and edge planes of phyllosilicates (Avena et al. 2003; Nagashima and Blum 1999). The intrinsic protonation constants K_H of surface functional groups were calculated to describe the proton affinity and their results are shown in Table 6.1. They found that the protonation constant for the siloxane group is very low (log K_H ~ -16.9), suggesting that the siloxane structure is difficult to protonate. On the contrary, the surface functional groups at edge surfaces are more reactive and can be protonated in the normal pH range. The groups of Mg-$OH^{2/3-}$ and Al-$OH^{1/2-}$ are found to be the dominant charging groups at phyllosilicate edge surfaces. They can be protonated and become positively charge through the following reactions:

$$MgOH^{-2/3} + H^+ = MgOH^{+1/3}$$

$$AlOH^{-1/2} + H^+ = AlOH^{+1/2}$$

Table 6.1 – The protonation constants (log K_H) of the surface groups in phyllosilicates (Avena, Mariscal, and De Pauli 2003, Yan et al. 2011).

Surface group	Location	Log K_H^{int}
Al_2–OH	Basal surface	−1.5
Al_2–O^{1-}	Basal surface	12.3
Si_2–O	Basal surface	−16.9
SiAl–O^{x}	Edge surface	−16.9 to 12.3
Si–OH	Edge surface	−1.9
Si–O^{1-}	Edge surface	11.9
Al–$OH^{1/2-}$	Edge surface	7.9-9.9
Mg-$OH^{2/3-}$	Edge surface	10.0

From Table 6.1, it can be noted that the protonation constant for Mg-$OH^{2/3-}$ is higher than Al-$OH^{1/2-}$, which indicates that Mg-$OH^{2/3-}$ is easier to protonate. Also, it explains the fact that brucite has higher PZC than gibbisite. Since the edge surfaces of muscovite and talc contain the Al-$OH^{1/2-}$ groups and Mg-$OH^{2/3-}$ groups, respectively, the talc edge surface should have a higher PZC than the muscovite edge surface. This theoretical analysis has been confirmed by the experimental AFM results from the literature (Yan et al. 2011).

In the case of the chlorite edge surface, Mg-$OH^{2/3-}$ is the main charging functional group, although there is a small amount of Al-$OH^{1/2-}$ present in the brucite-like layer. Theoretically, the ratio of Mg to Al in the chlorite octahedral layer (both mica-like layer and brucite-like layer) is 5:1. Instead of interlayer cations, chlorite has an additional brucite-like layer between two mica-like layers, leading to a greater amount of Mg-$OH^{2/3-}$. Based on the crystal structure information, the ratio of the amount of Mg-$OH^{2/3-}$ in talc

to that in chlorite is 3:4. Therefore, the chlorite edge surface should be more positively charged at a given pH. This is in good agreement with the AFM surface force measurements results in this study which show that chlorite has a higher IEP value than talc and muscovite.

It has been reported that chlorite can be floated with both cationic collectors (alkyl amines, alkyl ether amines, and quaternary ammonium salts) as well as the anionic collectors (alkyl phosphonic acids, oleic acids, and xanthate) (Silvester, Bruckard, and Woodcock 2011). Although the results from electrophoresis measurement cannot fully explain these flotation results, the establishment of the anisotropic surface charging of chlorite may help to explain the observed flotation results. For example, Zheng et al. studied the flotation of chlorite as a single mineral system and they found that the chlorite can be floated using lauryl amine with highest recovery (~50%) between pH 7 and pH 9 (Zheng et al. 2009). Also, chlorite can be floated using oleic acid. It is interesting that the recovery of chlorite at pH 8 with oleic acid is similar to that with lauryl amine (~50%), suggesting that both the cationic collector and anionic collector can adsorb at the chlorite surface at pH 8. According to the results of this study, the chlorite mica-like basal plane surface is negatively charged at pH 8, whereas the brucite-like basal surface and the edge surface are positively charged. Therefore, under these conditions, the adsorption of the lauryl amine could occur at the mica-like surface and the oleic acid could adsorb at the brucite-like basal plane surface and at the edge surface, leading to flotation by either cationic or anionic surfactants (collectors), as observed experimentally. Clearly, the fundamental information on anisotropic surface charge characteristics of chlorite derived

from this study allows design of more effective flotation reagent systems for chlorite-containing mineral systems.

6.4 Summary

The surface charge properties of chlorite, which is a mixed layer phyllosilicate, have been characterized by measuring the surface forces between a silicon nitride tip and the chlorite surfaces using atomic force microscopy. The mica-like face and brucite-like face of chlorite were prepared by splitting a chlorite crystal along its natural cleavage plane (001). Moreover, the chlorite edge surface was created using the ultramicrotome cutting technique. Both the basal plane surfaces and the edge surface have a surface roughness less than 1 nm, which should satisfy the requirement for AFM surface force measurements.

The surface force measurements were conducted in 1mM KCl at pH 5.6, 8.0, and 9.0. The measured surface forces were fitted with the theoretical DLVO model. The surface potential and surface charge density for chlorite basal plane surfaces and the edge surface were then determined from the fitting curve. A significant difference in charging behavior has been observed for the chlorite mica-like face and the brucite-like face. At all three pH conditions, the chlorite mica-like face is negatively charged with the IEP less than pH 5.6. In contrast, the chlorite brucite-like face is positively charged in this pH range and the IEP is higher than pH 9.0.

Surface charging of the chlorite edge surface has also been examined. The transition from positive charge to negative charge was observed between pH 8.0 and pH 9.0. From the curve fitting, the IEP of the chlorite edge surface was determined to be pH

8.5. This value is slightly higher than the IEP for muscovite and talc edge surfaces, which may be due to the greater number of magnesium hydroxide groups at the chlorite edge.

In this study, the anisotropic surface characteristics of chlorite have been demonstrated. The surface charging behavior of the chlorite basal plane surfaces and the edge surface has been established as a function of pH. The results from this research have established a better understanding of the charging behavior for phyllosilicates. Moreover, it is expected that the results will provide a fundmental foundation for solving flotation issues, including collector adsorption, slime coating, and particle interactions.

CHAPTER 7

SUMMARY AND CONCLUSIONS

The major objective of this dissertation is to investigate the surface properties of selected phyllosilicates using both experimental techniques and theoretical methods. In particular, the wetting characteristics and surface charging behavior of a bilayer phyllosilicate kaolinite and a mixed-layer phyllosilicate chlorite were discussed. Also, the effect of lattice isomorphous substitutions on the surface hydrophobicity of silica tetrahedral basal planes was studied using molecular dynamics simulation. The accomplishments and contributions are summarized as follows.

In order to characterize the anisotropic wettability of the submicron phyllosilicate particles, an AFM-based technique was developed. The concept of this technique is to measure the surface forces between a hydrophobic diamond-like-carbon (DLC) AFM tip and the substrate of interest. Then the surface hydrophobicity can be determined by the direction and magnitude of the hydrophobic attraction force. By measuring the surface force between the DLC tip and a well-cleaned glass substrate, the isoelectric point of the DLC tip was determined as around pH 4. It is expected that the electrostatic interaction is insignificant at this pH value. This AFM-based technique was validated by performing the surface force measurements between the DLC tip and two hydrophobized silica substrates with different wettability. Different magnitudes were observed for the

attractive hydrophobic forces at the two silica substrates, confirming that this technique can be utilized to determine the surface hydrophobicity.

Using this technique, the wetting characteristics of the kaolinite silica face and alumina face have been determined. The results from AFM surface force measurements showed that the kaolinite silica face has a moderate degree of hydrophobicity which may be due to the lack of hydrogen bonding sites at the siloxane-terminated silica tetrahedral face. Theoretical calculation of van der Waals interaction suggests that the short-range hydrophobic force detected between the DLC tip and the kaolinite silica basal surface may originate from the van der Waals force when considering the water exclusion zone at the hydrophobic surfaces. In contrast, the alumina face is determined as hydrophilic as the hydroxyl groups at the alumina face are capable of providing the hydrogen bonding sites. Results from molecular dynamics simulation (MDS) also support the findings from the AFM study.

The effects of isomorphous lattice substitution on the hydrophobicity and the interfacial water structure of the phyllosilicate silica tetrahedral basal surfaces were studied using molecular dynamics simulation. The results show that the water contact angle decreases significantly with the increasing amount of isomorphous substitutions. The relationship between the percentage of isomorphous substitution and water contact angle was established and the water contact angle of the kaolinite silica face was predicted. Moreover, it has been found that the isomorphous substitutions also greatly affect the interfacial water structure, which may be due to the surface charge imbalance and the hydration of the interlayer potassium ions.

The anisotropic surface charging of chlorite has been established based on the AFM surface force measurements. The results show that the surface charging of the chlorite mica-like face differs from the chlorite brucite-like face. At pH 5.6 8.0 and 9.0, the chlorite mica-like face is negatively charged with the IEP less than pH 5.6. In contrast, the chlorite brucite-like face is positively charged in this pH range and the IEP is higher than pH 9.0. The surface charging of the chlorite edge surface was found to be pH-dependent. The IEP of the chlorite edge surface was determined as pH 8.5, which is slightly higher than the edge surfaces of talc and muscovite due to the greater content of magnesium hydroxide at the chlorite edge surface. It is expected that these findings will help to explain the observed flotation behavior.

REFERENCES

Alvarez-Silva, M., A. Uribe-Salas, M. Mirnezami, and J. A. Finch. 2010. The point of zero charge of phyllosilicate minerals using the Mular–Roberts titration technique. *Minerals Engineering* 23:383-389.

Ardizzone, S., G. Spinolo, and S. Trasatti. 1995. The point of zero charge of Co3O4 prepared by thermal decomposition of basic cobalt carbonate. *Electrochimica Acta* 40:2683-2686.

Assemi, S., J. Nalaskowski, J. D. Miller, and W. P. Johnson. 2006. Isoelectric Point of Fluorite by Direct Force Measurements Using Atomic Force Microscopy. *Langmuir* 22:1403-1405.

Assemi, S., A. V. Nguyen, and J. D. Miller. 2008. Direct measurement of particle-bubble interaction forces using atomic force microscopy. *International Journal of Mineral Processing* 89:65-70.

Avena, M. J., and C. P. De Pauli. 1998. Proton Adsorption and Electrokinetics of an Argentinean Montmorillonite. *Journal of Colloid and Interface Science* 202:195-204.

Avena, M. J., M. M. Mariscal, and C. P. De Pauli. 2003. Proton binding at clay surfaces in water. *Applied Clay Science* 24:3-9.

Berendsen, H. J. C., J. R. Grigera, and T. P. Straatsma. 1987. The missing term in effective pair potentials. *Journal of Physical Chemistry* 91:6269-71.

Bhattacharjee, S., and M. Elimelech. 1997. Surface element integration: A novel technique for evaluation of DLVO interaction between a particle and a flat plate. *Journal of Colloid and Interface Science* 193:273-273.

Bickmore, B. R., D. Bosbach, M. F. Hochella, L. Charlet, and E. Rufe. 2001. In situ atomic force microscopy study of hectorite and nontronite dissolution: Implications for phyllosilicate edge surface structures and dissolution mechanisms. *American Mineralogist* 86:411-423.

Bish, D. L., and R. B. Von Dreele. 1989. Rietveld refinement of non-hydrogen atomic positions in kaolinite. *Clays and Clay Minerals* 37:289-296.

Bleam, W. F. 1990. The nature of cation-substitution sites in phyllosilicates. *Clays and Clay Minerals* 38:527-536.

Bleam, W. F., G. J. Welhouse, and M. A. Janowiak. 1993. The surface Coulomb energy and proton Coulomb potentials of pyrophyllite {010}, {110}, {100}, and {130} edges. *Clays and Clay Minerals* 41:305-316.

Brady, P. V., R. T. Cygan, and K. L. Nagy. 1996. Molecular Controls on Kaolinite Surface Charge. *Journal of Colloid and Interface Science* 183:356-364.

Bremmell, K. E., D. Fornasiero, and J. Ralston. 2005. Pentlandite-lizardite interactions and implications for their separation by flotation. *Colloids and Surfaces A: Physicochemical and Engineering Aspects* 252:207-212.

Bremmell, K. E., G. J. Jameson, and S. Biggs. 1999. Adsorption of ionic surfactants in particulate systems: flotation, stability, and interaction forces. *Colloids and Surfaces A: Physicochemical and Engineering Aspects* 146:75-87.

Bryant, E. M., R. S. Bowman, and J. S. Buckley. 2006. Wetting alteration of mica surfaces with polyethoxylated amine surfactants. *Journal of Petroleum Science and Engineering* 52:244-252.

Burdukova, E., G. C. Van Leerdam, F. E. Prins, R. G. Smeink, D. J. Bradshaw, and J. S. Laskowski. 2008. Effect of calcium ions on the adsorption of CMC onto the basal planes of New York talc - A ToF-SIMS study. *Minerals Engineering* 21:1020-1025.

Case, D. A., T. E. Cheatham Iii, T. Darden, H. Gohlke, R. Luo, K. M. Merz Jr, A. Onufriev, C. Simmerling, B. Wang, and R. J. Woods. 2005. The Amber biomolecular simulation programs. *Journal of Computational Chemistry* 26:1668-1688.

Chalaturnyk, R. J., J. D. Scott, and B. Ozum. 2002. Management of oil sands tailings. *Pet. Sci. Technol.* 20:1025-1046.

Cygan, R. T., J.-J. Liang, and A. G. Kalinichev. 2004. Molecular models of hydroxide, oxyhydroxide, and clay phases and the development of a general force field. *Journal of Physical Chemistry B* 108:1255-1266.

Dang-Vu, T., R. Jha, S.-Y. Wu, D. D. Tannant, J. Masliyah, and Z. Xu. 2009. Wettability determination of solids isolated from oil sands. *Colloids and Surfaces A: Physicochemical and Engineering Aspects* 337:80-90.

Deer, W. A., R. A. Howie, and J. Zussman. 1997. *Rock Forming Minerals*, 2nd edition. Vol. 2B. London: The Geological Society.

Drelich, J., J. Long, and A. Yeung. 2007. Determining Surface Potential of the Bitumen-Water Interface at Nanoscale Resolution using Atomic Force Microscopy. *The Canadian Journal of Chemical Engineering* 85:625-634.

Du, H., and J. D. Miller. 2007a. A molecular dynamics simulation study of water structure and adsorption states at talc surfaces. *International Journal of Mineral Processing* 84:172-184.

Du, H., and J. D. Miller. 2007b. Adsorption states of amphipatic solutes at the surface of naturally hydrophobic minerals: A molecular dynamics simulation study. *Langmuir* 23:11587-11596.

Du, H., and J. D. Miller. 2007c. Interfacial water structure and surface charge of selected alkali chloride salt crystals in saturated solutions: A molecular dynamics modeling study. *Journal of Physical Chemistry C* 111:10013-10022.

Du, Q., E. Freysz, and Y. R. Shen. 1994. Surface vibrational spectroscopic studies of hydrogen bonding and hydrophobicity. *Science* 264:826-828.

Durand, C., and E. Rosenberg. 1998. Fluid distribution in kaolinite- or illite-bearing cores: cryo-SEM observations versus bulk measurements. *Journal of Petroleum Science and Engineering* 19:65-72.

Edwards, C. R., W. B. Kipkie, and G. E. Agar. 1980. The effect of slime coatings of the serpentine minerals, chrysotile and lizardite, on pentlandite flotation. *International Journal of Mineral Processing* 7:33-42.

Eriksson, J. C., S. Ljunggren, and P. M. Claesson. 1989. A phenomenological theory of long-range hydrophobic attraction forces based on a square-gradient variational approach. *Journal of the Chemical Society, Faraday Transactions 2: Molecular and Chemical Physics* 85: 163-176.

Wypych, F., and K.G. Satyanarayana. 2004. *Clay surfaces: Fundamentals and applications*: Academic Press.

Fa, K., A. V. Nguyen, and J. D. Miller. 2006. Interaction of calcium dioleate collector colloids with calcite and fluorite surfaces as revealed by AFM force measurements and molecular dynamics simulation. *International Journal of Mineral Processing* 81:166-177.

Fine Tailings Fundamentals. 1995. *Advances in oil sands tailings research*. Alberta, Canada: Alberta Dept. of Energy, Oil Sands and Research Division.

Fornasiero, D., and J. Ralston. 2005. Cu(II) and Ni(II) activation in the flotation of quartz, lizardite and chlorite. *International Journal of Mineral Processing* 76:75-81.

Frost, R. L., E. Horváth, É. Makó, and J. Kristóf. 2004. Modification of low- and high-defect kaolinite surfaces: implications for kaolinite mineral processing. *Journal of Colloid and Interface Science* 270:337-346.

Fuerstenau, D. W., and P. Huang. 2003. " Interfacial phenomena involved in talc flotation," in *Proc. 23rd Int. Minerals Processing Congress*, Document Transformation Technologies, pp. 1034-1043. Cape Town.

Fuerstenau, D. W., and Pradip. 2005. Zeta potentials in the flotation of oxide and silicate minerals. *Advances in Colloid and Interface Science* 114–115:9-26.

Gupta, V., and J. D. Miller. 2010. Surface force measurements at the basal planes of ordered kaolinite particles. *Journal of Colloid and Interface Science* 344:362-371.

H. Murray, H., and J. E. Kogel. 2005. Engineered clay products for the paper industry. *Applied Clay Science* 29:199-206.

Hampton, M. A., and A. V. Nguyen. 2009. Systematically altering the hydrophobic nanobubble bridging capillary force from attractive to repulsive. *Journal of Colloid and Interface Science* 333:800-806.

Hanly, G., D. Fornasiero, J. Ralston, and R. Sedev. 2011. Electrostatics and Metal Oxide Wettability. *The Journal of Physical Chemistry C* 115:14914-14921.

Hartley, P. G., I. Larson, and P. J. Scales. 1997. Electrokinetic and Direct Force Measurements between Silica and Mica Surfaces in Dilute Electrolyte Solutions. *Langmuir* 13:2207-2214.

Harvey, C. C., and H. H. Murray. 1997. Industrial clays in the 21st century: A perspective of exploration, technology and utilization. *Applied Clay Science* 11:285-310.

Haydn H, M. 1991. Overview — clay mineral applications. *Applied Clay Science* 5:379-395.

Haydn H, M. 2000. Traditional and new applications for kaolin, smectite, and palygorskite: a general overview. *Applied Clay Science* 17:207-221.

Hu, Y., and X. Liu. 2003. Chemical composition and surface property of kaolins. *Minerals Engineering* 16:1279-1284.

Hu, Y., X. Liu, and Z. Xu. 2003. Role of crystal structure in flotation separation of diaspore from kaolinite, pyrophyllite and illite. *Minerals Engineering* 16:219-227.

Hu, Y., S. Wei, J. Hao, J. D. Miller, and K. Fa. 2005. The anomalous behavior of kaolinite flotation with dodecyl amine collector as explained from crystal structure considerations. *International Journal of Mineral Processing* 76:163-172.

Hu, Y.-h., W. Sun, X.-w. Liu, and D.-z. Wang. 2003. Cleavage nature, electrokinetics, aggregation and dispersion of kaolinite. *Transactions of Nonferrous Metals Society of China* 13:1430-1434.

Hunter, R. J., and M. James. 1992. Charge reversal of kaolinite by hydrolyzable metal ions: an electroacoustic study. *Clays and Clay Minerals* 40:644-649.

Israelachvili, J. N. 1972. The Calculation of Van Der Waals Dispersion Forces between Macroscopic Bodies. *Proceedings of the Royal Society of London. A. Mathematical and Physical Sciences* 331:39-55.

Israelachvili, J. N., and R. M. Pashley. 1984. Measurement of the hydrophobic interaction between two hydrophobic surfaces in aqueous electrolyte solutions. *Journal of Colloid and Interface Science* 98:500-514.

Isrealachvili, J. N. 1985. *Intermolecular and Surface Forces*. New York: Academic Press.

Johnson, S. B., G. V. Franks, P. J. Scales, D. V. Boger, and T. W. Healy. 2000. Surface chemistry-rheology relationships in concentrated mineral suspensions. *International Journal of Mineral Processing* 58:267-304.

Kaggwa, G. B., L. Huynh, J. Ralston, and K. Bremmell. 2006. The Influence of Polymer Structure and Morphology on Talc Wettability. *Langmuir* 22:3221-3227.

Kaminsky, H. A. W., T. H. Etsell, D. G. Ivey, and O. Omotoso. 2009. Distribution of clay minerals in the process streams produced by the extraction of bitumen from athabasca oil sands. *Canadian Journal of Chemical Engineering* 87:85-93.

Kirkpatrick, R. J., A. G. Kalinichev, and J. Wang. 2005. Molecular dynamics modelling of hydrated mineral interlayers and surfaces: Structure and dynamics. *Mineralogical Magazine* 69:289-308.

Koneshan, S., J. C. Rasaiah, R. M. Lynden-Bell, and S. H. Lee. 1998. Solvent structure, dynamics, and ion mobility in aqueous solutions at 25C. *Journal of Physical Chemistry B* 102:4193-4204.

Lin, F. H., C. H. Jian, and Y. H. Lee. 2000. "A study of purified montmorillonite intercalated with 5-fluorouracil as drug carrier." Second Smith and Nephew International Symposium - Tissue Engineering, Advances in Tissue Engineering, Biomaterials and Cell Signalling pp70.

Liu, J., Z. Xu, and J. Masliyah. 2004. Role of fine clays in bitumen extraction from oil sands. *AIChE Journal* 50:1917-1927.

Long, J., H. Li, Z. Xu, and J. H. Masliyah. 2006. Role of colloidal interactions in oil sand tailings treatment. *AIChE Journal* 52:371-383.

Ma, K., and A. C. Pierre. 1999. Clay sediment-structure formation in aqueous kaolinite suspensions. *Clays and Clay Minerals* 47:522-526.

Melchionna, S., G. Ciccotti, and B. L. Holian. 1993. Hoover NPT dynamics for systems varying in shape and size. *Molecular Physics* 78:533-44.

Mezger, M., H. Reichert, S. Schöder, J. Okasinski, H. Schröder, H. Dosch, D. Palms, J. Ralston, and V. Honkimäki. 2006. High-resolution in situ x-ray study of the hydrophobic gap at the water–octadecyl-trichlorosilane interface. *Proceedings of the National Academy of Sciences* 103:18401-18404.

Miller, J., V. Gupta, H. Du, X. Wang, X. Yin, and J. Wang. 2011. "The surface chemistry of layered silicates," in *Proceedings of the Yoon Symposium, SME Annual Meeting*. Denver.

Miller, J. D., J. Nalaskowski, B. Abdul, and H. Du. 2007. Surface characteristics of kaolinite and other selected two-layer silicate minerals. *Canadian Journal of Chemical Engineering* 85:617-624.

Miranda, P. B., and Y. R. Shen. 1999. Liquid interfaces: a study by sum-frequency vibrational spectroscopy. *Journal of Physical Chemistry B* 103:3292-307.

Motta, M. M., and C. F. Miranda. 1989. Molybdate Adsorption on Kaolinite, Montmorillonite, and Illite: Constant Capacitance Modeling. *Soil Sci. Soc. Am. J.* 53:380-385.

Mular, A. L., and R. B. Roberts. 1966. "A simplified method to determine the isoelectric point of oxides," *Transactions of the Canadian Institute of Mining and Metallurgy* 69:438-439.

Nagashima, K., and F. D. Blum. 1999. Proton Adsorption onto Alumina: Extension of Multisite Complexation (MUSIC) Theory. *Journal of Colloid and Interface Science* 217:28-36.

Nalaskowski, J., B. Abdul, H. Du, and J. D. Miller. 2007. "Anisotropic character of talc surfaces as revealed by streaming potential measurements, atomic force microscopy, molecular dynamics simulations and contact angle measurements." *Canadian Metallurgical Quarterly* 46:227-236.

Nalaskowski, J., J. Drelich, J. Hupka, and J. D. Miller. 2003. Adhesion between hydrocarbon particles and silica surfaces with different degrees of hydration as determined by the AFM colloidal probe technique. *Langmuir* 19:5311-5317.

Nalaskowski, J., J. Drelich, and J. D. Miller. 2008. Forces between polyethylene surfaces in oxyethylene dodecyl ether solutions as influenced by the number of oxyethylene groups. *Langmuir* 24:1476-1483.

Nguyen, A., and H. Schulze. 2004. *Colloidal Science of Flotation*. New York: Marcel Dekker.

Nicol, S. K., and R. J. Hunter. 1970. Rheological and electrokinetic properties of kaolinite suspensions. *Australian Journal of Chemistry* 23:2177-86.

Pietrobon, M. C., S. R. Grano, S. Sobieraj, and J. Ralston. 1997. Recovery mechanisms for pentlandite and MgO-bearing gangue minerals in nickel ores from Western Australia. *Minerals Engineering* 10:775-786.

Pokrovsky, O. S., and J. Schott. 2004. Experimental study of brucite dissolution and precipitation in aqueous solutions: surface speciation and chemical affinity control. *Geochimica et Cosmochimica Acta* 68:31-45.

Pokrovsky, O. S., J. Schott, and F. Thomas. 1999. Processes at the magnesium-bearing carbonates/solution interface. I. a surface speciation model for magnesite. *Geochimica et Cosmochimica Acta* 63:863-880.

Rayner, J. H., and G. Brown. 1973. "The crystal structure of talc," *Clays and Clay Minerals* 21:103-114.

Rosenholtz, J., and S. Dudley. 1936. "The dielectric constant of mineral powders," *American Mineralogist* 21:115-120.

Saada, A., B. Siffert, and E. Papirer. 1995. Comparison of the hydrophilicity/hydrophobicity of illites and kaolinites. *Journal of Colloid and Interface Science* 174:185-185.

Schofield, R. K. 1938. Physical chemistry of clay. *Br. Clayworker* 47:208-10.

Schofield, R. K. 1939. The electrical charges on clay particles. *Soils Fert.* 2:1-5.

Sendner, C., D. Horinek, L. Bocquet, and R. R. Netz. 2009. Interfacial water at hydrophobic and hydrophilic surfaces: Slip, viscosity, and diffusion. *Langmuir* 25:10768-10781.

Shang, J., M. Flury, J. B. Harsh, and R. L. Zollars. 2008. Comparison of different methods to measure contact angles of soil colloids, *Journal of Colloid and Interface Science* 328:299-307.

Shang, J., M. Flury, J. B. Harsh, and R. L. Zollars. 2010. Contact angles of aluminosilicate clays as affected by relative humidity and exchangeable cations. *Colloids and Surfaces A: Physicochemical and Engineering Aspects* 353:1-9.

Shen, Y., S. Nihonyanagi, and K. Uosaki. 2001. Sum frequency generation (SFG) study of the pH-dependent water structure on a fused quartz surface modified by an octadecyltrichlorosilane (OTS) layer. *Physical Chemistry, Chemical Physics* 3:3463-3469.

Silvester, E. J., W. J. Bruckard, and J. T. Woodcock. 2011. Surface and chemical properties of chlorite in relation to its flotation and depression. *Mineral Processing and Extractive Metallurgy* 120:65-70.

Smietana, M., J. Szmidt, M. L. Korwin-Pawlowski, W. J. Bock, and J. Grabarczyk. 2007. Application of diamond-like carbon films in optical fibre sensors based on long-period gratings. *Diamond and Related Materials* 16:1374-1377.

Sondi, I., J. Bišćan, and V. Pravdić. 1996. Electrokinetics of Pure Clay Minerals Revisited. *Journal of Colloid and Interface Science* 178:514-522.

Sondi, I., O. Milat, and V. Pravdić. 1997. Electrokinetic Potentials of Clay Surfaces Modified by Polymers. *Journal of Colloid and Interface Science* 189:66-73.

Sondi, I., and V. Pravdić. 1996. Electrokinetics of Natural and Mechanically Modified Ripidolite and Beidellite Clays. *Journal of Colloid and Interface Science* 181:463-469.

Sposito, G., N. T. Skipper, R. Sutton, S.-h. Park, A. K. Soper, and J. A. Greathouse. 1999. Surface geochemistry of the clay minerals. *Proceedings of the National Academy of Sciences* 96:3358-3364.

Subramanian, V. 1998. Effects of long-chain surfactants, short-chain alcohols and hydrolyzable cations on the Hydrophobic and Hydration Forces. Ph.D. Dissertation, Virginia Polytechnic Institute and State University, Blacksburg, VA

Swartzen-Allen, S. L., and E. Matijevic. 1974. Surface and colloid chemistry of clays. *Chem. Rev.* 74:385-400.

Tanaka, N., D. M. Rye, Y. Xiao, and A. C. Lasaga. 1994. Use of stable sulfur isotope systematics for evaluating oxidation reaction pathways and scavenging of sulfur dioxide in the atmosphere. *Geophys. Res. Lett.* 21:1519-1522.

Tsao, Y. H., D. F. Evans, and H. Wennerstrom. 1993. Long-range attractive force between hydrophobic surfaces observed by atomic force microscopy. *Science* 262:547-550.

Tyrrell, J. W. G., and P. Attard. 2001. Images of Nanobubbles on Hydrophobic Surfaces and Their Interactions. *Physical Review Letters* 87:176104.

van Olphen, H. 1963. *An Introduction to Clay Colloid Chemistry*. New York, London: John Wiley & Sons.

van Oss, C. J. 1994. *Interfacial Forces in Aqueous Media*. New York: Marcel Dekker.

Vincent, M.-M., and D. Jean Marc. 2007. "Immersion of Solids," in *Encyclopedia of Surface and Colloid Science, Second Edition*, pp. 2892-2905: Taylor & Francis.

Vrdoljak, G. A., G. S. Henderson, J. J. Fawcett, F. J. Wicks, and J. Frederick. 1994. "Structural relaxation of the chlorite surface imaged by the atomic microscope," *Journal of American Mineralogist* 79:107-112.

Wai, K. W., and G. S. Banker. 1966. "Applications of the montmorillonites in tablet making," *Journal of Pharmaceutical Sciences* 55:1245-1248.

Wallqvist, V., P. M. Claesson, A. Swerin, J. Schoelkopf, and P. A. C. Gane. 2006. Interaction forces between talc and hydrophobic particles probed by AFM. *Colloids and Surfaces A: Physicochemical and Engineering Aspects* 277:183-190.

Wang, H. N., and J. Chen. 2004. *Geochemistry*. Beijing: Science Press.

Wang, J., A. G. Kalinichev, and R. J. Kirkpatrick. 2009. Asymmetric hydrogen bonding and orientational ordering of water at hydrophobic and hydrophilic surfaces: a comparison of water/vapor, water/talc, and water/mica interfaces. *Journal of Physical Chemistry C* 113:11077-11085.

Wang, J., A. G. Kalinichev, R. J. Kirkpatrick, and R. T. Cygan. 2005. Structure, energetics, and dynamics of water adsorbed on the muscovite (001) surface: a molecular dynamics simulation. *Journal of Physical Chemistry B* 109:15893-905.

Wang, X., J. Liu, H. Du, and J. D. Miller. 2010. States of adsorbed dodecyl amine and water at a silica surface as revealed by vibrational spectroscopy. *Langmuir* 26:3407-3414.

Wang, X., X. Yin, and J. D. Miller. 2012. "Molecular Features of Water Films Created with Bubbles at Hydrophobic and Hydrophilic Surfaces." New Delhi, India: Proceeding of International Mineral Processing Congress.

White, G. N., and L. W. Zelazny. 1988. Analysis and implications of the edge structure of dioctahedral phyllosilicates. *Clays and Clay Minerals* 36:141-146.

Williams, D. J. A., and K. P. Williams. 1978. Electrophoresis and zeta potential of kaolinite. *Journal of Colloid and Interface Science* 65:79-87.

Wolgemuth, J. L., R. K. Workman, and S. Manne. 2000. Surfactant Aggregates at a Flat, Isotropic Hydrophobic Surface. *Langmuir* 16:3077-3081.

Wood, J., and R. Sharma. 1995. How Long Is the Long-Range Hydrophobic Attraction? *Langmuir* 11:4797-4802.

Wu, W. 2001. Baseline studies of the clay minerals society source clays: Colloid and surface phenomena. *Clays and Clay Minerals* 49:446-452.

Yan, L., A. H. Englert, J. H. Masliyah, and Z. Xu. 2011. Determination of Anisotropic Surface Characteristics of Different Phyllosilicates by Direct Force Measurements. *Langmuir* 27:12996-13007.

Yin, X., and J. Drelich. 2008. Surface charge microscopy: Novel technique for mapping charge-mosaic surfaces in electrolyte solutions. *Langmuir* 24:8013-8020.

Yoon, R.-H., and S. A. Ravishankar. 1996. Long-Range Hydrophobic Forces between Mica Surfaces in Dodecylammonium Chloride Solutions in the Presence of Dodecanol. *Journal of Colloid and Interface Science* 179:391-402.

Yu, C. J., A. G. Richter, A. Datta, M. K. Durbin, and P. Dutta. 1999. Observation of Molecular Layering in Thin Liquid Films Using X-Ray Reflectivity. *Physical Review Letters* 82:2326-2329.

Zhang, J., R.-H. Yoon, and J. C. Eriksson. 2007. AFM surface force measurements conducted with silica in CnTACl solutions: Effect of chain length on hydrophobic force. *Colloids and Surfaces A: Physicochemical and Engineering Aspects* 300:335-345.

Zhang, J., R.-H. Yoon, M. Mao, and W. A. Ducker. 2005. Effects of degassing and ionic strength on AFM force measurements in octadecyltrimethylammonium chloride solutions. *Langmuir* 21:5831-5841.

Zhao, H., S. Bhattacharjee, R. Chow, D. Wallace, J. H. Masliyah, and Z. Xu. 2008. Probing surface charge potentials of clay basal planes and edges by direct force measurements. *Langmuir* 24:12899-12910.

Zheng, G., L. Liu, J. Liu, Y. Wang, and Y. Cao. 2009. "Study of chlorite and its influencing factors ", *Procedia Earth* and *Planetary Science* 1:830-837.

Šolc, R., M. H. Gerzabek, H. Lischka, and D. Tunega. 2011. "Wettability of kaolinite (001) surfaces — Molecular dynamic study". *Geoderma* 169:47-54.